UNIVERSIDAD DE CONCEPCIÓN

FACULTAD DE INGENIERÍA

Departamento de Ingeniería Eléctrica

SUPERFICIAL FES TECHNIQUES FOR IMPROVING HAND DEXTERITY IN NEUROREHABILITATION

Tesis presentada a la Facultad de Ingeniería de la Universidad de Concepción para optar al grado académico de Magíster en Ciencias de la Ingeniería con Mención en Ingeniería Eléctrica.

POR: JAVIER IGNACIO SÁEZ ACUÑA.

Profesor Guía: PABLO ESTEBAN AQUEVEQUE NAVARRO.

Profesores Co-Guía: BRIAN JAMES ANDREWS.

FRANCISCO ANDRÉS SAAVEDRA RODRÍGUEZ.

diciembre 2025

Concepción, Chile.

Table of Contents

LIST OF FIGURES ..... **V**

LIST OF TABLES ..... **XIII**

RESUMEN **XV**

ABSTRACT **XVII**

ABBREVIATIONS ..... **XIX**

CHAPTER 1. INTRODUCTION **1**

1.1. PROBLEM/MOTIVATION 5

A. Implanted Neuroprostheses 6

B. Transcutaneous Electrical Stimulation Based on Electrode Arrays 8

C. Proposed Approach 9

CHAPTER 2. LITERATURE REVIEW **13**

2.1. INTRODUCTION 13

2.2. CURRENT TRANSCUTANEOUS ELECTRICAL STIMULATION SYSTEMS 16

2.3. CONCENTRIC ELECTRODES 21

2.4. ELECTRODE PROTOTYPING PROCESSES 27

2.5. INTERFERENTIAL CURRENTS 31

2.6. DISCUSSION 36

CHAPTER 3. OBJECTIVES **40**

3.1. HYPOTHESIS 40

3.2. GENERAL OBJECTIVE 40

3.3. SPECIFIC OBJECTIVES 40

3.4. SCOPE AND LIMITATIONS 41

3.5. PUBLICATIONS 41

CHAPTER 4. METHODOLOGY **43**

4.1. ELECTRODE MODELING 44

4.1.1 Finite Element Method *45*

A. Electrode Comparison Side-by-side and Concentric 49

B. Effects of Concentric Electrodes Design Parameters 52

4.1.2 Nerve Axon Model *54*

4.2. PROTOTYPING PROCESS 57
4.2.1 Substrate Printing 57
4.2.2 Electrode Assembly 58
4.2.3 Impedance Measurement 59
4.3. IN-VIVO TESTING 61
4.3.1 Set-up y and Testing Procedure 61
A. Movement Analysis with Concentric Electrodes 63
B. Subjective Pain Measurement 69

CHAPTER 5. RESULTS AND DISCUSSION 70

5.1. MATHEMATICAL MODELING 70
5.1.1 Electrode Comparison Side-by-side and Concentric 70
5.1.2 Effect of Design Parameters of Concentric Electrodes 77
5.1.3 Discussion 82
5.2. PROTOTYPING PROCESS 85
5.2.1 Fabrication 85
5.2.2 Impedance Measurement 89
5.2.3 Discussion 91
5.3. IN-VIVO TESTING 92
5.3.1 Biphasic Stimulation with Concentric Electrodes 92
5.3.2 Interferential Current Stimulation with Concentric Electrodes 97
5.3.3 Discussion 102

CHAPTER 6. CONCLUSION 106

CHAPTER 7. APPENDIX 108

7.1. BIPHASIC STIMULATION WITH CONCENTRIC ELECTRODES 108
7.2. INTERFERENTIAL CURRENT STIMULATION WITH CONCENTRIC ELECTRODES 110

CHAPTER 8. REFERENCES 113

List of Figures

Fig. 1.1. Broad view of the nervous system of the forearm and hand. Extracted from E. Losanno et al, 2023 [15]. 3

Fig. 1.2. Anatomy of the Forearm in Cross-Section and Pathways of the Forearm Nerves. Extracted from D. B. Popović 2014[14]. 4

Fig. 1.3. Electrode Positioning for Wrist Extension Using the Traditional Approach. Extracted from: [16]. 6

Fig. 1.4. General Schematic of an implanted neuroprosthetic with automated control. Extracted from Gupta et al, 2023 [17]. 7

Fig. 1.5. Electrode Array System for Forearm Stimulation. Extracted from Hoffmann et al, 2012 [25]. 9

Fig. 1.6. Summary Diagram of the State of the Art in Upper Limb Motor Rehabilitation Technologies Post-Stroke and the Positioning of the Proposed Approach [6], [17]. 11

Fig. 2.1. Electrode array-based systems for restoration of hand function developed by different research groups. A) HandNMES Crema et al., 2018 [40], b) Popović-Maneski et al., 2013 [32] and c) Fesia Grasp, developed by the company Fesia Technology (Martín-Odriozola et al., 2022) [35]. 18

Fig. 2.2. Electrode Configurations Used in the Study by Datta et al., 2008. Extracted from Datta et al, 2008 [51]. 23

Fig. 2.3. Electrodes and results obtained from the study conducted by Bortoletto et al, 2016 [19], a) concentric electrode used, b) location during in vivo tests, c) magnitude of the electric field in the normal direction, and d)

magnitude of the electric field on the cortical surface. Extracted from Bortoletto et al, 2016. 25

Fig. 2.4. Electrodes fabricated using 3D printing techniques: a) 3D filament electrodes with graphene [65], b) Ag electrodes with conductive polymers [66]. Extracted from Stephens-Fripp et al, 2018 and Chlaihawi et al. 2018. 30

Fig. 2.5. The schematic diagram illustrates the impact of interferential currents on cerebral function. The diagram depicts two alternating currents of slightly differing frequencies. It is assumed that neurons are unresponsive to high frequencies; however, in the regions where these currents interfere, demodulation of the currents is induced, resulting in neuronal responsiveness. Extracted from Mirzakhalili et al., 2020 [67]. 32

Fig. 2.6. Electric potential and demodulation produced in a peripheral nerve produced by the interferential currents. A) Color map of the potential generated by the superposition of the individual electrodes and the direction of the electric field. A myelinated axon is placed in the center. B) Voltages generated by each electrode sum at point c. C) The resultant electric potential and the envelope produced at point d. Extracted from Mirzakhalili et al., 2020 [67]. 33

Fig. 4.1. Schematic of the Methodology for Thesis Development.... 44

Fig. 4.2. 3D Simplified Forearm Model Created in COMSOL Multiphysics 6.1, a) Superior view with concentric electrode and b) square, c) Anatomical reference extracted from 3D4Medical [84] c) Transverse view with labeled model layer. 47

Fig. 4.3. To-Scale Electrodes Used in the Comparative FEM Study, a) Square electrodes, b) Concentric electrodes. 50

Fig. 4.4. To-Scale designs of concentric electrodes for different sizes and B) inter-electrode distances. 53

Fig. 4.5. Schematic of the MRG Model for Myelinated Motor Axons in Mammals [88]. 55

Fig. 4.6. Layered Visualization of the 3D-Printed Electrode: The first layer consists of the flexible resin substrate, the second layer is the active material made of Ag/AgCl conductive paint, and the final layer is the gel. 59

Fig. 4.7. Impedance measurement setup and electrode comparison. A) Schematic representation of the electrode–skin interface model used for impedance measurements. B) Equivalent electrical circuit model representing the interface C) Measurement protocol parameters and D) Photograph of the electrodes evaluated applied to the anterior forearm. 60

Fig. 4.8. Histogram of age, circumference of the proximal third part of the forearm and forearm large of the participants. The mean value and SD are indicated in the figure. 63

Fig. 4.9. In-vivo procedure. A) Resting position of patients during measurement. B) Motor points for flexion digits 4-5 (blue) and thumb abduction (green), concentric electrode where place in the motos points (MP), square electrodes were placed in MP and SQ as indicated in the figure. C) Zones where the stimulation was applied using biphasic stimulation with concentric electrodes (green) and ICS with concentric electrodes (green and blue). 65

Fig. 4.10. (A) Experimental setup for in-vivo testing, including the stimulator, stimulation channels, emergency killswitch, VAS pain scale, and Perception Neuron Studio gloves for motion capture. The reference axis was used for calibration, and data acquisition was performed using a laptop running Axis Studio software. ScienceMode2 software was employed to communicate stimulation parameters to RehaMove2 stimulator. (B) Visualization of the biomechanical hand model within Axis Studio, used for real-time motion during electrical stimulation trials. system. 67

Fig. 4.11. Visual Analog Scale (VAS) for subjective pain perception [95]. 69

Fig. 5.1. Qualitative visualization of the electric field distribution generated by concentric and square electrodes using finite element modeling. (A) Electric field magnitude in a longitudinal plane parallel to the nerves, represented as a 3D surface plot. (B) Cross-sectional view of the electric field in a transverse plane at the center of the model. (C) Contour and vector field maps showing field direction and intensity. 72

Fig. 5.2. A) Quantitative analysis of activation spread for concentric and square electrodes. The x-axis shows the total depolarization (∑AF), while the y-axis represents the **AFspread**. Lower values on the y-axis indicate more localized neural activation, while higher values on the x-axis total depolarization. B) 3D visualization of normalized activating function distribution along the nerve axis for both configurations. The concentric electrode produces a more confined and targeted activation profile, while the square electrode exhibits broader, less selective stimulation. 74

Fig. 5.3. Focality index as a function of radial distance r for the concentric and square electrodes. The concentric electrode demonstrates significantly higher focality, with a smaller half-maximum radius $\mathbf{r0.5}$ = 16.3 mm, compared to the square electrode $\mathbf{r0.5}$ = 24.4 mm. A lower $\mathbf{r0.5}$ indicates a more spatially confined electric field, emphasizing the enhanced precision of the concentric configuration. 74

Fig. 5.4. In-silico evaluation of nerve activation with concentric and square electrodes using the MRG axon model. (A) Activation thresholds for ulnar, median, and radial nerves. (B) Action potential propagation along the median nerve with 7 mA (activation) and 2 mA (No activation). (C–D) Recruitment profiles showing selective activation ranges (HSR, MSR, LSR). Concentric electrodes achieved narrower selective recruitment, whereas square electrodes produced broader, less specific activation 76

Fig. 5.5. Current density magnitude along a longitudinal line beneath the electrode surface. A) Comparison across electrode sizes (Size 1–3) and B) Comparison across inter-electrode distances (I-E1 to I-E3). The non-uniformity of each configuration is quantified using the peak-to-average ratio k, with lower values indicating more homogeneous current distribution.....78

Fig. 5.6. Membrane potential distributions over time and along the Ranvier nodes representing axon activation in the ulnar, median, and radial nerves, corresponding to various concentric ring electrode designs with an input of 5 mA. 80

Fig. 5.7. Electric field (V/m) distribution in a cross-sectional plane parallel to the nerve pathways for three concentric electrode designs (I-ED 1, I-ED 2, and I-ED 3), each with varying inter-electrode distances. A constant

input current of 5 mA was applied in all cases. The results show that increasing the inter-electrode distance enhances the depth of electric field penetration, as evidenced by the spread of higher voltage regions in I-ED 3 compared to I-ED 1. 81

Fig. 5.8. Electric field (V/m) distribution for electrode Size 1 at varying stimulation frequencies: 1 Hz-100 Hz (typical range for FES), and 1k Hz-10k Hz (typical range for ICS). All simulations were performed with a constant input current of 5 mA. The results demonstrate a decrease in electric field magnitude as frequency increases, due to the reduced impedance of biological tissues at higher frequencies. 82

Fig. 5.9. A) Stages of the fabrication process of the electrodes. Flexible resin substrate, substrate filled with conductive Ag/AgCl paint and hydrogel layer. B) Frontal view of the 3D-printed electrode with a measurement reference. 86

Fig. 5.10. Impedance vs. frequency for concentric, square prototyped, and commercial electrodes. All configurations show decreasing impedance with frequency, with greater differences observed below 1 kHz. 91

Fig. 5.11. Representative example of metacarpophalangeal (MCP) joint trajectories during digit flexion with square and concentric electrodes. (A) Square electrode stimulation induced simultaneous flexion of all four fingers, with similar amplitudes across them. (B) Concentric electrode stimulation produced a more selective response, with pronounced flexion of the ring finger, partial activation of the pinky, and minimal movement in the index and middle fingers. (C) Biomechanical hand model illustrating the

corresponding flexion response, showing the transition from resting position to flexion after stimulation onset. 93

Fig. 5.12. Average range of motion (ROM) during (A) finger flexion and (B) thumb abduction with square and concentric electrodes. Square electrodes induced broader activation across digits, while concentric electrodes showed greater selectivity, reducing unintended movements in non-targeted fingers. 95

Fig. 5.13. Visual Analog Scale (VAS) scores for perceived discomfort during (left) finger flexion and (right) thumb abduction with square and concentric electrodes. For flexion, concentric electrodes showed slightly higher average VAS scores than square electrodes, though both remained within the mild-to-moderate range. For thumb abduction, mean VAS scores were similar between electrode types, with most participants reporting mild discomfort, no statistical significance was found. 97

Fig. 5.14. ICS and concentric electrode results across forearm zones. (A) Threshold currents required to elicit activation and the number of participants responding in each zone for both stimulation methods. (B) Example of finger movements generated with ICS across zones Z1–Z4; no activation was observed in Z4 for this participant. (C) Average range of motion (ROM) for each finger across zones and stimulation methods, showing generally higher ROM with ICS compared to concentric biphasic stimulation. 99

Fig. 5.15. VAS scores comparing discomfort during concentric biphasic stimulation and ICS. Average VAS scores were significantly lower

with ICS (2.12 ± 1.73) compared to concentric biphasic stimulation (3.75 ± 1.98), indicating improved comfort with ICS (paired t-test, $p < 0.05$).....101

List of Tables

Table 4.1. Dimensions of the Components in the FEM Model. 46

Table 4.2. Isotropic Dielectric Properties of the Domains in the FEM Model at 80 Hz Extracted from IT'IS Foundation [83]. 46

Table 4.3. Dimensions of the Electrodes in the Comparative Study. 50

Table 4.4. Dimensions of Different Designs of Concentric Ring Electrodes 53

Table 4.5. Summary of the tests to be performed, measuring instrument and the objective of the measurement. 61

Table 4.6. Age and Anthropometric Data of the participants 62

Table 5.1. Estimated material costs for 3D-printed electrodes. 87

Table 5.2. Average ± SD ROM (°) of fingers with square and concentric electrode for finger flexion and thumb abduction. 95

Table 5.3. Mean ± SD values of Selectivity index and VAS per geometry 96

Table 5.4. Stimulation current threshold (mean ± SD, mA) for each zone and number of participants that elicit an activation for each type of stimulation. 100

Table 7.1. Subjects ROM (°) per finger and selectivity index during stimulation with square biphasic stimulation for finger flexion. 108

Table 7.2. Subjects ROM (°) per finger and selectivity index during stimulation with concentric biphasic stimulation for finger flexion. 108

Table 7.3. Subjects ROM (°) per finger and selectivity index during stimulation with square biphasic stimulation for thumb abduction. 109

Table 7.4. Subjects ROM (°) per finger and selectivity index during stimulation with concentric biphasic stimulation for thumb abduction..... 109

Table 7.5. Subjects ROM (°) per finger during biphasic stimulation with concentric electrodes in Z1. 110

Table 7.6. Subjects ROM (°) per finger during biphasic stimulation with concentric electrodes in Z2. 110

Table 7.7. Subjects ROM (°) per finger during biphasic stimulation with concentric electrodes in Z3. 110

Table 7.8. Subjects ROM (°) per finger during biphasic stimulation with concentric electrodes in Z4. 111

Table 7.9. Subjects ROM (°) per finger during ICS with concentric electrodes in Z1. 111

Table 7.10. Subjects ROM (°) per finger during ICS with concentric electrodes in Z2. 111

Table 7.11. Subjects ROM (°) per finger during ICS with concentric electrodes in Z3. 112

Table 7.12. Subjects ROM (°) per finger during ICS with concentric electrodes in Z4. 112

Resumen

La presente tesis aborda los desafíos asociados con los déficits motores del miembro superior posteriores al accidente cerebrovascular. Centrando la investigación en la FES como modalidad terapéutica, se busca mejorar la precisión, eficacia y accesibilidad de la estimulación eléctrica superficial para la rehabilitación de la destreza manual. Las técnicas actuales presentan limitaciones relevantes, como baja selectividad muscular y malestar durante la terapia.

La literatura destaca tres conceptos para optimizar neuroprótesis no invasivas: (1) rediseño geométrico de electrodos hacia configuraciones concéntricas para focalizar el campo eléctrico; (2) uso de manufactura aditiva para crear nuevas geometrías; y (3) aplicación de estímulos de media frecuencia para reducir la impedancia cutánea y mejorar la comodidad. No obstante, persisten vacíos respecto al impacto de estos enfoques en terapias FES, lo que constituye el foco de esta tesis.

La metodología comprende cuatro fases: diseño de electrodos, modelación computacional, prototipado mediante manufactura aditiva y pruebas in vivo en sujetos sanos. Los resultados indican que los electrodos concéntricos generan un campo eléctrico más localizado ($r_{0.5}$: 16,3 mm vs. 24,4 mm), y que el proceso de impresión 3D permitió fabricar electrodos flexibles y biocompatibles a bajo costo (~2,4 USD). En pruebas in vivo, la selectividad aumentó un 32% y la estimulación interferencial redujo significativamente el malestar (VAS: 3,75 ± 1,98 a 2,12 ± 1,73).

En conjunto, la tesis demuestra que optimizar la geometría de los electrodos y los parámetros de estimulación mejora la selectividad y la

comodidad en FES superficial, aportando bases para futuras terapias no invasivas orientadas a tareas y personalizadas para cada paciente.

Abstract

The proposed thesis aims to address the pressing challenges associated with post-stroke upper limb motor deficits. By focusing on FES as a therapeutic modality, this research seeks to refine the precision, efficacy, and accessibility of surface electrical stimulation techniques, advancing hand dexterity rehabilitation. Current approaches for upper limb neurorehabilitation face significant limitations, including low selectivity in muscle activation and considerable discomfort during therapy.

To enhance the applicability of non-invasive motor neuroprostheses, three key concepts have emerged in the literature: (1) modifying electrode geometry to concentric designs, which can focalize the electric field and improve selectivity; (2) utilizing additive manufacturing techniques to create novel electrode shapes; and (3) employing medium-frequency stimuli to reduce skin impedance, enhance comfort and enable a precise control over the stimulation area. Despite their potential, there are notable gaps in the literature regarding the application of these concepts to FES therapies and their resulting effects. Addressing these gaps forms the central objective of this thesis.

The methodology encompasses four core phases: (1) electrode design (2) computational modeling, (3) prototyping through additive manufacturing techniques and (4) in-vivo testing conducted on healthy subjects.

The results demonstrated that concentric electrodes produced a more localized and selective electric field, as confirmed by qualitative FEM visualizations and quantitative metrics showing a focality radius ($r_{0.5}$) of 16.3 mm compared to 24.4 mm for square electrodes. The proposed 3D-printing-

based prototyping process enabled the rapid fabrication of flexible, biocompatible electrodes with an average unit cost of approximately 2.4 USD, facilitating efficient iteration between design and experimentation. In-vivo evaluations showed a 32% increase in selectivity index (0.723 ± 0.175 vs. 0.546 ± 0.098, $p < 0.01$) for concentric electrodes and a significant reduction in discomfort with interferential current stimulation, decreasing VAS scores from 3.75 ± 1.98 to 2.12 ± 1.73 ($p < 0.05$).

This thesis contributes to the domain of neurorehabilitation by demonstrating that optimizing electrode geometry and stimulation waveform parameters can significantly enhance both selectivity and comfort in surface FES. These advances help bridge the gap between complex neuroprosthetic systems and accessible, clinically applicable stimulation technologies. The validated hypothesis establishes a solid foundation for the future integration of these methods into task-oriented, patient-specific neurorehabilitation therapies.

Abbreviations

ADL : Activities of Daily Living

FEM : Finite Element Method

FES : Functional Electrical Stimulation

ICS : Interferential Current Stimulation

LMICs : Low- and middle-income countries

NMES : Neuromuscular Electrical Stimulation

PCB : Printed Circuit Board

QoL : Quality of Life

SCI : Spinal Cord Injury

VAS : Visual Analog Scale

WHO : World Health Organization

Chapter 1. Introduction

Globally, stroke ranks among the leading causes of death and disability. According to the World Stroke Organization, nearly 12 million strokes occur annually worldwide, with approximately 94 million people currently living who have experienced a stroke [1]. Furthermore, it is estimated that nearly one-third of stroke survivors endure lasting disabilities [1]. The Chilean context is no exception, with approximately 26,280 cases annually, making strokes the leading cause of disability in adults in the country [2].

A stroke occurs when a blood vessel in the brain ruptures or becomes blocked, causing damage that leads to various sequelae depending on the affected area [3], [4]. Among the motor consequences of stroke, hemiplegia—characterized by the complete loss of mobility on one side of the body—and hemiparesis, which refers to partial loss of movement, are the most prevalent. Notably, hemiparesis affects over 70% of stroke survivors, particularly in the upper limb [5]. This condition causes difficulties in walking, grasping objects, dressing, and other activities of daily living (ADLs) compromising the patient’s independence [6]. Furthermore, it not only limits patients' autonomy in their everyday lives but also impacts their professional and social environments. Depending on the severity of the stroke, individuals may be unable to return to their previous jobs, leading to socioeconomic challenges for their families. Combined, these difficulties lead to significant mental health challenges such as depression and anxiety,

hinder reintegration into the workforce and contribute to socio-economic burdens [7], [8].

The development of rehabilitation technologies has paved the way for patients to achieve greater independence and improve their quality of life (QoL). Some rehabilitation therapies include robot-assisted therapy, virtual reality therapy, and functional electrical stimulation (FES) [6]. FES is a rehabilitation technique that uses electrical pulses to enhance motor function and promote neuroplasticity by engaging patients in everyday activities such as grasping objects, writing, or finger movements [9]. This therapy focuses on improving motor function while promoting neuroplasticity, and its effectiveness in enhancing neural connections has been well-documented [10]. On the other side, neuromuscular electrical stimulation (NMES) is another rehabilitation therapy that applies electrical currents to muscles to produce tetanic contractions, strengthening the muscles and mimicking exercise therapy [11]. These transcutaneous electrical stimulation therapies are often used together, as their goals complement one another, offering a complete approach to improving motor function and muscle strength [12].

Rehabilitation therapies based on electrical stimulation are widely used in neurorehabilitation [13]. However, current therapies face challenges in delivering systems with high efficiency and applicability. One major challenge is the application of FES therapies in the upper limb, where precise control of the generated movement must be achieved precisely and without compromising comfort during stimulation. The forearm's complex anatomy adds difficulty to achieve the selectivity needed to generate specific movements [14].

The muscles responsible for hand movements are divided into two main groups: extrinsic hand muscles and intrinsic hand muscles. Broadly, the extrinsic muscles are located in the forearm and are responsible for larger hand movements, such as flexion and extension. In contrast, the intrinsic muscles are located within the hand itself and are responsible for finer and more precise movements of the hand and fingers [15]. In Fig. 1.1 is shown a broad view of the nervous system pathway that control hand movements.

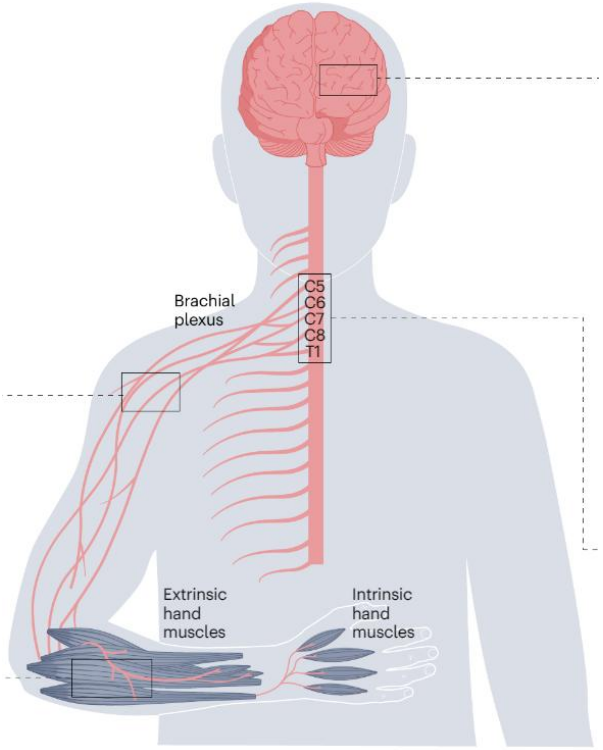

Fig. 1.1. Broad view of the nervous system of the forearm and hand. Extracted from E. Losanno et al, 2023 [15].

The peripheral nervous system that controls hand movements is composed of three main nerves: the median nerve, the ulnar nerve, and the radial nerve. The median nerve primarily controls the extrinsic flexors and pronators, while the radial nerve governs the opposing functions—extensors

and supinators. The ulnar nerve primarily innervates the intrinsic hand muscles, facilitating fine motor control [15].

In this context, stimulation systems must provide sufficient selectivity to ensure that only the targeted nerve is activated. Unintended activation of adjacent nerves or muscles can lead to undesired or ineffective movements, undermining the therapy's effectiveness. Addressing this challenge is essential for improving the precision and comfort of FES-based treatments in the forearm [14]. Below is an anatomical and physiological diagram of the forearm. (Fig. 1.2).

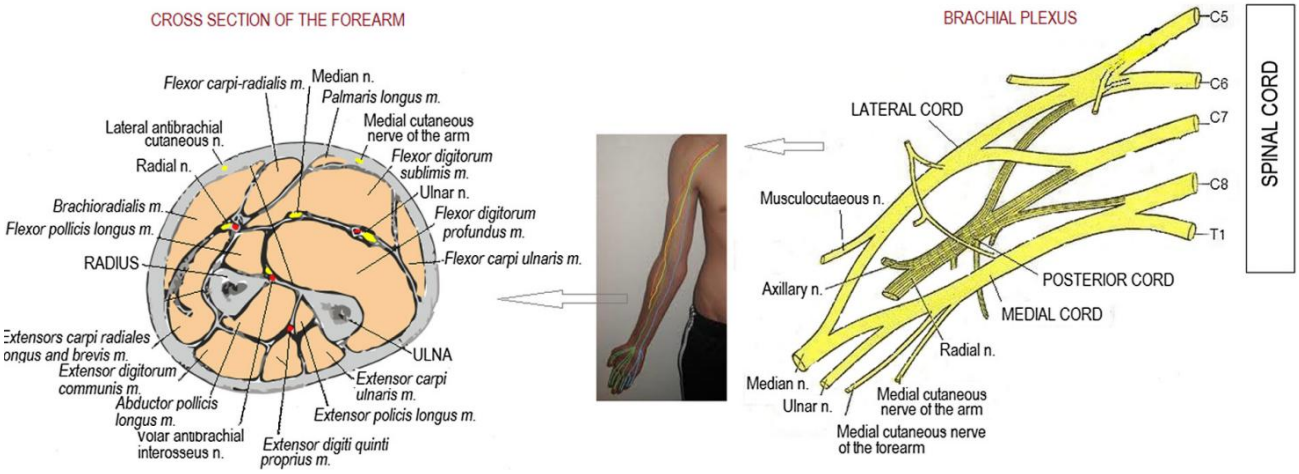

Fig. 1.2. Anatomy of the Forearm in Cross-Section and Pathways of the Forearm Nerves. Extracted from D. B. Popović 2014[14].

An example of this anatomical complexity is the path of the ulnar nerve. It enters the anterior compartment of the forearm by passing between the two heads of the flexor carpi ulnaris muscle, running parallel to the ulna bone. Along its course, the ulnar nerve is positioned deep to the flexor carpi ulnaris and divides into three main branches: the muscular branches of the

ulnar nerve, the palmar branch, and the dorsal branch. This nerve plays a critical role in the motor innervation of several muscles, including [14]:

- The flexor carpi ulnaris.
- The hypothenar muscles.
- The opponens digiti minimi.
- The flexor digitorum superficiales and profundus.
- The adductor pollicis.

Similarly, the radial and median nerves have a distribution and path comparable to the ulnar nerve. Given this anatomy, even if only a single nerve is stimulated, multiple muscles may be activated simultaneously. For this reason, the rehabilitation technique employed must be capable of directing the stimulus to individual motor units with precision [14].

1.1. Problem/Motivation

Currently, there are three approaches to overcome this challenge. The traditional method involves using strategically placed stimulation points to generate the desired movement, typically employing square or circular electrodes (Fig. 1.3) [16]. This approach is widely used in clinical neurorehabilitation. However, such systems have functional limitations, with the main challenges being: 1) low selectivity in the nerves stimulated due to the broad area covered by the stimulation, 2) discomfort during stimulation caused by the activation of pain receptors, and 3) the need for constant repositioning of the electrodes to achieve different types of movements. In the literature, there are two approaches to resolving these challenges. The

first involves implantable neuroprostheses, and the second utilizes surface electrode arrays, both of which are described below.

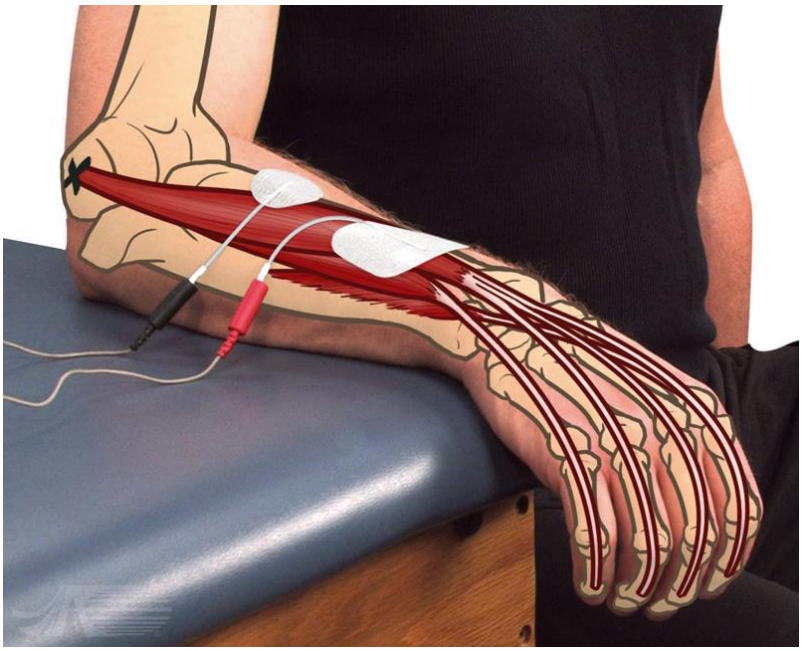

Fig. 1.3. Electrode Positioning for Wrist Extension Using the Traditional Approach. Extracted from: [16].

A. Implanted Neuroprostheses

Implantable electronic devices are widely used to restore or support the function of organs, such as cardiac pacemakers. Additionally, these devices are extensively utilized in implanted neuroprostheses. This technique employs electrodes implanted in peripheral nerves, the spinal cord, or the brain to control the motor and sensory nervous responses of the patient, aiming to restore lost functions. Beyond the stimulation system (electrodes and stimulator), neuroprostheses are often integrated with brain activity sensors to establish direct coordination with muscles and provide sensory

feedback. (Fig. 1.4) [17]. This type of treatment presents certain challenges that are closely related to the implantation process.

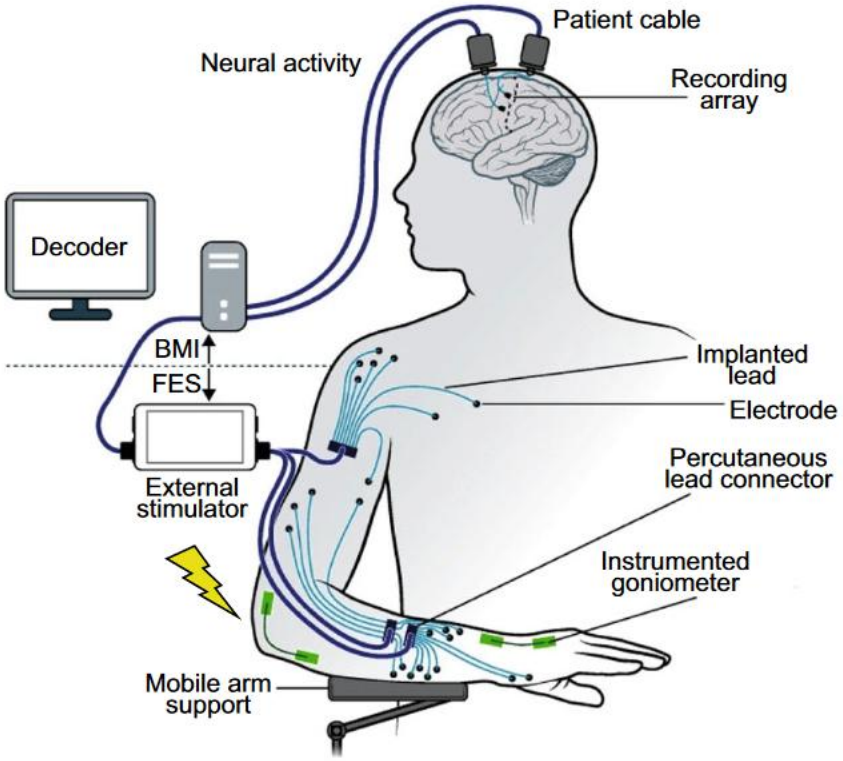

Fig. 1.4. General Schematic of an implanted neuroprosthetic with automated control. Extracted from Gupta et al, 2023 [17].

Being an invasive procedure, this treatment carries inherent risks such as pain during the procedure, infection, allergic reactions [18], or nerve damage [19]. Additionally, there is the possibility of implant displacement. Moreover, the materials used to construct the implant must be biocompatible to ensure proper integration with biological tissue, prevent bacterial growth over time, and feature a structural design appropriate for the area where it is placed [20], [21]. Any failure in these characteristics would necessitate another invasive intervention for the patient. These inherent traits of

implantable devices limit their applicability, given the current medical trend toward achieving minimally invasive systems.

B. Transcutaneous Electrical Stimulation Based on Electrode Arrays

Over the past decade, research has focused on using small electrodes arranged in arrays to achieve high selectivity in the stimulated muscle [22]. This type of stimulation is typically achieved using an array of circular electrodes (~0.8 cm^2) along with a rectangular electrode placed at a certain distance from the array [23]. Although this approach is still under development, researchers have reported achieving a wide variety of distinct movements [24], [25]. However, this solution relies on complex systems to achieve its objectives, requiring multi-channel stimulators (~16 channels) and specifically designed electrodes that are not widely available. The current challenge for this type of technology lies in developing appropriate algorithms and control systems to accurately manage the position of the hand and fingers [24], [26].

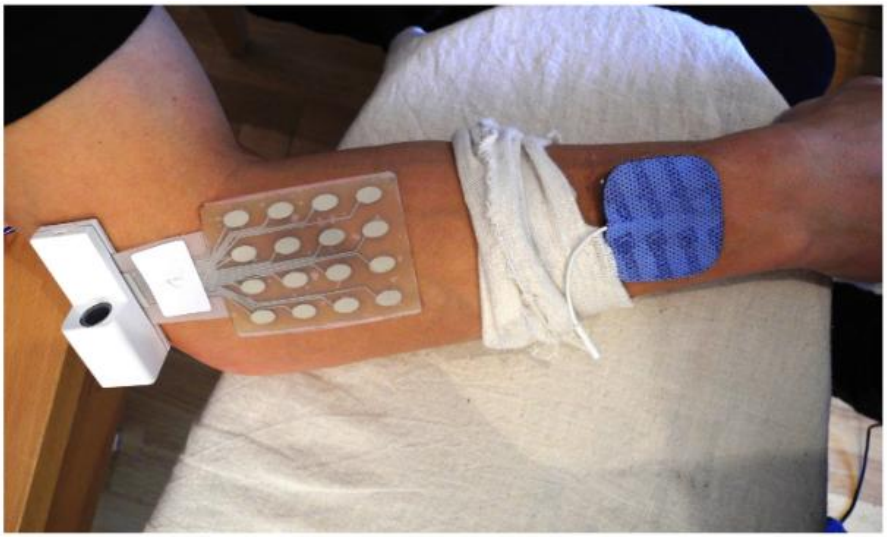

Fig. 1.5. Electrode Array System for Forearm Stimulation. Extracted from Hoffmann et al, 2012 [25].

Considering the details of both systems, their implementation in the context of our country presents significant challenges. One of the primary obstacles is the reliance on foreign suppliers for acquiring advanced electrodes and stimulators, which complicates accessibility and increases dependency on external resources.

C. Proposed Approach

Due to the application limitations outlined earlier, the approach developed in this thesis focuses on modifying fundamental parameters of electrical stimulation, such as the electric field generated by electrode geometry and the stimulation current, to enhance the traditional approach and the applicability of these therapies.

To achieve this, technologies such as 3D printing will be utilized to create new electrode geometries—such as the concentric ring electrode—through a simple prototyping process. Interferential currents will also be

employed to improve both comfort and the activation area during stimulation. This approach aims to assess the precise control of forearm movements, identifying potential advantages and highlighting limitations for clinicians performing these therapies and for patients receiving them. Fig. 1.6 presents a summary diagram of the current state-of-the-art and the positioning of the proposed approach.

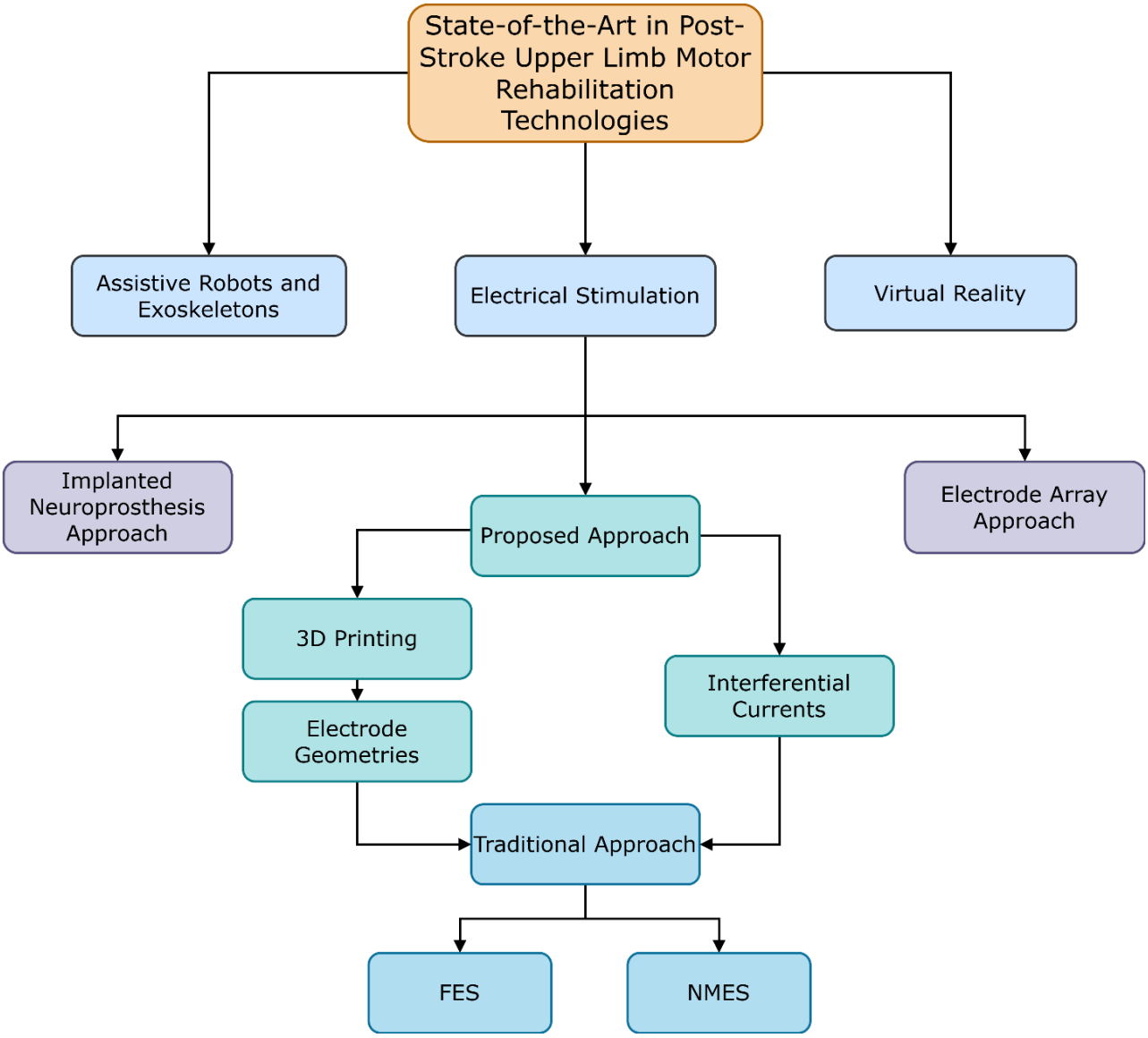

Fig. 1.6. Summary Diagram of the State of the Art in Upper Limb Motor Rehabilitation Technologies Post-Stroke and the Positioning of the Proposed Approach [6], [17].

Enhancing the traditional approach by the proposed approach could significantly improve the applicability of these therapies. Greater control over the generated movement could increase the range of achievable motions and optimize task-oriented treatments. Additionally, it would enable the

possibility of a more personalized treatment approach, tailoring therapies to meet the specific needs of individual patients. [27].

Chapter 2. Literature Review

2.1. Introduction

FES has proven to be an effective tool for motor rehabilitation, actively enhancing neuroplasticity and increasing cortical connections within the central nervous system and also could enhance axon regeneration in the peripheral nervous system [10], [28]. However, for an improvement of the nervous system using electrical stimulation in patients, immediate action after the stroke is needed, which in some cases is not possible. Also, there is a possibility that patients may not respond or demonstrate improvements to these therapies. If the patients is in one of these cases, electrical stimulation has also demonstrated muscular benefits, such as increased strength, prevention of atrophy and improved blood circulation [13], [29], [30]. So, the access of patients to these therapies is crucial.

As it was previously mentioned, the anatomical complexity of the forearm and hand poses challenges for achieving specific stimulation in surface electrical stimulation therapies. This complexity makes it difficult to generate precise and functional movements. The widely used approach in clinical non-invasive neurorehabilitation involves placing electrodes in strategic positions to produce the desired movement or exercise. There are online repositories and books that detail the characteristics and positions needed to achieve these movements [16]. However, this approach requires different electrode placements for each movement, necessitating manual repositioning. This limitation reduces the applicability and usability of

training sessions that involve multiple movements limiting the functional movements that can be reach [19].

In recent years, a discussion has emerged in the literature regarding the primary limitations of the traditional approach using surface electrodes. According to Koutsou et al. 2016 and Usman et al. 2020 [19], [31], one of the main issues with surface FES is its low selectivity due to the large size of the electrodes used, which can lead to the activation of undesired muscles and inability to effectively stimulate small and thin muscles. Since the source of the electric field is far from the target nerve, electrode positioning and proper modulation of the electric field are crucial for effectively activating the desired muscle [31], [32]. Additionally, the method is restricted to activating only superficial muscles, further limiting its effectiveness in targeting deeper muscular structures [33], due to the high impedance of the skin at the low frequencies typically employed in electrical stimulation [34]. Martín-Odriozola et al. (2022) further highlight the critical importance of muscular selectivity in upper-limb rehabilitation, particularly as hand dexterity relies on precise and diverse muscle activation [35]. This underscores that enhancing muscle selectivity is essential to directing stimulation for specific movements [35].

Besides, discomfort produced by the electrical pulses is a significant challenge in FES therapies, as it can lead to patients withdrawing from treatment [36]. This discomfort often arises from the simultaneous activation of sensory and motor fibers, and even the preferential activation of sensory fibers compared to motor fibers during transcutaneous electrical stimulation, creating unpleasant sensations that discourage continued use [37]. Repetition

is the cornerstone of effective FES therapies, as consistent practice is essential for meaningful rehabilitation progress [38]. Addressing this issue requires targeted strategies that not only enhance patient comfort but also ensure adherence, thereby maintaining the therapeutic efficacy and long-term benefits of FES treatments.

Despite these limitations, this approach is the most widely used worldwide for its ease of use, resource requirements and applicability [15]. Consequently, improving this aspects could facilitate more effective task-oriented rehabilitation approaches, targeting precise functional goals for patients, while also enabling advancements like the development and application of non-invasive neuroprostheses [39].

The classical approach to addressing this issue involves the use of implantable motor neuroprostheses. In this method, the patient undergoes a surgical procedure to implant an electrical system (electrodes and wires) directly into peripheral nerves. This type of neuroprosthesis is described by Gupta et al. 2023 [17]. Typically, the electrical stimulator is externally connected, allowing the patient to manage the stimulation directed to electrodes located on peripheral nerves or motor units. Furthermore, these treatments are often combined with brain-machine interface systems to detect the patient's intention to move, enhancing the overall functionality and responsiveness of the neuroprostheses but also increasing the complexity of the system. Although these systems provide highly specific and efficient solutions, there are certain limitations to their use. First, due to the invasive nature of the implantation process, patients are exposed to risks inherent to surgery, including pain, infection during the procedure, and the possibility of

electrode displacement. In the event of a major complication, the patient would need to undergo another invasive intervention [18]. Other challenges are discussed by Losanno et al. 2023 [15]. There are barriers in the current state-of-the-art that limit the clinical application of these systems. Most studies involving these technologies have been conducted in laboratory settings using large-scale systems, which are impractical for daily use [15]. For these systems to be adopted in routine clinical environments, their size must be significantly reduced. Additionally, the production, operation, and maintenance costs pose significant obstacles to their implementation [15]. Therefore, less invasive and more widely applicable alternatives to this approach are necessary to overcome these limitations.

In response to this challenge, researchers have proposed solutions to improve the selectivity of electrical stimulation systems using surface electrodes. These advancements aim to enable their application in anatomically complex areas, such as the forearm and hand. By achieving greater selectivity, surface FES systems could represent a significant step forward in movement control for surface rehabilitation therapies [40].

2.2. Current Transcutaneous Electrical Stimulation Systems

Electrode array systems emerged as a solution to address the limitations of traditional approaches, particularly in terms of selectivity, comfort, and stimulation zones [23]. These systems were developed to overcome the drawbacks of traditional methods, which relied on non-specific, conventional electrodes that often resulted in the simultaneous activation of undesired muscles. Typically, these systems consist of multiple

electrode arrays strategically placed on the skin, control interfaces for modulating stimulation parameters, and, in some cases, advanced algorithms to automatically adjust electrode configurations [19]. The electrodes used in these systems are commonly made of flexible PCBs on polycarbonate substrates or conductive textile materials [41]. Additionally, these systems often utilize multi-channel stimulators, enabling simultaneous control of multiple electrodes, thereby enhancing precision and functionality.

In 2018, Crema et al. proposed the HandNMES system, a portable, multi-site device based on neuromuscular electrical stimulation (NMES) designed to restore gripping function in individuals with neurological injuries [40]. The HandNMES system stood out for its focus on improving usability and comfort by utilizing flexible conductive materials, which allowed for better adaptation to the patient's anatomy [40]. In 2019, Shin and Hu presented a multi-channel stimulation system that used an electrode mesh aligned with the ulnar and median nerves to diversify the activation of finger flexors. This system enabled a greater variety of finger movement patterns, providing a significant advantage for precise control during rehabilitation [42]. In 2020, Usman et al. developed an FES system that combined a high-density electrode array with a self-calibration algorithm. This system significantly improved stimulation selectivity and reduced the co-activation of undesired muscles, enhancing the effectiveness of rehabilitation [19]. In 2022, Martín-Odriozola et al. introduced Fesia Grasp, a system that utilizes multiple stimulation fields to improve selectivity and personalize rehabilitation, advancing the adaptability and precision of therapy for individual patients [35]. Some of these technologies are shown on Fig. 2.1.

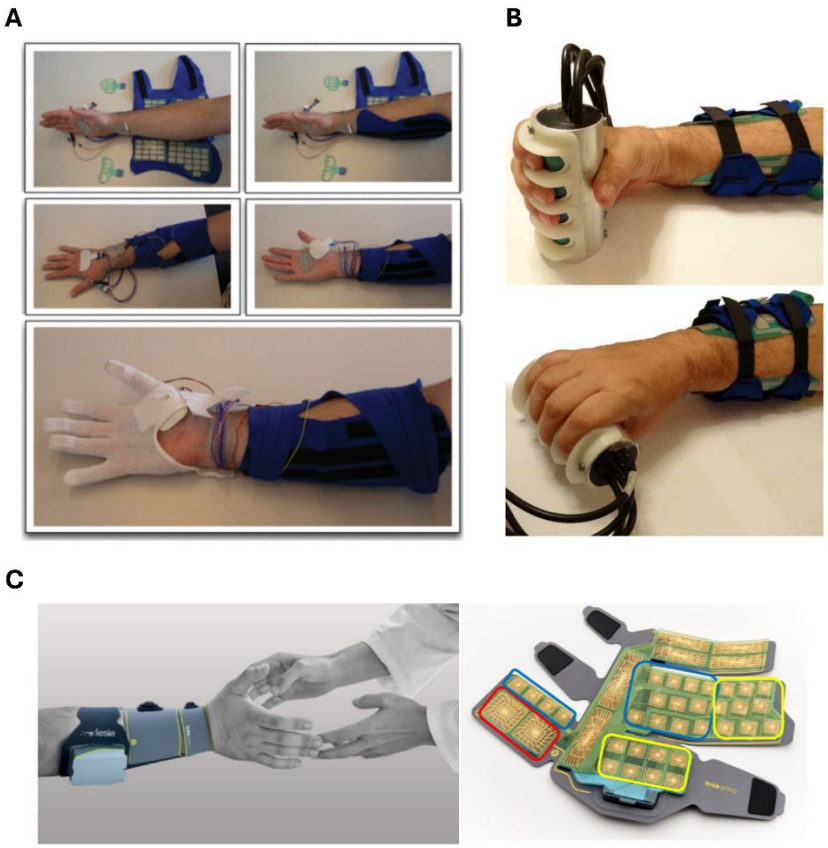

Fig. 2.1. Electrode array-based systems for restoration of hand function developed by different research groups. A) HandNMES Crema et al., 2018 [40], b) Popović-Maneski et al., 2013 [32] and c) Fesia Grasp, developed by the company Fesia Technology (Martín-Odriozola et al., 2022) [35].

Electrode arrays offer significant advantages in terms of precision and stimulation selectivity. Systems such as HandNMES, Shin and Hu's multi-channel device, and Fesia Grasp have shown promising results by enabling the selective activation of specific muscle groups, thereby improving the ability to generate functional movements. However, surface systems face challenges in reaching deeper tissues due to the high impedance of the skin at low frequencies. This limitation confines stimulation to more superficial

levels and necessitates the application of higher voltages to attempt to overcome this constraint, which can impact comfort and effectiveness [34].

On the other hand, these systems also face limitations in terms of applicability in different contexts worldwide, particularly in low- and middle-income countries (LMICs) where limited access to rehabilitation services and socioeconomic disparities exacerbate the challenges faced by stroke survivors by receiving lower-quality care [43], [44].

Key barriers include high manufacturing and acquisition costs, the requirement for complex interfaces and advanced algorithms for control, and the limited availability of electrodes, which are not widely accessible in the market. Flexible electrode manufacturing processes rely on advanced printing technologies, adding further challenges to achieving low-cost and effective production methods. The high-tech nature of these electrodes makes their replicability limited for both researchers and clinicians, as they often depend on external companies (e.g. ScreenTec or Tecnalia). This reliance increases costs and extends the waiting times between design and testing phases. Furthermore, while Fesia Grasp is commercially available, its high cost poses a significant barrier to widespread clinical adoption. Taken together, these factors significantly limit the accessibility of neurorehabilitation systems, hindering their broader implementation in clinical settings.

This issue is extensively discussed in the current landscape by Losanno et al. (2023), who emphasize the critical need to reduce costs to facilitate the clinical adoption of these technologies [15]. The authors highlight that neurotechnological systems used for grip restoration will require substantial

reductions in production, operation, and maintenance costs. Moreover, numerous barriers exist for deploying these neurotechnologies in low-resource settings and even for widespread use in developed countries. These challenges are often due to variations in healthcare systems influenced by financial constraints or limitations in human resources, further hindering their accessibility and implementation [15], [45]. Addressing these limitations is crucial to ensuring that such innovations can be equitably integrated into diverse healthcare systems worldwide.

Recently, Barelli et al. (2022), motivated by these challenges, designed STIMGRASP, a FES device aimed at home-based rehabilitation [46]. This system is characterized by its portability and ease of use, making it more accessible for patients needing to conduct rehabilitation at home. STIMGRASP was developed with a focus on simplicity, leveraging external elements such as orthoses, positioning it as an alternative to traditional approaches. Unlike electrode array systems, STIMGRASP reduces system complexity while maintaining efficiency by relying on external components like orthoses [46]. However, the system does not address the issue of selectivity inherent in traditional approaches, suggesting that it lacks the capacity to provide precise adjustments for the rehabilitation of more anatomically complex areas. Another noteworthy system is MyndMove, an 8-channel FES neurostimulator developed to enhance upper limb motor rehabilitation. MyndMove offers advanced stimulation control, enabling functional movements in patients with neurological injuries [47]. However, its primary limitation lies in its high cost, which restricts its availability and widespread clinical adoption. Despite this, MyndMove is designed for use in

traditional therapies, offering greater precision due to its advanced electronic design, making it a valuable option for improving the effectiveness of rehabilitation treatments [47].

The accessibility and practicality of these technologies are recurring issues in the literature [15]. High costs and technical complexity are key factors that limit the adoption of these innovations, leaving patients without affordable options to benefit from advances in FES. Systems that achieve high selectivity tend to be complex, while simpler and more portable solutions often compromise stimulation specificity, which affects precise movement control. Systems like STIMGRASP have shown that the traditional approach can be complemented to enhance both performance and applicability in clinical settings. The ongoing discussion focuses on how to enrich the traditional approach to address its key limitations. Concepts such as the use of concentric electrodes, the fabrication of electrodes through 3D printing, and the application of interferential currents are emerging in the literature as potential strategies to enhance and complement the traditional approach, aiming for a balance between simplicity, precision, and accessibility.

2.3. Concentric Electrodes

Modifying the geometry of traditional electrodes is an alternative that has been studied by various authors for different applications. These modifications are primarily driven by the specific design objectives that need to be achieved.

In upper-limb surface neuroprostheses, electrode geometry plays a crucial role in achieving efficient and precise activation. The importance of design lies in obtaining controlled and comfortable responses during surface stimulation [48]. Various electrode geometries have been proposed in the literature to achieve specific objectives during electrical stimulation. One such design is the concentric ring electrode, initially proposed by Besio in 2006 [49]. This electrode geometry was originally intended to provide more focused measurements of surface electromyography. Later, concentric electrode geometry was studied for different types of electrical stimulation. Due to its smaller stimulation area, current density considerations during stimulation are critical for this type of electrode. Besio's 2006 research analyzed the efficient use of concentric electrodes for electrical stimulation, suggesting considerations such as the use of appropriate conductive materials and maintaining stable skin contact [50]. Ensuring a stable skin-electrode interface allowed the concentric electrode to be explored in applications such as transcranial electrical stimulation, aiming to avoid implantation. These applications require highly focused electric fields to target specific neurons, as studied by Datta et al. in 2008 [51]. Their study evaluated the electric field generated by various geometries based on concentric electrodes using FEM simulations. The geometries examined are shown in Fig. 2.2.

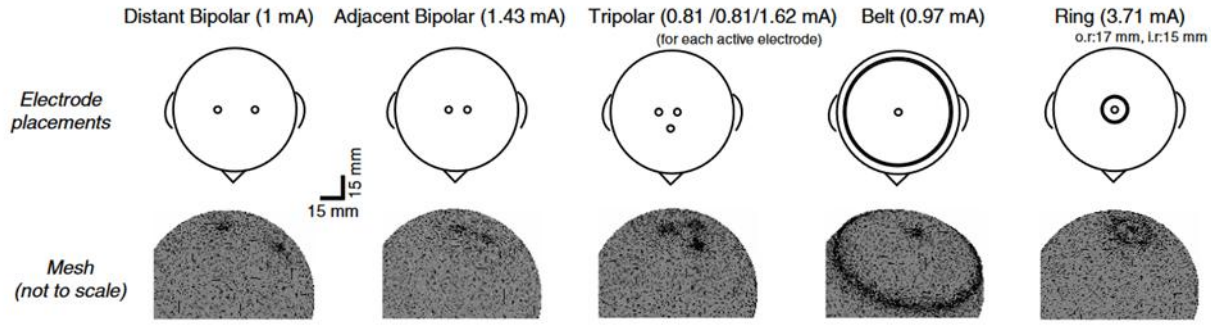

Fig. 2.2. Electrode Configurations Used in the Study by Datta et al., 2008. Extracted from Datta et al, 2008 [51].

The results obtained by these authors demonstrate a clear focus achieved by the concentric electrode. However, this configuration showed reduced stimulation depth compared to other geometries. It is important to note that the input current in this study was direct current, suggesting that in an FES context, the results might differ. This is because the intensity of the generated field depends on tissue impedance, which is influenced by the stimulation frequency and the current path through various tissue layers before reaching the target. This pathway is significantly different in the skull compared to the upper or lower extremities. Despite these differences, the study concluded that electrode configurations can be modified to achieve varying degrees of spatial focus, providing flexibility in applications depending on the target area and the desired outcomes.

Subsequently, this electrode geometry was evaluated in vivo by Besio et al. in 2011 [52], in the context of transcranial electrical stimulation in rats. The objective of this study was to analyze the electrical potential generated in the hippocampus of rats during transcranial stimulation using concentric electrodes. The study demonstrated that the potential generated beneath the

central disc of the electrode could reach magnitudes sufficient to activate neurons [18]. These results showed an in-vivo behavior similar to the previously mentioned in silico findings, further validating the efficacy of concentric electrodes for targeted stimulation.

Another study conducted in 2016 by Bortoletto et al. [53], aimed to evaluate the hypothesis of previous authors in vivo with healthy participants. For this, they recruited 15 healthy individuals who underwent direct transcranial electrical stimulation using concentric electrodes. Motor evoked potentials generated by the stimulation were recorded, and a human head model based on magnetic resonance imaging was used to calculate the electric field distribution. The results showed that in healthy participants, the stimulation produced by the electrodes was highly focused, particularly beneath the central electrode [53] (Fig. 2.3). This improved the precision of the stimulation by concentrating the current beneath the central ring, thereby reducing current dispersion and enhancing the focality of the treatment.

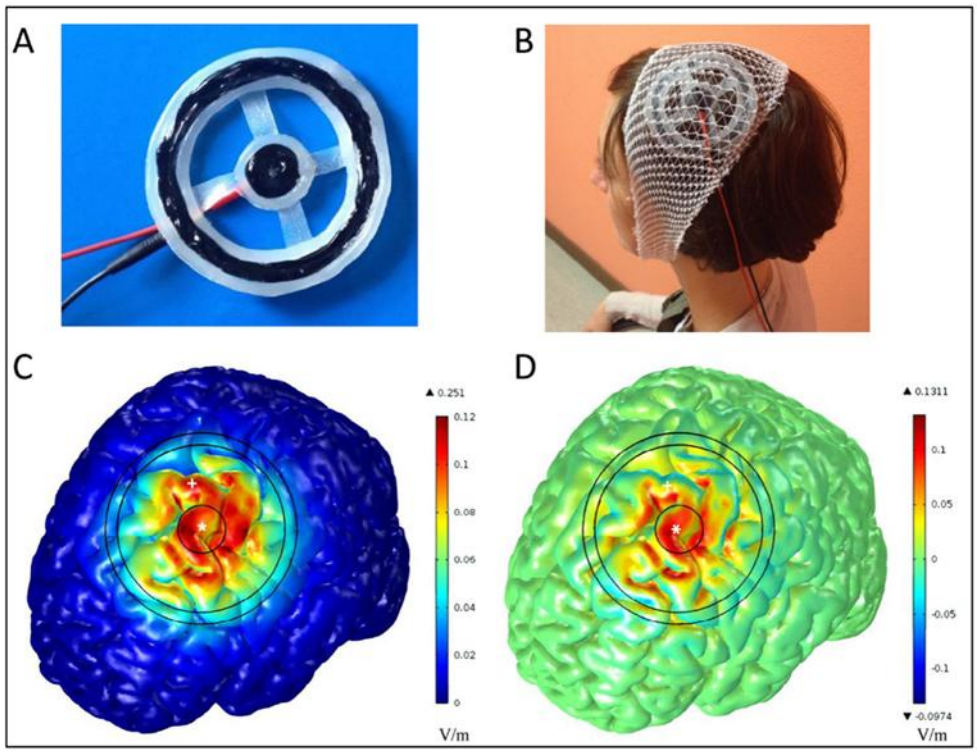

Fig. 2.3. Electrodes and results obtained from the study conducted by Bortoletto et al, 2016 [19], a) concentric electrode used, b) location during in vivo tests, c) magnitude of the electric field in the normal direction, and d) magnitude of the electric field on the cortical surface. Extracted from Bortoletto et al, 2016.

The results presented by the authors demonstrate how modifying a parameter of electrical stimulation, in this case the electrode geometry, can alter the generated stimulation to achieve the required focalization for transcranial electrical stimulation. This type of stimulation differs in certain conditions from motor transcutaneous FES, as the tissues and their distribution are distinct. In transcranial stimulation, the current must pass through bone tissue before reaching the target structure (the brain), unlike peripheral stimulation, where the nerve is surrounded by muscle. Due to these differences, the behavior of concentric electrodes must be evaluated specifically for motor surface FES applications.

In the state-of-the-art of non-invasive neuroprosthesis, researchers have evaluated the performance of concentric electrodes in surface FES for motor-related applications. Ravichandran et al. (2020) demonstrated that concentric electrodes offer advantages by providing a more uniform distribution of electrical current, which reduces the unintended activation of adjacent sensory and muscle fibers [54]. This advancement is crucial for targeting specific muscles, such as in hand neuroprostheses [54]. Similarly, Keogh et al. (2022) reported that concentric electrodes could stimulate the phrenic nerve to control the diaphragm, with the distribution helping to maximize muscle response while minimizing side effects [55]. Additionally, Cassar et al. (2023) optimized concentric electrode geometry using a mathematical approach. The researchers found that, like previous cases, the optimized geometry achieved more focused stimulation. Moreover, they observed that concentric electrodes could activate deeper nerve fibers without excessively increasing current density, offering a balance between comfort, efficiency, and safety in FES therapies [56].

The characterization and evaluation of the different parameters of stimulation on concentric electrodes must be evidenced due to the inherent difference with respect to concentric electrodes. As it was previously mentioned, concentric electrodes tend to increase the current density in the skin not only because of their smaller size, but also because of the edge-effect produced by abrupt changes in the voltage through the different tissues. This effect may be boosted with the anode and cathode proximity. Also, another key parameter is to evaluate the optimal design of the geometry of the concentric electrode to reduce unintended muscle activation and ensure that

the action potential is triggered only in the target nerves. This characterization of the concentric electrode has not been discussed in the literature yet and it's fundamental to discuss and propose further applications.

For evaluating these concentric electrode designs, they must be fabricated through prototyping process that ensure key parameters such as biocompatibility but also leverage time, cost, as ease of implementation.

2.4. Electrode Prototyping Processes

The geometries currently prototyped in the state-of-the-art employ various manufacturing methods, such as flexible PCB, copper, or 3D printing. However, the prototyping process must strike a balance between performance efficiency (in terms of conductivity), usability (biocompatibility, flexibility, breathability, and adhesion), process time, and cost [57]. Achieving this balance enhances the applicability and replicability of the process. Below, the processes utilized in the state of the art are described.

One of the most commonly used procedures involves employing PCBs or flexible PCBs. The popularity of these methods lies in their ease of implementation and customization. However, in most cases, critical factors such as biocompatibility or breathability are overlooked. RaviChandran et al. (2020) [54], used this technique to fabricate prototype electrodes. In their study, the electrodes were coated with a gel on their surface for application on humans. However, applying gel over the entire electrode can create a short circuit between the anode and cathode, causing the electrical current to flow through the gel rather than the tissues, potentially impacting the results.

Additionally, since the electrodes were not made from flexible material, they failed to adapt to the conditions of the human body and did not allow moisture transfer, which could lead to increased skin irritation. This same process was employed by Golestanirad et al, 2013 [58]. The primary issue with this procedure is the in-vivo use, as copper is highly toxic to biological tissues. When copper particles are absorbed by biological tissue, they can cause cellular toxicity [59], which is linked to conditions such as dermatitis [60] and even alopecia [61]. This highlights the critical importance of ensuring that electrodes intended for in vivo use are biocompatible to prevent adverse reactions.

A different approach was employed by Krenn et al. 2015 [41], who used a flexible printed circuit with a polyimide base, a material whose biocompatibility has been validated for use in electrode-skin interfaces. They also applied a gold conductive layer to prevent copper oxidation. However, while this method addresses biocompatibility and durability concerns, it presents challenges in terms of balancing complexity, cost, and time. This procedure is not widely applicable, as it requires specialized materials and skilled personnel, making it less accessible for all settings.

Another approach involves the use of textile electrodes, as demonstrated by Skrzetuska et al. (2021), where electrodes were fabricated using machine embroidery [62]. While this method offers flexibility and adaptability, it can pose challenges in terms of the precision of the created geometry and the uniformity of current application. These limitations can result in "hot spots," areas of increased current density that may lead to discomfort or uneven stimulation.

With the rise of 3D printing, printed electrodes have gained popularity in the current literature. This is due to the wide variety of printing techniques available and the customization possibilities depending on the intended use. 3D printing has the potential to enhance electrode performance by improving mechanical flexibility, stretchability, and conformability, while maintaining biocompatibility—key characteristics required for the fabrication of electrode prototypes [63]. However, constant challenges remain in terms of cost and implementation [64]. Below, some applications of printed electrodes or 3D-printed electrode fabrication are described.

Stephens-Fripp et al. (2018) fabricated reusable concentric electrodes using Ninjaflex® (NinjaTek, Lititz PA, USA), which was processed in an industrial spray gun chamber to embed graphene particles into the substrate. The researchers reported good flexibility and reliable measurements over time [65]. Another approach, proposed by Chlaihawi et al. (2018) [66], involved printing Ag electrodes on a PET substrate. Multi-walled carbon nanotubes and PDMS were used as a conductive polymer, which was then deposited onto the printed Ag electrode. The results demonstrated the applicability of this type of electrode for ECG measurements.

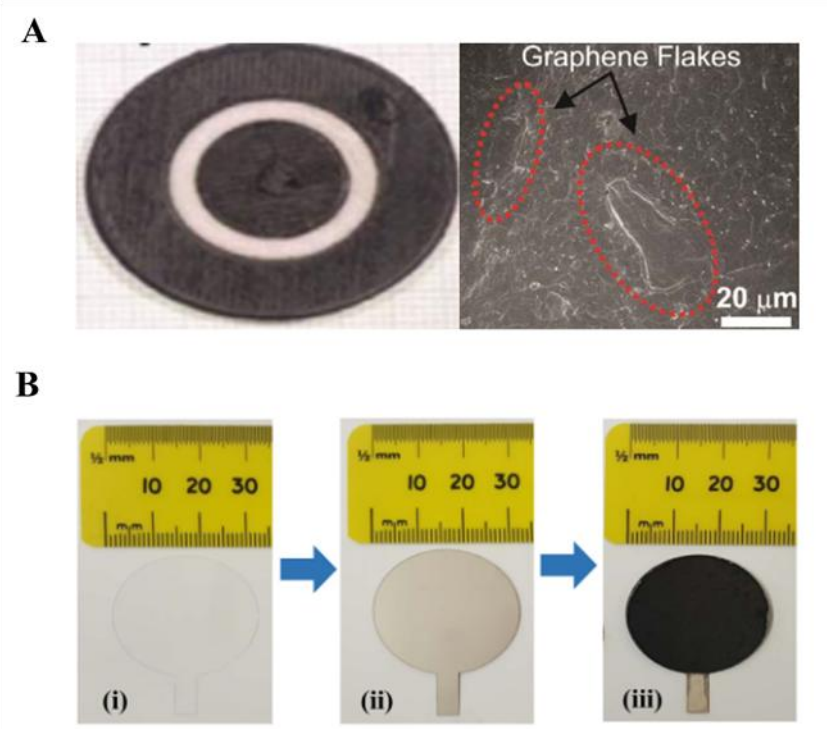

Fig. 2.4. Electrodes fabricated using 3D printing techniques: a) 3D filament electrodes with graphene [65], b) Ag electrodes with conductive polymers [66]. Extracted from Stephens-Fripp et al, 2018 and Chlaihawi et al. 2018.

The 3D printing processes mentioned above rely on advanced printing technologies and materials, which limit their replicability for prototyping purposes. Researchers aiming to evaluate the performance of new electrode geometries often require specialized equipment and personnel or must rely on external companies for fabrication, increasing both the cost and time associated with the design and evaluation process. Furthermore, the characteristics required for stimulation electrodes differ naturally from those needed for measurement or sensory stimulation electrodes. Motor stimulation electrodes must ensure comfort and avoid tissue damage, often incorporating

gel layers, and they operate at frequencies distinct from those used in sensory feedback applications.

Thus, there is a need in the literature for a fabrication process that is simple, fast, safe, and efficient to validate new electrode geometries for use in motor surface FES applications. This prototyping process can leverage advancements in 3D printing and draw inspiration from processes reported in the literature to reduce its complexity while maintaining effectiveness.

2.5. Interferential Currents

Medium-frequency stimuli are current inputs within the range of 1 kHz to 10 kHz. Due to the range of frequencies that these stimuli use, the impedance of the skin is significantly reduced, and different physiological processes occur in the patient.

Interferential currents are a type of electrical stimulation that uses two medium-frequency currents with slightly different frequencies. These waves are demodulated by the body, producing a third, lower-frequency current that penetrates deeper into the tissues. This occurs due to the reduced skin impedance at higher frequencies. This effect is described in the following figures. Fig. 2.5, represent the effect of interferential currents on the brain, the same effect is produced in the upper limb. The diagram shows two alternating input currents with slightly different frequencies. These input stimuli do not affect the neural respond. However, in the areas where these input currents interfere, demodulation is produced creating a low-frequency stimulus. This stimulus can generate neural responses [67]. Fig. 2.6 shows the electric potential and the demodulation produced by the interferential

currents in a peripheral myelinated axon. A) depicts a color map for the electric potential with the lines of electric field, a single axon is positioned in the center. B) Shows the electric potential produced by the two input currents as well as the summatory of the currents and C) shows the resultant electric potential and the amplitude modulation of the signal [67].

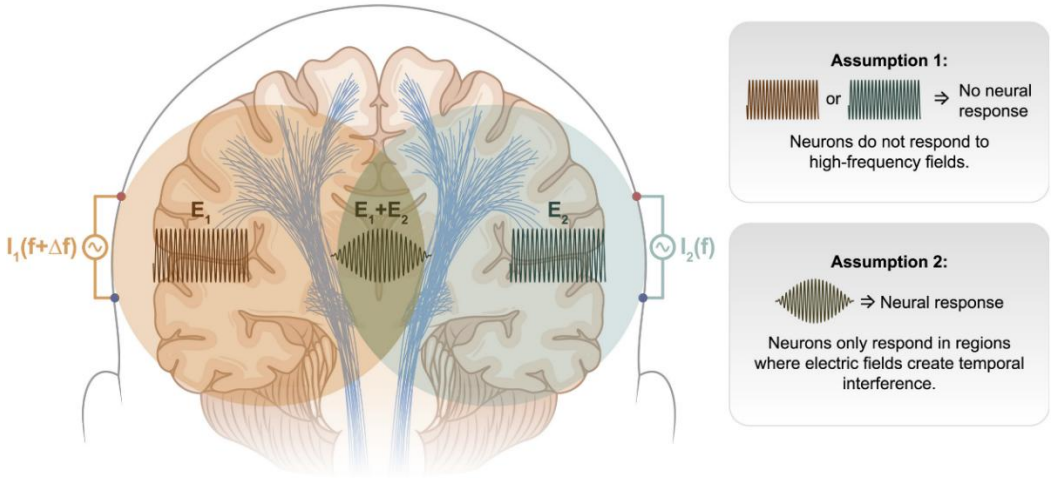

Fig. 2.5. The schematic diagram illustrates the impact of interferential currents on cerebral function. The diagram depicts two alternating currents of slightly differing frequencies. It is assumed that neurons are unresponsive to high frequencies; however, in the regions where these currents interfere, demodulation of the currents is induced, resulting in neuronal responsiveness. Extracted from Mirzakhalili et al., 2020 [67].

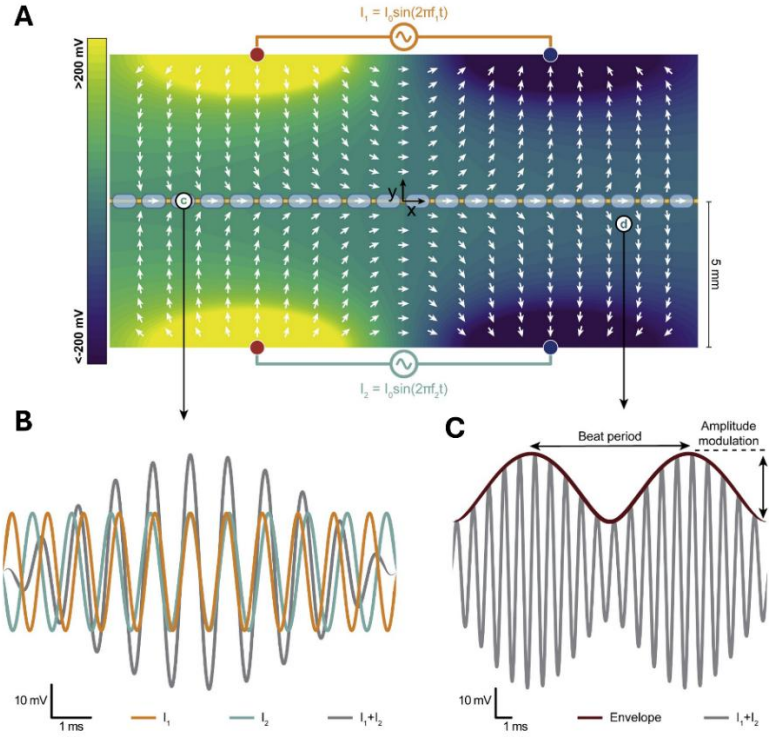

Fig. 2.6. Electric potential and demodulation produced in a peripheral nerve produced by the interferential currents. A) Color map of the potential generated by the superposition of the individual electrodes and the direction of the electric field. A myelinated axon is placed in the center. B) Voltages generated by each electrode sum at point c. C) The resultant electric potential and the envelope produced at point d. Extracted from Mirzakhalili et al., 2020 [67].

Interferential currents have been commonly used in the treatment of chronic pain due to their ability to induce analgesic effects [68]. According to Goats (1990), this analgesic effect is achieved by stimulating sensory nerve fibers and disrupting the transmission of pain signals to the central nervous system [69]. By using medium-frequency currents, interferential stimulation reduces pain perception, providing an analgesic sensation for the patient. Additionally, Goats noted that interferential currents can also induce motor stimulation by generating gentle muscle contractions. Goats mention that muscle fatigue during this type of stimulation is significantly lower compared

to other forms of low-frequency stimulation, as interferential currents interfere less with the normal physiological processes of muscles and nerves [69], but further and recent evidence is needed to assess this statement.

A motor application of interferential current stimulation (ICS) was described by Kozasa et al. (2018) [70], who observed that increasing the average frequency reduced pain perception during stimulation of deep muscles such as the soleus. Additionally, the study demonstrated that interferential currents could induce contractions at 50% of the maximum voluntary contraction. The authors highlighted that this type of stimulation could be valuable in functional rehabilitation, particularly during the push-off phase of ankle movement in gait [70]. On the other hand, Bounyong et al. 2016 explored controlling the interference area in ICS, showing that improved muscle selectivity could be achieved by adjusting the proportion of the electrode area [71].

This concept of enhanced selectivity has also been applied to transcranial stimulation, aiming to achieve greater depth and precision in targeting specific brain regions. Interferential stimulation offers several advantages over other forms of brain stimulation, such as transcranial direct current stimulation (tDCS) or transcranial alternating current stimulation (tACS). These advantages include greater penetration, allowing deeper brain structures to be reached without increasing the current intensity applied to the scalp. This reduces side effects and enables more effective stimulation. Furthermore, the higher frequencies used in ICS result in less pain or discomfort for patients compared to other techniques. Finally, the focal specificity of the resulting modulation allows stimulation to be concentrated

on specific brain areas without significantly affecting superficial regions, providing more precise control over the stimulated areas [67], [72].

In the state-of-the-art, ICS has primarily been used in applications not directly related to FES training, such as the treatment of knee osteoarthritis or shoulder impingement syndrome [73], [74]. While motor improvements have been observed in these applications, these enhancements cannot be solely attributed to direct motor effects. Instead, they result from reduced pain and increased patient comfort, which facilitate better performance during rehabilitation.

ICS is also used to prevent pelvic organ prolapse (Korkut et al., 2023) by strengthening the pelvic floor muscles and improving their endurance. This is achieved through the stimulation of the involved muscles, generating contractions that help provide adequate support for internal organs. Additionally, this type of stimulation has been shown to enhance muscle strength, which is essential for preventing the progressive weakening that can lead to prolapse [75].

A recent study evaluated the comfort of ICS in the forearm using both computational modeling and psychophysical testing. The analysis focused on activation thresholds and subjective comfort in peripheral nerves. The findings showed that activation thresholds did not differ significantly between ICS and conventional stimulation, challenging one of the central assumptions of ICS. Nevertheless, comfort increased substantially under ICS. These results support the need for comparative evaluations of comfort between ICS and biphasic stimulation [76]. The absence of lower neural activation thresholds does not reduce the value of ICS. Medium-frequency

carriers decrease tissue impedance, which lowers the voltage required to deliver a given current. This advantage is most relevant for voltage-controlled stimulators, common in commercial devices, as it allows more efficient operation within compliance limits. For current-controlled stimulators, however, the effect is minimal since the device adjusts voltage.

Medium-frequency stimuli are noteworthy to evaluate in FES therapies. Their ability to reduce skin impedance through higher frequencies, provide comfortable and effective stimulation, the wide commercial availability position of the interferential currents as a promising alternative for optimizing motor FES therapies. However, significant gaps remain in the literature regarding the effectiveness of ICS in traditional FES applications. Therefore, it is crucial to evaluate this approach within the current body of research and present detailed results that highlight the advantages, disadvantages, and limitations of its application.

2.6. Discussion

Throughout this literature review, a broad spectrum of FES techniques and approaches for motor rehabilitation of the upper limb, specifically the forearm and hand, has been explored. Both traditional systems and recent advancements aimed at improving selectivity and intervention efficacy have been highlighted. Among the more conventional approaches are FES systems utilizing traditional electrodes; however, these systems face limitations, such as low selectivity and discomfort during stimulation.

Implantable neuroprostheses represent a distinct approach within neurorehabilitation, characterized by direct interfaces with peripheral nerves

or the central nervous system. Unlike surface FES, which often struggles with low selectivity due to current dispersion through the skin and subcutaneous tissues, implantable systems inherently achieve precise and focused stimulation. However, their invasive nature introduces risks such as infection, electrode displacement, and high production and maintenance costs, which substantially limit their applicability outside specialized clinical settings, particularly in resource-constrained environments.

The literature consequently points to the need for non-invasive alternatives that remain accessible and adaptable across clinical contexts while maintaining stimulation specificity. Such approaches could help bridge the gap between the simplicity of traditional systems and the precision of invasive solutions.

In response to these limitations, alternative approaches have been proposed, including the use of electrode arrays and multi-channel systems. These systems enhance stimulation selectivity by diversifying movement patterns and optimizing muscle activation. However, they also face significant barriers, such as high manufacturing costs and reliance on complex technologies. Research by Crema et al., Shin and Hu, and Usman et al. has demonstrated that these arrays provide benefits in terms of precision and movement control [19], [40], [42], but challenges related to accessibility and high costs, as discussed by Losanno et al. (2023), persist [15].

The development of STIMGRASP has also been highlighted as an effort to simplify motor rehabilitation through a more accessible, home-oriented approach. STIMGRASP has shown that the traditional FES approach can be complemented with external elements, such as orthoses, to

reduce system complexity and facilitate application in a home setting [46]. On the other hand, MyndMove offers a technologically advanced solution that complements the traditional approach. However, its high cost presents a significant obstacle, limiting its widespread adoption despite its potential for improving precision and functionality in motor rehabilitation therapies [47].

Recent studies suggest that modifying electrode geometry—particularly through concentric designs—may improve stimulation focality and efficiency by promoting a more uniform current distribution and reducing unintended activation of surrounding tissues. Nevertheless, evidence regarding their specific performance in motor-oriented FES remains limited. Advances in rapid prototyping, such as flexible PCBs and 3-D printing, could facilitate customized fabrication, but the literature still lacks consensus on how to balance cost, biocompatibility, and reproducibility. These gaps highlight the need for systematic evaluation of concentric geometries within motor rehabilitation contexts.

ICS has also been explored as a means of improving comfort and reaching deeper muscle layers by lowering skin impedance through medium-frequency carriers. While most existing studies have focused on analgesic outcomes, its possible role in motor rehabilitation has only recently been suggested. Moreover, when ICS is combined with traditional side-by-side and concentric electrode configurations, it could potentially allow modulation of the interference area, providing greater control over the spatial distribution of the electric field. This integration may enhance both the selectivity of the evoked movements and the comfort perceived during

stimulation, further supporting its potential value in functional motor applications.

The reviewed evidence indicates that future research should investigate integrated strategies that enhance focality and comfort while maintaining low system complexity. In particular, combining geometric optimization of electrodes with medium-frequency stimulation and accessible fabrication processes appears promising but remains insufficiently explored. Addressing this gap motivates the present study, which aims to evaluate these approaches within a unified framework for upper-limb neurorehabilitation.

Chapter 3. Objectives

3.1. Hypothesis

"The use of interferential currents and concentric electrodes for surface electrical stimulation of the forearm improves finger movement selectivity, quantified through the range of motion, and reduces stimulation discomfort in the visual analog scale compared to traditional square electrode stimulation".

3.2. General Objective

To evaluate the biophysical and neurophysiological effect of surface electrical stimulation of the forearm using custom-shaped concentric electrodes and interferential currents on finger movement selectivity and stimulation comfort.

3.3. Specific Objectives

- Evaluate and characterize concentric electrode designs and compare them to square electrodes using a finite element method (FEM) approach and mathematical models of nerve axons.
- Design a simple fabrication process for prototyping personalized electrode geometries based on 3D printing for small-scale applications.
- Evaluate the effectiveness of movement control and patient comfort of transcutaneous electrical stimulation with concentric electrodes and interferential currents through testing on healthy subjects.

3.4. Scope and Limitations

The development of this thesis will include results obtained through *in-silico, in-vitro, and in-vivo* studies involving healthy subjects. Clinical trials with follow-up on patients with neurophysiological pathologies will be excluded. Engineering tools will be studied and proposed to evaluate the effects generated in individuals using measurement instruments. The results, as well as the advantages and disadvantages of potential applications, will then be analyzed and presented.

3.5. Publications

Journal Publications in Review

Javier Sáez, Francisco Saavedra, Rodrigo Osorio, Martín Westermeyer, James Fitzgerald, Brian Andrews and Pablo Aqueveque. "Biophysical and Functional Evaluation of Concentric Electrodes for Localized Non-Invasive FES". IEEE Transaction on Neural Systems and Rehabilitation Engineering, 2025.

Journal Publications

Rodrigo Osorio, Jack Edmondson, Siobhan Mackenzie Hall, Francisco Saavedra, **Javier Sáez**, Adrian Poulton, James FitzGerald, Pablo Aqueveque, Brian Andrews, Jonathan Jarvis, "Characterization and Evaluation of Interferential Current Stimulation for Functional Electrical Stimulation". Artificial Organs, May 2025, doi:10.1111/aor.15027.

Conference Papers

Javier Sáez, Francisco Saavedra, Rodrigo Osorio, Brian Andrews, Pablo Aqueveque, Design Parameters of Concentric Electrodes: A

Simulation Study to Optimise Non-invasive Functional Electrical Stimulation, 15th Vienna International Workshop on FES & 30 years IFESS Anniversary, 2025, Vienna, Austria.

Siobhan Mackenzie Hall, **Javier Sáez**, Panagiotis Tsakonas, Rodrigo Osorio, Francisco Saavedra, Pablo Aqueveque, James FitzGerald, Brian Andrews, AI electrode and stimulus design for FES research: a pilot study, 15th Vienna International Workshop on FES & 30 years IFESS Anniversary, 2025, Vienna, Austria.

Javier Sáez, Francisco Saavedra, Rodrigo Osorio, Martín Westermeyer, James Fitzgerald, Brian Andrews and Pablo Aqueveque. "3D-Printed Electrode Fabrication for Functional Electrical Stimulation (FES): Prototyping Concentric Electrodes". IEEE EMBC 2024, Orlando, FL, USA. DOI 10.1109/EMBC53108.2024.10782379

Javier Sáez, Paulina Ortega-Bastidas, Francisco Saavedra, Soledad Luarte-Martínez, Brian Andrews and Pablo Aqueveque. "Effects of Interferential Currents on Motor Function and Muscle Strength: A Systematic Review". IFESS 2024, Bath, UK. https://doi.org/10.1111/aor.14902

Rodrigo Osorio, Siobhan Mackenzie Hall, Jack Edmonson, Francisco Saavedra, **Javier Sáez**, Brian Andrews, James Fitzgerald, Adrian Poulton, Jonathan Jarvis, and Pablo Aqueveque. "Motor and Sensory Response of ICS vs Conventional FES: Comparison Between Two Electrode Configurations", IFESS 2024, Bath, UK. https://doi.org/10.1111/aor.14902

Chapter 4. Methodology

The methodology of this thesis focuses on four fundamental stages. The first stage involves the design of various electrode geometries based on concentric electrodes, using specific design considerations. The second stage corresponds to the modeling of the electrical behavior and effects of the previously designed electrodes through a finite element method (FEM) and nerve axon models. During this stage, the primary effects produced by the concentric electrode were evaluated and compared in-silico to traditional square electrodes. The third stage focuses on prototyping of the previously evaluated designs. Additive manufacturing techniques were used to develop the electrodes and validate their performance. Finally, the fourth stage consists of in-vivo testing on healthy subjects, aimed at evaluating the effects of the proposed techniques in real-world conditions. The methodological framework is summarized in the following schematic (Fig. 4.1.):

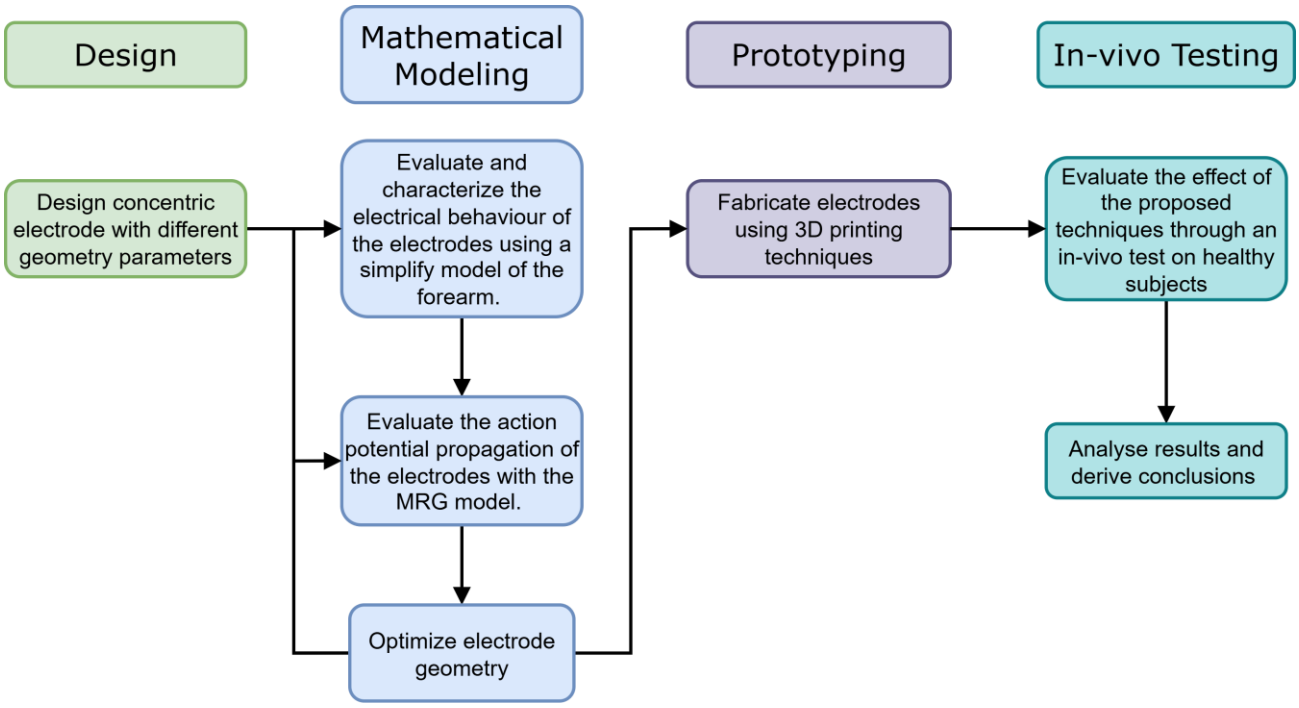

Fig. 4.1. Schematic of the Methodology for Thesis Development.

4.1. Electrode Modeling

To mathematically characterize the behavior of the electrodes with biological tissue, two tools were used. The first is the finite element method (FEM), and the second is the McIntyre–Richardson–Grill (MRG) axon model. This stage enables the prediction of the nervous system's response to electrical stimuli, allowing for an evaluation of how different parameters influence the initial objective. The simulation strategy employed in this workflow draws upon established multiscale modelling principles in the field of neurostimulation [77]. Finite element analysis and axonal modelling are

applied in a unified manner to enable physiologically relevant assessment of electrode performance [78], [79], [80], [81].

4.1.1 Finite Element Method

The FEM modeling was employed to evaluate the electrical behavior of biological tissues in response to surface electrical stimulation. Simulations were carried out using COMSOL Multiphysics® 6.1 (Burlington MA, USA) in conjunction with LiveLink™ for MATLAB® R2023a (Natick MA, USA), on a workstation equipped with an Intel® Core™ i7-10700 processor, 32 GB of RAM, and an NVIDIA GeForce GTX 1080 Ti GPU.

A simplified, anatomically representative model of the human forearm was constructed, comprising the primary tissue layers—skin, subcutaneous fat, and muscle—as well as two bones (ulna and radius) and three peripheral nerves (median, ulnar, and radial). The nerves were embedded within the muscle layer, with spatial positioning based on anatomical references: the median nerve was placed centrally, while the ulnar and radial nerves were offset laterally by +1.6 cm and −1.1 cm from the central axis, respectively. To simulate the electrode–tissue interface, a hydrogel layer was incorporated between the stimulation electrode and the skin surface. The electrode was placed on the anterior surface of the model, targeting the median nerve. The dimensions of each layer are provided in Table 4.1.

Dielectric properties (electrical conductivity and relative permittivity) were assigned to each domain based on literature values at 50 Hz [78], [82], matching the primary frequency component of the stimulation waveform . These values were extracted from the IT’IS Foundation database and are

detailed in Table 4.2. The model domains included: skin, fat, muscle, nerve, bone, hydrogel, and the electrode material [48], [82].

Table 4.1. Dimensions of the Components in the FEM Model.

Component	Dimension	Value (mm)
Nerves	Diameter	3
Bones	Diameter	15
Skin	Thickness	1.8
Fat	Thickness	0.5
Muscle	Major axis diameter	28.15
	Minor axis diameter	22.15
	Eccentricity	0.85*

*Eccentricity doesn´t have units.

Table 4.2. Isotropic Dielectric Properties of the Domains in the FEM Model at 80 Hz Extracted from IT'IS Foundation [83].

Component	Permittivity	Conductivity (S/m)
Nerves	6.85E+5	2.79E-2
Bones	6.46E+3	2.01E-2
Skin	1.14E+3	2.00E-4
Fat	2.12E+5	4.06E-2
Muscle	1.20E+7	2.56E-1
Hydrogel [78], [82]	1	3.80E-3
Electrode [78], [80]	1	8.00E6

The models generated for the concentric and square electrodes are shown in Fig. 4.2. In this figure, two of the electrode configurations used can be observed, along with the layers of the model in a transverse plane. These electrode where placed at the centre of the model targeting the median nerve.

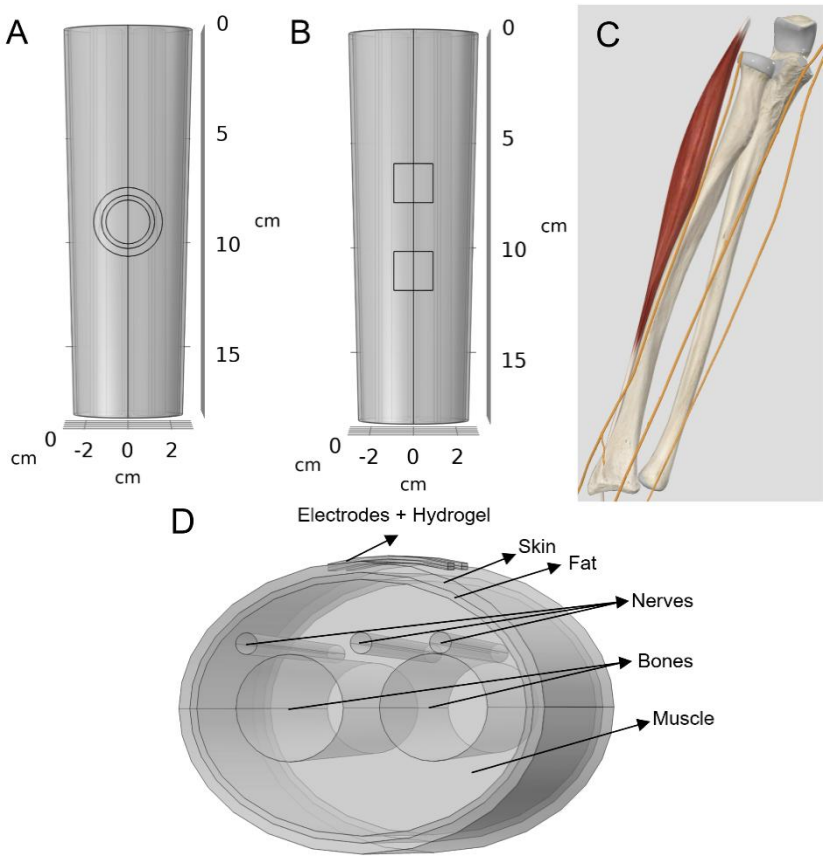

Fig. 4.2. 3D Simplified Forearm Model Created in COMSOL Multiphysics 6.1, a) Superior view with concentric electrode and b) square, c) Anatomical reference extracted from 3D4Medical [84] c) Transverse view with labeled model layer.

The model was discretized using an extra-fine tetrahedral mesh, comprising approximately 2.1 million elements, to ensure spatial resolution adequate for capturing electric field gradients near the target nerves. The simulations were configured using the Electric Currents interface of the AC/DC module in a stationary (time-independent) regime. A constant current was applied at the active electrode via a von Neumann boundary condition to simulate a uniform current density [54]. The return electrode was grounded

using a Dirichlet boundary condition, while all other external surfaces were treated as electrically insulating [54].

The system calculates the electric potential using the defined boundary conditions and the dielectric properties of the materials by solving the quasi-static field equations through conductivity (1), and computing the electric field produced by the electrode configurations (2). Note that the capatice component of the equation is zero, since we are computing a time-independent study, which have been evaluated and neglected for this type of studies [80].

$$-\nabla \cdot (\sigma \nabla V) - \nabla \cdot \left(\varepsilon_0 \varepsilon_r \nabla \frac{\partial V}{\partial t}\right) = 0 \quad \textbf{(1)}$$

$$\vec{E} = -\nabla V \quad \textbf{(2)}$$

where, $-\nabla \cdot (\sigma \nabla V)$ represents the divergence of the conductive (ohmic) current density. This term dominates at low frequencies and under steady-state conditions, where current flow is governed primarily by the spatial distribution of conductivity across tissues such as skin, fat, muscle, and nerve. The second term accounts for the displacement current arising from the capacitive properties of biological tissues. This term is neglected for low frequencies. (2) represents the electric field vector as the negative of the voltage gradient.

The calculated electric potential from the FEM is subsequently used as input for the nerve axon model, whose development is detailed in the subsection.

From these FEM models, two distinct studies were conducted. The first study focused on comparing the electric field distribution generated by

the concentric electrode and the square electrode. The second study evaluated the electrical effects of the concentric electrode designs with variations in their geometry and electrical parameters. Specifically, different electrode sizes and varying distances between electrodes were analyzed. In all studies, the electrodes were designed to maintain equal areas between the anode and cathode. This ensures comparability with traditional square or circular electrode configurations, which typically employ equal active areas for both electrodes.

A. Electrode Comparison Side-by-side and Concentric

As described previously, a comparative study was carried out between square side-by-side electrodes and concentric ring electrodes. In this step, the main characteristics of both electrodes will be analyzed in terms of electric field and activating function. These values are going to be extracted in different planes and lines. A to-scale drawing of the electrodes can be seen in Fig. 4.3 and its dimensions on Table 4.3. These dimensions were determined following an iterative design process, where the geometry of the concentric electrode was optimized to improve the outcomes. This process was conducted in the second FEM study: Effects of Concentric Electrodes Design Parameters with the integration of the MRG model.

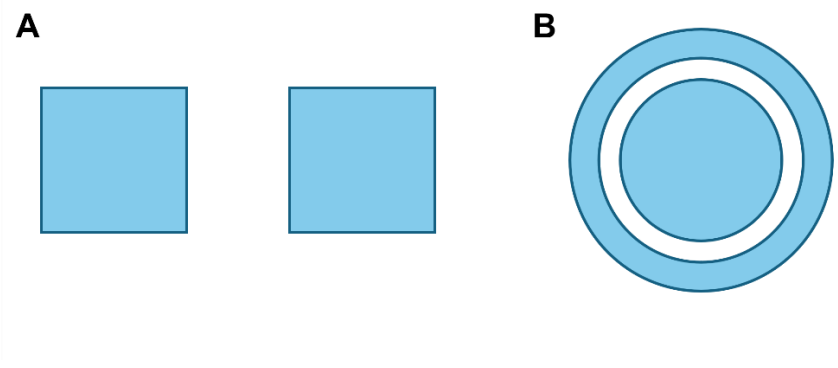

Fig. 4.3. To-Scale Electrodes Used in the Comparative FEM Study, a) Square electrodes, b) Concentric electrodes.

Table 4.3. Dimensions of the Electrodes in the Comparative Study.

Electrode	Dimension	Value (mm)
Square	Side	$10\sqrt{\pi}$
Concentric	Central Circumference Radius	10
	Internal Ring Radius	12.2
	External Ring Radius	15.75

The resulting electric field distribution was analyzed in both longitudinal and transverse anatomical planes to evaluate spatial concentration and focality across tissue layers and surrounding nerves. To quantify this focality, the Focality Index $\mathcal{F}(r)$ was introduced, representing the proportion of total electric field magnitude within a given radius r from the stimulation target (3) [85]:

$$\mathcal{F}(r) = \frac{\sum_{n\in\mathcal{T}(r)} |E(r_n)|}{\sum_n |E(r_n)|} \quad \textbf{(3)}$$

Here, $\mathcal{T}(r)$ is the set of mesh nodes located within radius r of the target. $E(r_n)$ is the electric field value at that radius. The half-maximum radius $r_{0.5}$ defined by $\mathcal{F}(r) = 0.5$ was used as a comparative metric of spatial confinement.

To evaluate the probability for neural excitation, the activating function (AF) was calculated, following the definition by Rattay, as the second spatial derivative of the extracellular potential along the nerve axis:

$$AF = \frac{\partial^2 V}{\partial x^2} \tag{4}$$

Positive values of AF indicate regions of membrane depolarization, while negative values correspond to hyperpolarization, serving as a proxy for stimulation efficacy and spatial selectivity [86], [87].

Additionally, the AF Spread metric was introduced to characterize the geometric dispersion of neural excitation within each nerve. This metric captures the spatial extent of depolarizing activation regions (where AF>0) and is defined as the weighted standard deviation of the spatial coordinates of active elements, with weights proportional to their AF magnitude:

$$\mathrm{AF}_{\mathrm{spread}} = \sqrt{\sum_{i \in \Omega_{\mathrm{AF}>0}} w_i \cdot |\vec{x_i} - \vec{\mu}|^2} \tag{5}$$

In this expression, $\vec{x_i}$ represents the position of the i-th depolarizing element, $\vec{w_i}$ is the normalized weight based on the local AF value, and $\vec{\mu}$ is the weighted centroid of the depolarizing region. This formulation ensures that regions with stronger influence contribute more to the spread, making the metric physiologically relevant.

These modeling procedures allowed for a physiologically grounded, quantitative comparison between electrode geometries.

B. Effects of Concentric Electrodes Design Parameters

A second FEM study was conducted to assess how the different designs parameters of the concentric electrodes affect the electrical behavior within the biological tissue and neural activation. For this study, two groups of electrodes were created; different sizes of electrodes and different inter-electrode distances (I-ED), as is shown in Fig. 4.4, the dimensions of each design are shown on Table 4.4. In this study current density below the electrodes, depth of the electrical stimulus in the tissue, and frequency effects were analyzed. The input current was fixed at 5 mA for all simulations. The effect of the different designs in axon activation was analyzed with the MRG axon model. Based on the results obtained for each concentric electrode design, the optimal configuration for the application was selected.

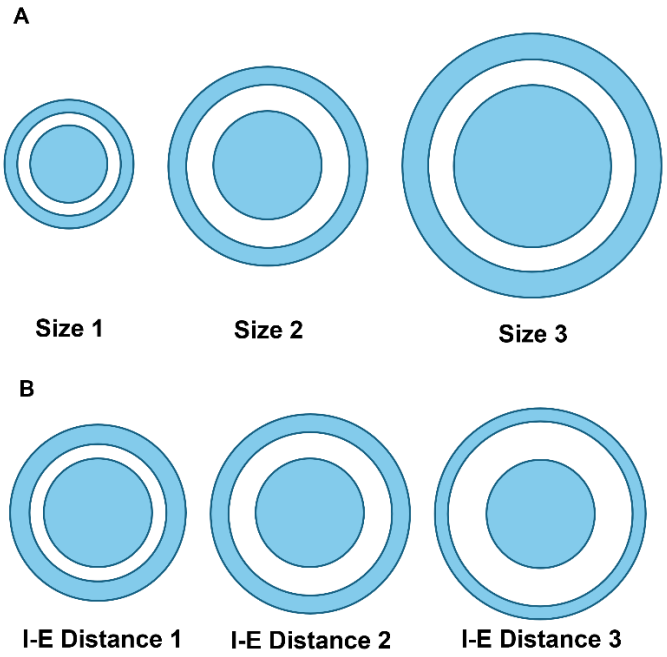

Fig. 4.4. To-Scale designs of concentric electrodes for different sizes and B) inter-electrode distances.

Table 4.4. Dimensions of Different Designs of Concentric Ring Electrodes

Design	Central Electrode Radius (mm)	Ring Inner Radius (mm)	Ring Outer Radius (mm)	Area (mm^2)
Size 1	7.5	10	12.5	353.43
Size 2 and I-ED 2	10	15	18	625.18
Size 3	15	20	25	1413.72
I-ED 1	10	12	15.6	626.31
I-ED 3	10	17.32	20	628.37

To further evaluate the electrical performance of the concentric electrode designs, current density was measured along a longitudinal axis directly beneath the electrode surface. This analysis aimed to assess the uniformity of current distribution within the tissue, as spatial variability in

current density can influence both stimulation efficacy and patient comfort. A key metric used in this evaluation was the normalized peak-to-average ratio, which quantifies the degree of non-uniformity (1). This ratio was computed using the maximum, minimum, and average current density values (J) along the defined path. Higher values of this ratio are indicative of greater spatial concentration of current, which may correspond to increased risk of localized skin discomfort or hot spots during stimulation [54].

$$k = \frac{J_{max} - J_{min}}{J_{avg}} \quad \textbf{(6)}$$

To evaluate the effect of stimulation frequency on tissue impedance and voltage requirements, a frequency sweep analysis was conducted using the FEM model. Frequency values ranged from 1 Hz to 100 Hz, representative of conventional FES protocols, and from 1 kHz to 10 kHz, typical of ICS. For each frequency, the system was simulated under constant current stimulation to assess voltage variations across the tissue domain. The frequency sweep was assessed using the design Size 2 and I-ED 2.

Both studies were performed using COMSOL Multiphysics® 6.1 in combination with LiveLink™ for MATLAB® R2023a, which enabled automated parameter sweeping and data extraction. The scripting interface allowed for efficient iteration over different parameters, significantly accelerating the simulation workflow.

4.1.2 Nerve Axon Model

To assess the neural response elicited by the different electrode configurations, simulations were performed using the MRG model of a

myelinated Aα motor fiber [88]. This model, derived from the foundational Hodgkin–Huxley framework, provides a biophysically detailed representation of action potential initiation and propagation in mammalian motor axons. It accounts for the dynamics of ion channel gating, membrane capacitance, and intracellular axial current, making it particularly suitable for evaluating extracellular stimulation in neuroprosthetic applications. A general schematic of the model is shown in Fig. 4.5.

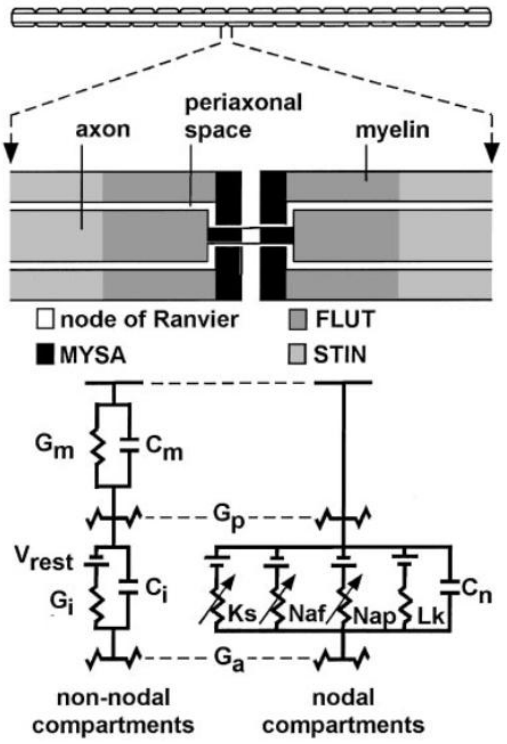

Fig. 4.5. Schematic of the MRG Model for Myelinated Motor Axons in Mammals [88].

The model was implemented in MATLAB® R2023a using a customized version of the AxonSim platform, adapted to accept spatially resolved extracellular potential data exported from the FEM simulations [89]. For each of the three nerves modeled in the forearm—median, ulnar, and radial—a single axon was positioned at the center of the nerve cross-section.

Each axon was modeled with a diameter of 16 µm, comprising 134 nodes of Ranvier, consistent with the morphological parameters of Aα motor fibers [88].

The extracellular stimulation was applied in the form of a monophasic pulse with a duration of 200 µs. The extracellular potentials computed from FEM were interpolated across the axonal compartments and integrated into the transmembrane voltage differential equation:

$$C_m \frac{dV_m}{dt} = -I_{\text{ion}} + I_{\text{axial}} - I_{\text{ext}} \quad (7)$$

where C_m is the membrane capacitance, I_{ion} is the ionic current through voltage-gated ion channels, I_{axial} is the axial current flowing between compartments, I_{ext} is the externally applied stimulus derived from the FEM model and $\frac{dV_m}{dt}$ is the change of membrane potential in time [88]. This formulation captures the interplay between external electric fields and internal axonal dynamics, enabling accurate prediction of action potential initiation.

This modeling approach was applied to the two simulation studies described previously. For the electrode geometry comparison between square and concentric electrodes, the MRG axon model was used in conjunction with an automated threshold search implemented via LiveLink™ for MATLAB. The input current was incrementally increased in 0.1 mA steps until each nerve reached activation, allowing assessment of the electrode's selectivity range based on the recruitment pattern of the median, ulnar, and radial nerves:

- **High Selectivity Range (HSR):** Only the target nerve was activated.
- **Medium Selectivity Range (MSR):** Two nerves were activated simultaneously.
- **Low Selectivity Range (LSR):** All three nerves were recruited.

In the second study, which evaluated the effect of geometric parameters in concentric electrode designs, a fixed input current of 5 mA was applied across all configurations. The MRG model was used to determine which nerves were activated under each design condition, enabling the analysis of how changes in electrode size and inter-electrode spacing influence stimulation focality and neural recruitment.

4.2. Prototyping Process

The prototyping process for the previously designed electrode consists primarily of two main parts. The first part involves the printing process of the electrode, and the second part focuses on the assembly of the electrode using the various layers.

4.2.1 Substrate Printing

The previously designed electrode was modeled in 3D using CAD software. Various structural considerations were made for electrode design. The first was the inclusion of space for the electrode connection. Additionally, it was determined that the ring-shaped structure separating the electrodes would have a greater height than the anode and cathode. A rectangular structure was also designed at the bottom of the electrode to accommodate the connection cables.

Once the electrode was designed, it was printed using a Formlabs Form 3+ printer with Formlabs flexible resin FLFLGR02, selected for ergonomic purposes and its application in wearable prototypes [90]. A layer height of 100 μm was chosen as a balance between detail and printing speed. The printing software automatically adjusted the printing speed based on the geometry of the electrode. After printing was completed, the post-processing steps included cleaning the printed electrodes with isopropyl alcohol for 10 minutes to remove uncured resin. Once dried, the electrodes were cured under UV light at 60°C for 60 minutes using the Form Cure system to ensure optimal mechanical properties.

4.2.2 Electrode Assembly

Once the substrate printing process was completed, the electrodes were assembled. For this, the substrate was manually painted using 117-23 Ag/AgCl conductive paint from Creative Materials (Albany NY, USA). This type of paint is specifically designed for medical purposes, particularly for electrical stimulation applications such as TENS, as indicated in the technical data [91]. Subsequently, a gel layer was added to the top of the electrode to ensure a stable contact interface with the skin (AG735, Axelgaard Manufacturing Co. Fallbrook, CA, USA). This gel layer was precisely cut to match the dimensions of the designed electrode using a laser cutter. Connections were established using a standard 2 mm pin connector with conductive thread. The various layers involved in the fabrication process are shown in Fig. 4.6.

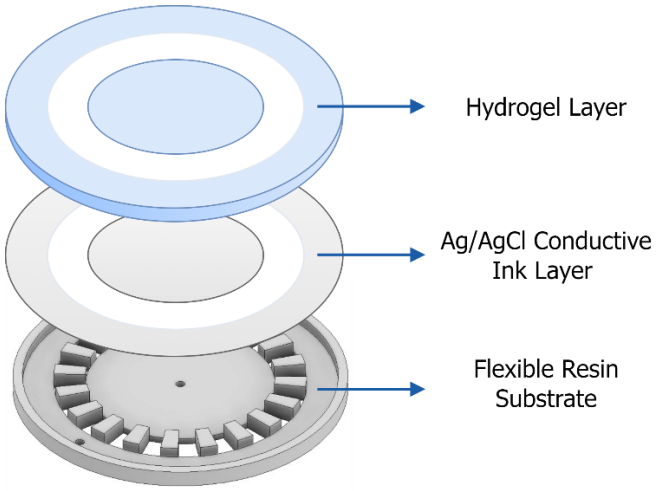

Fig. 4.6. Layered Visualization of the 3D-Printed Electrode: The first layer consists of the flexible resin substrate, the second layer is the active material made of Ag/AgCl conductive paint, and the final layer is the gel.

4.2.3 Impedance Measurement

To evaluate the electrical characteristics of the electrode–skin interface, impedance measurements were performed for both the custom-fabricated electrodes (concentric and square) and a commercially available square electrode (Axelgaard UltraStim X). This protocol is shown on Fig. 4.7. The objective of this protocol was to characterize the frequency-dependent impedance behavior of each configuration under standardized, physiologically relevant conditions. All electrode types were normalized to have equivalent active surface areas and consistent anode–cathode distributions, allowing for a direct comparison of geometric effects without confounding surface area differences. The skin site selected for measurement was the anterior forearm, replicating the typical electrode placement used in the stimulation experiments. Prior to each measurement, the skin was cleaned

with 70% ethanol to ensure a uniform contact surface by removing oils and surface contaminants.

Measurements were conducted using a Hioki IM3536 precision LCR meter (Hioki E.E. Corporation, Japan), operating in impedance mode. A constant current stimulus of 1 mA was applied while sweeping across a frequency range from 10 Hz to 100 kHz. This range was selected to capture the impedance characteristics relevant to both low-frequency biphasic stimulation and medium-frequency interferential currents, as well as the principal spectral components of a typical 200 µs stimulation pulse. The instrument recorded the resulting voltage response, from which the complex impedance (Z) was computed as a function of frequency. These measurements provide insight into the interface behavior, including capacitive effects and tissue-electrode coupling, which are critical for optimizing stimulation comfort and efficacy.

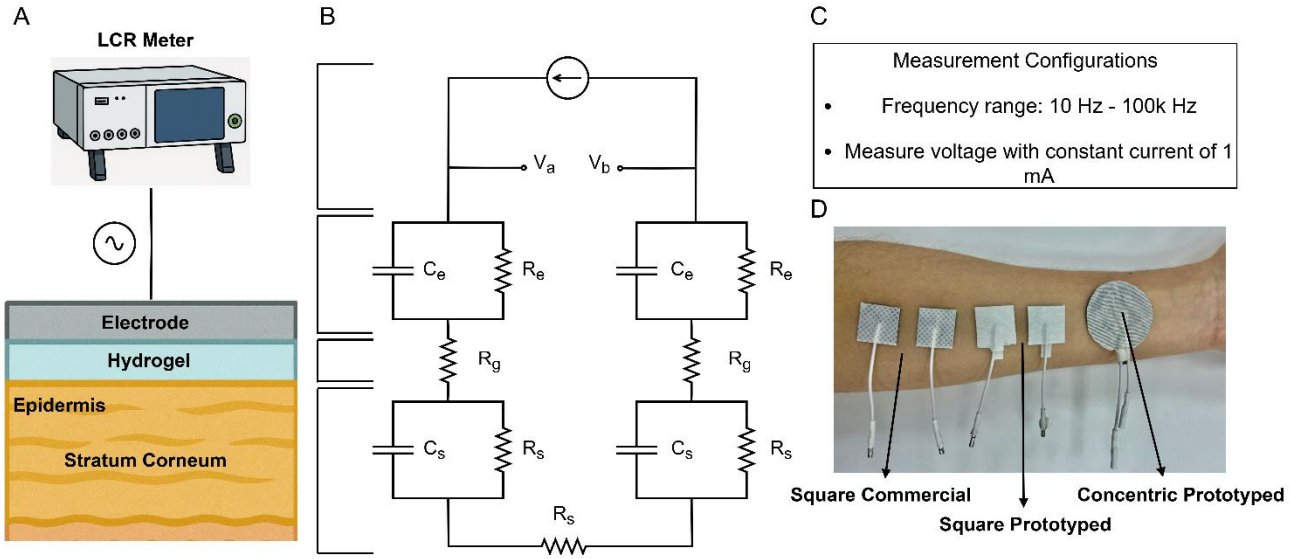

Fig. 4.7. Impedance measurement setup and electrode comparison. A) Schematic representation of the electrode–skin interface model used for impedance measurements. B)

Equivalent electrical circuit model representing the interface C) Measurement protocol parameters and D) Photograph of the electrodes evaluated applied to the anterior forearm.

4.3. In-vivo Testing

This section details the experimental procedures conducted during the in-vivo testing phase. Three distinct tests were designed to evaluate the physiological responses to different stimulation strategies. Each test corresponds to a specific stimulation method, allowing for a comprehensive comparison in terms of selectivity, range of motion, and user comfort.

4.3.1 Set-up y and Testing Procedure

This subsection describes the equipment and materials used for the in-vivo testing protocol. Two stimulation devices were employed: the RehaMove 2 (Magdeburg, Germany) stimulator for biphasic electrical stimulation, and the Ultima Neo Pro (Akron OH, USA) for ICS. Stimulation was applied using two electrode geometries: concentric electrodes and square electrodes. Prior to each test, motor points corresponding to the desired functional movements were identified individually for each subject and carefully recorded to ensure consistent electrode placement. A summary of the tests, measurement equipment, and objectives is provided in Table 4.5.

Table 4.5. Summary of the tests to be performed, measuring instrument and the objective of the measurement.

Evaluation Parameter	Measurement Instrument	Objective
Range of Movement	Perception Neuron Studio Gloves	Evaluate the range of motion and selectivity of predefined functional movements
Discomfort	Visual Analog Scale (VAS)	Evaluate subjective pain response during tests

The in-vivo testing was conducted on 12 healthy adult volunteers (6M, 6F). Each participant underwent stimulation using three distinct methods to enable comparative analysis. The protocols included: (1) biphasic stimulation with traditional square side-by-side electrodes (50 Hz, 200 μs), (2) biphasic stimulation with concentric electrodes (50 Hz, 200 μs), and (3) ICS delivered using both square and concentric electrode configurations (CH1: 4000 Hz, CH2: 4050 Hz). This comprehensive setup allowed for the evaluation of stimulation efficacy, selectivity, and subjective comfort across different electrode geometries and waveform types.

The experimental protocol was approved by the institutional ethics committee of the Universidad de Concepción (approval code: CEBB 1605-2024), and written informed consent was obtained from all participants prior to data collection. Volunteers were excluded if they had any history of neuromuscular disorders, upper-limb injuries, dermatological conditions at the stimulation site or any known contraindications to electrical stimulation. The age and anthropometric data are detailed in Table 4.6 and in Fig. 4.8.

Table 4.6. Age and Anthropometric Data of the participants

	Average ± SD
Age	28.00 ± 8.26 years
Forearm Circumference	23.79 ± 2.85 cm
Forearm Large	25.41 ± 1.76 cm
N	12

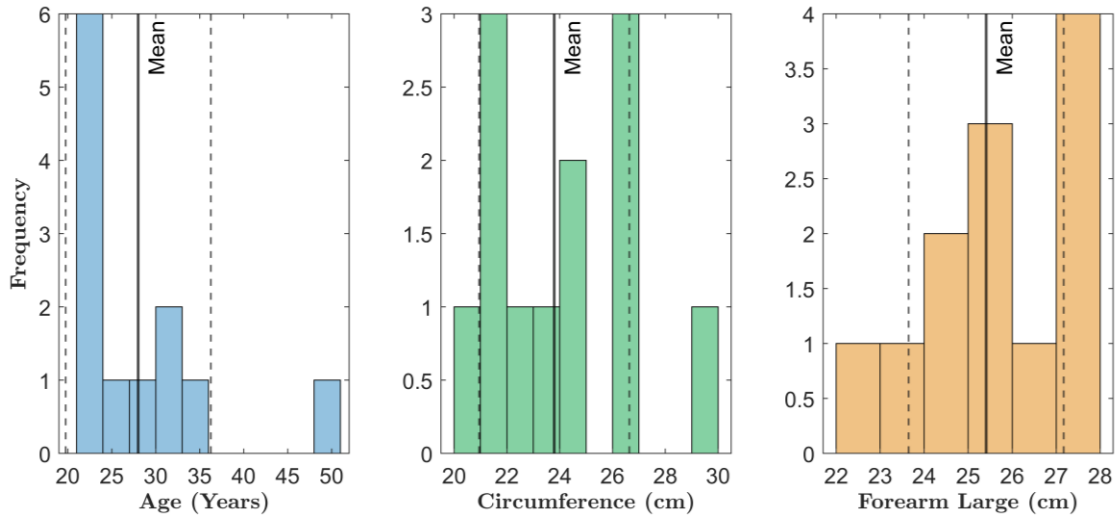

Fig. 4.8. Histogram of age, circumference of the proximal third part of the forearm and forearm large of the participants. The mean value and SD are indicated in the figure.

A. Movement Analysis with Concentric Electrodes

The movement generated by the three stimulation methods was evaluated in the test subjects. Two studies were performed. The first study evaluated the movement generated by the concentric electrode and was compared with the square electrode; the selected movements were:

- Flexion of digits.
- Thumb abduction.

The movements selected for the in-vivo procedures—flexion of digits 4 and 5, and thumb abduction—were chosen due to their importance in assessing the selectivity and functional relevance of the stimulation protocols. The flexion of digits 4 and 5 is particularly useful for evaluating neural targeting, as it involves both superficial and deep muscle layers innervated by different nerves. While the flexor digitorum superficialis (FDS), innervated by the median nerve, contributes to the flexion of all four

fingers, the flexor digitorum profundus (FDP), which is innervated by the ulnar nerve, is specifically responsible for flexing digits 4 and 5. Therefore, the observation of isolated flexion of digits 4 and 5 serves as an indicator of selective ulnar nerve activation. Conversely, if the FDS is also activated, it results in the flexion of digits 2 through 5, indicating broader and less specific stimulation.

The second movement, thumb abduction, plays a critical role in fine motor control, particularly during precision grip tasks. This movement is primarily driven by the abductor pollicis brevis, a superficial muscle innervated by the median nerve. When selectively activated, this muscle produces isolated thumb abduction with little or no influence on the other digits. As such, the presence of isolated thumb abduction offers a clear metric for evaluating the focality and precision of the stimulation strategy.

Electrical stimulation was delivered using the RehaMove 2 stimulator with fixed pulse width, and frequency. The current amplitude was increased from and 2 to 14 mA amplitude. For each subject, the stimulation current was adjusted to 2 mA above the minimal activation threshold required to elicit a visible contraction of the target finger. The movement generated with the threshold and 2 mA above it, were recorded (total of three measurements).

The second in-vivo study compared ICS with conventional biphasic stimulation; both delivered through concentric electrodes. Four stimulation zones (Z1–Z4) were defined by partitioning the proximal third of the forearm into four equal arc segments along one half of its circumference. For each zone, the activation threshold current (i.e., the minimum current required to elicit a visible, repeatable contraction) were measured under both modalities

and compared. Range of motion (ROM) at the fingers will also be quantified. The reduction of the skin impedance and deeper motor unit recruitment afforded by medium-frequency carriers of ICS will produce larger ROM and/or lower activation thresholds than biphasic stimulation in the voltage-controlled stimulator.

The motor points of movement in each patient are assessed, as is shown on Fig. 4.9. The Perception Neuron Studio motion analysis system and Studio Gloves software were used for data capture, as is shown in Fig. 4.10. The Perception Neuron Studio Gloves utilizes IMU sensors to capture acceleration, angular velocity, and magnetic field data, and export the quaternions of the biomechanical model of Axis software for subsequent analysis in MATLAB.

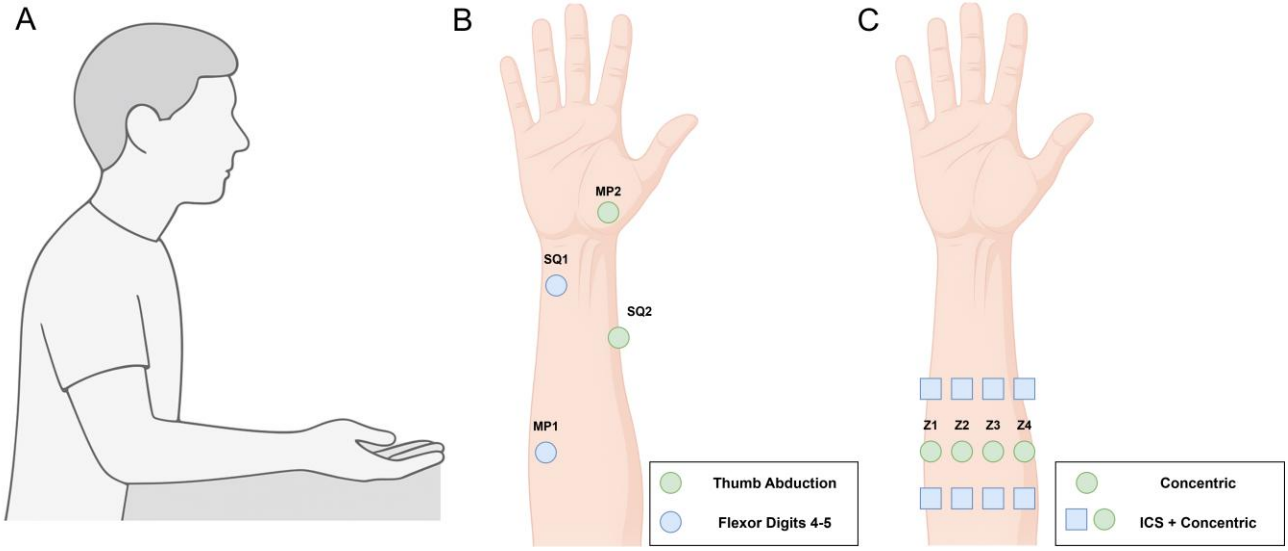

Fig. 4.9. In-vivo procedure. A) Resting position of patients during measurement. B) Motor points for flexion digits 4-5 (blue) and thumb abduction (green), concentric electrode where place in the motos points (MP), square electrodes were placed in MP and SQ as indicated in the figure. C) Zones where the stimulation was applied using biphasic stimulation with concentric electrodes (green) and ICS with concentric electrodes (green and blue).

To ensure accuracy in biomechanical measurements, a calibration procedure was performed prior to each recording session. The system was calibrated using a physical reference axis alignment. The anti-magnetic disturbance setting in Axis Studio was enabled to minimize magnetic field interference. Additionally, recalibration was conducted between movement trials to mitigate signal drift and reduce accumulated noise, ensuring consistent performance of the biomechanical model throughout the data collection process.

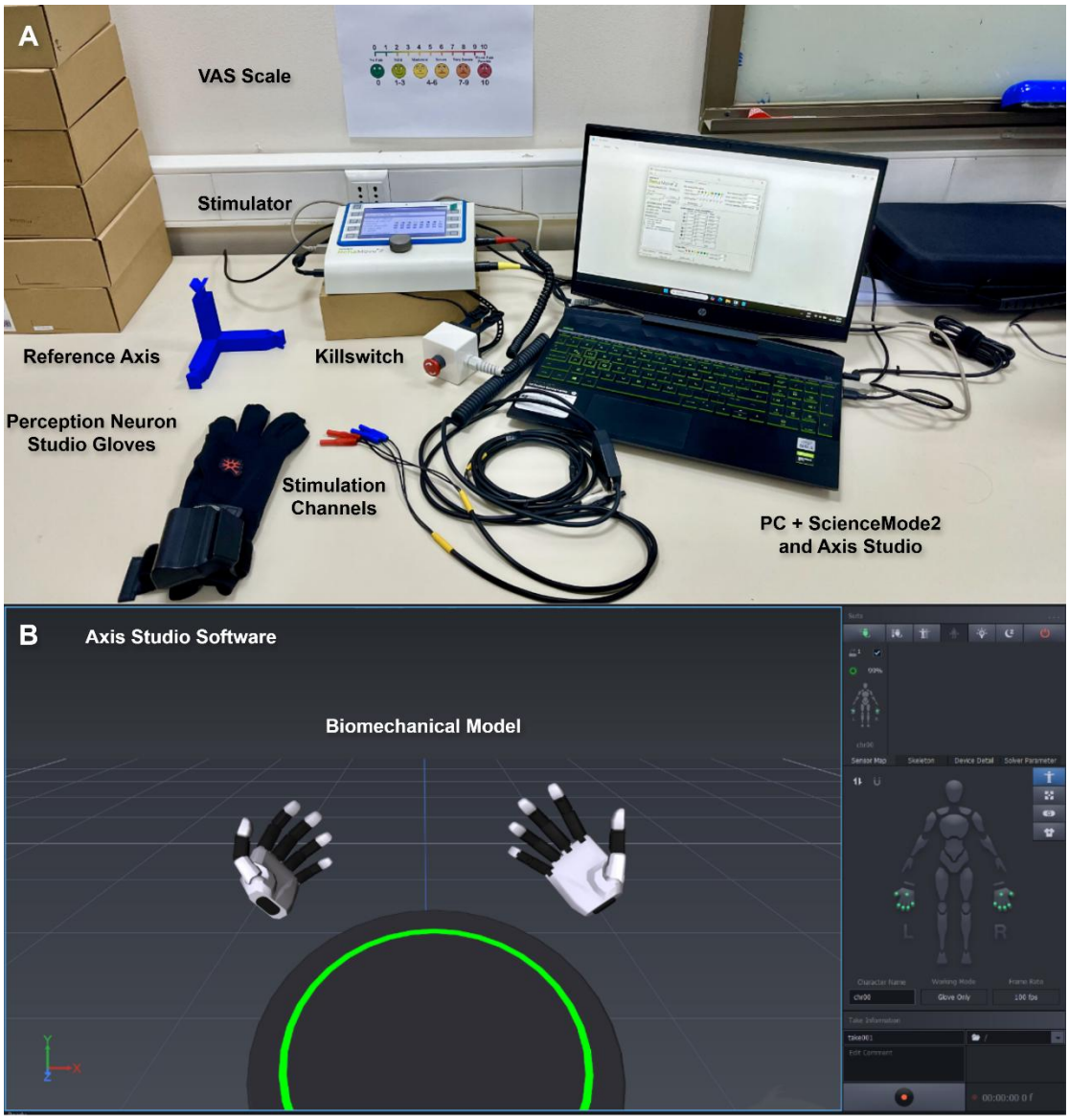

Fig. 4.10. (A) Experimental setup for in-vivo testing, including the stimulator, stimulation channels, emergency killswitch, VAS pain scale, and Perception Neuron Studio gloves for motion capture. The reference axis was used for calibration, and data acquisition was performed using a laptop running Axis Studio software. ScienceMode2 software was employed to communicate stimulation parameters to RehaMove2 stimulator. (B) Visualization of the biomechanical hand model within Axis Studio, used for real-time motion during electrical stimulation trials. system.

The biomechanical flexion angles of the metacarpophalangeal (MCP), proximal interphalangeal (PIP), and distal interphalangeal (DIP) joints were

calculated for digits 2 to 5. Additionally, the thumb abduction angle was assessed [92].

To compute these joint angles from quaternion data, the relative orientation of the distal segment with respect to the proximal segment was first determined using quaternion algebra, as follows (8) [93], [94]:

$$q_{\mathrm{B/A}} = q_A^{\mathrm{conj}} \otimes q_B \quad \textbf{(8)}$$

This approach effectively establishes the proximal segment as the reference frame. Subsequently, the relative quaternions were converted into Euler angles, prioritizing the rotation corresponding to the primary axis of the intended movement (e.g., the X-axis for flexion/extension).

The time-varying joint angles and the corresponding ROM (9) generated by each stimulation method were analyzed for each finger. To evaluate the selectivity and dexterity of the stimulation based on ROM, joint movement was first recorded with the hand in a relaxed, resting position, followed by the application of stimulation. This procedure ensured that the observed motion could be attributed exclusively to the stimulation, allowing the effects on each individual finger to be isolated. These metrics were used to evaluate the selectivity of the induced movements.

$$\mathrm{ROM} = \theta_{\max} - \theta_{\min} \quad \textbf{(9)}$$

To quantitatively assess the functional selectivity of each electrode geometry, a Selectivity Index was calculated using the range of motion (ROM) data of the fingers. This metric evaluates how effectively a stimulation protocol isolates movement to the target (objective) finger

relative to unintended motion in non-targeted fingers. It is defined as the ratio of the ROM of the objective fingers to the cumulative ROM of all other fingers, as shown in (10). The index yields values between 0 and 1, where values closer to 1 indicate higher selectivity. This analysis was performed for each electrode configuration to compare their capacity for precise finger activation.

$$\text{Selectivity}_{\text{index}} = \frac{\text{ROM}_{obj}}{\sum_{\text{Fingers}} \text{ROM}_{Fingers}} \tag{10}$$

B. Subjective Pain Measurement

Subjective pain perception during the various tests were evaluated using the Visual Analog Scale (VAS, Fig. 4.11). This scale is widely used due to its ease of implementation and efficiency in providing reliable results. In this case, the subjective pain perception was assessed in the two studies (i.e., concentric vs square and concentric vs ICS).

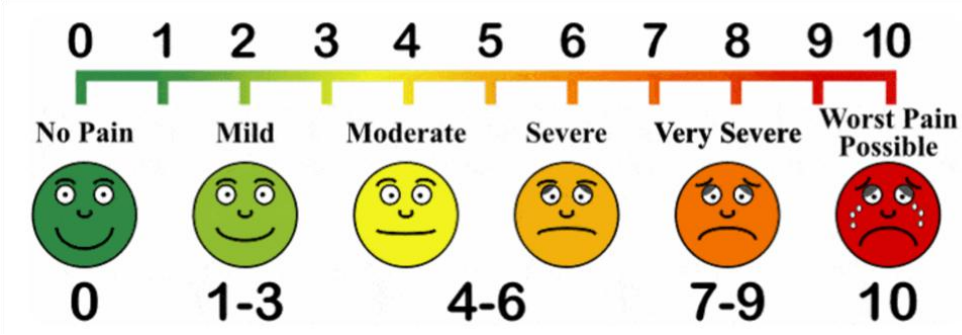

Fig. 4.11. Visual Analog Scale (VAS) for subjective pain perception [95].

Chapter 5. Results and Discussion

5.1. Mathematical Modeling

5.1.1 Electrode Comparison Side-by-side and Concentric

The outcomes from the comparison study using FEM analysis are detailed below. Fig. 5.1 presents a comparative qualitative visualization of the electric field distribution generated by concentric and square electrodes across multiple anatomical planes, highlighting their distinct spatial characteristics and implications for selective nerve stimulation.

Fig. 5.1.A shows 3D surface plots of the electric field magnitude in a longitudinal plane parallel to the course of the nerves. In the case of the concentric electrode (top), the electric field is characterized by a highly localized peak directly beneath the central cathode, with a gradual radial decay as the distance from the center increases. This pattern suggests a more confined stimulation region, predominantly targeting the median nerve. In contrast, the square electrode (bottom) produces two distinct peaks corresponding to the anode and cathode pads, with a broader and more dispersed field profile. This results in stimulation of a wider volume of tissue, encompassing not only the target nerve but also adjacent structures.

The following plots complement the distribution of the electric field. Fig. 5.1.B displays the transverse cross-sectional view of the electric field, providing insight into how each electrode configuration distributes stimulation across tissue depth. The concentric electrode produces a focal electric field that is largely confined to the superficial layers of the forearm,

with the highest intensity concentrated near the skin surface. This phenomenon is closely related to the short distance between the electrodes, causing the current to flow from the anode to the cathode through the upper layers. This superficial distribution results in limited penetration toward deeper structures, such as the median, ulnar, and radial nerves. In contrast, the square electrode generates a broader and deeper field, with peak intensities extending further into the tissue.

Finally, Fig. 5.1 provides contour and vector field plots, revealing both the magnitude and directionality of the electric field. In the concentric configuration (top), field vectors exhibit a radial inward orientation toward the central electrode, confirming the symmetrical and focused nature of the field. Conversely, in the square configuration (bottom), the field vectors follow a linear trajectory from the anode to the cathode, producing a broader field distribution along the longitudinal axis of the arm.

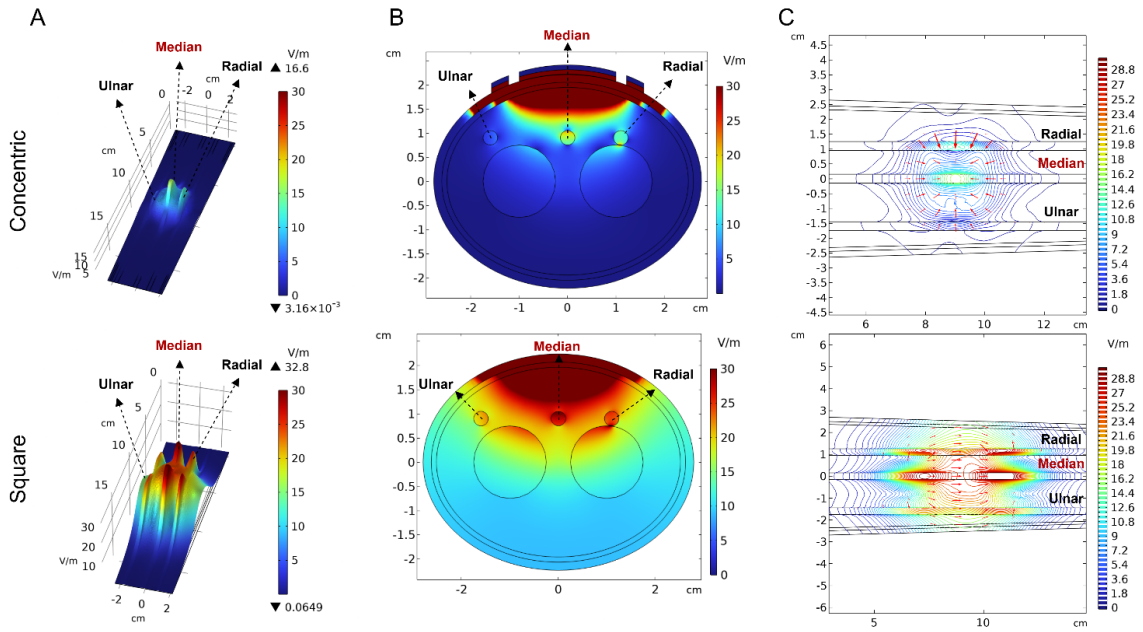

Fig. 5.1. Qualitative visualization of the electric field distribution generated by concentric and square electrodes using finite element modeling. (A) Electric field magnitude in a longitudinal plane parallel to the nerves, represented as a 3D surface plot. (B) Cross-sectional view of the electric field in a transverse plane at the center of the model. (C) Contour and vector field maps showing field direction and intensity.

Overall, the contrasting electric field profiles observed between the concentric and square electrodes underscore a fundamental trade-off between stimulation precision and depth. The concentric electrode offers enhanced spatial control, producing a highly localized field that can facilitate selective activation of superficial neural targets. This characteristic makes it particularly suitable for applications requiring fine motor control or targeted neuromuscular engagement within anatomically dense regions such as the forearm. However, the focal nature of this field inherently limits its penetration into deeper tissue layers, potentially compromising its effectiveness for activating nerves located further beneath the surface needing higher levels of input current that can increase discomfort.

To complement the electric field analysis and enable a nerve-specific evaluation of spatial selectivity, the spatial dispersion of neural activation was quantified using the $\mathrm{AF}_{\mathrm{spread}}$ metric. This measure represents the weighted dispersion of regions where the activating function (AF) is greater than zero (depolarized zones), effectively capturing how concentrated or dispersed the neural depolarization is within each nerve volume.

As illustrated in Fig. 5.2 (Panel A), the concentric electrode consistently resulted in lower $\mathrm{AF}_{\mathrm{spread}}$ values across the median, ulnar, and radial nerves compared to the square electrode. In particular, stimulation of the median nerve exhibited the greatest difference: the concentric configuration achieved a highly confined depolarization zone with an AF_{spread} close to 1 cm, whereas the square electrode produced a much broader spread, exceeding 2.3 cm, despite having a comparable or higher total depolarizing input ($\sum$AF). These quantitative findings are further supported by the 3D visualizations shown in Panel B, which display the normalized activating function along the nerve axis. For the square electrode, the depolarizing region appears spatially diffuse, extending significantly along the nerve. In contrast, the concentric electrode yields a compact and localized activation profile, tightly aligned with the desired stimulation site.

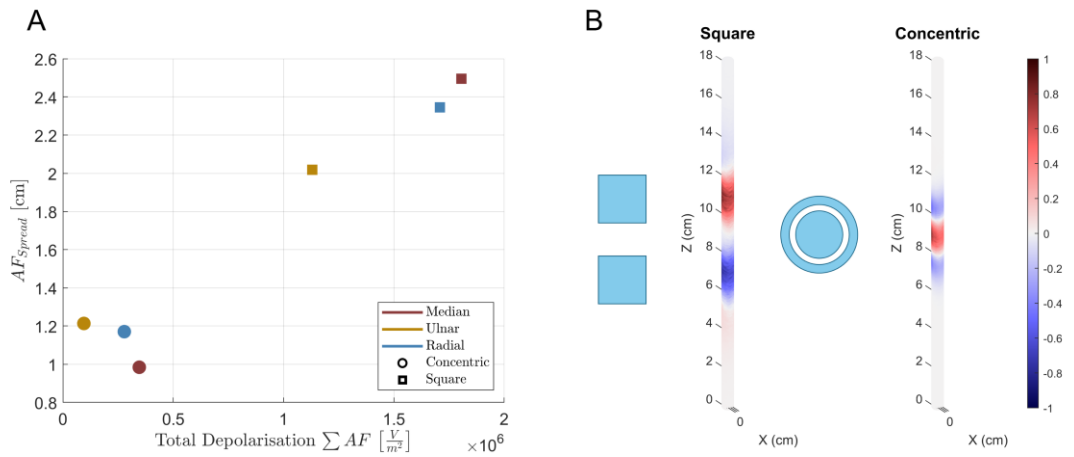

Fig. 5.2. A) Quantitative analysis of activation spread for concentric and square electrodes. The x-axis shows the total depolarization (∑AF), while the y-axis represents the AF_{spread}. Lower values on the y-axis indicate more localized neural activation, while higher values on the x-axis total depolarization. B) 3D visualization of normalized activating function distribution along the nerve axis for both configurations. The concentric electrode produces a more confined and targeted activation profile, while the square electrode exhibits broader, less selective stimulation.

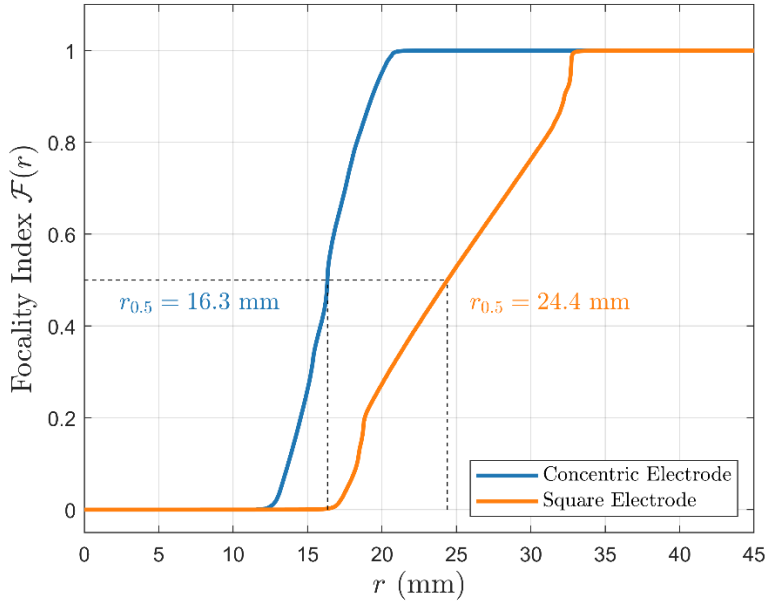

Fig. 5.3. Focality index as a function of radial distance r for the concentric and square electrodes. The concentric electrode demonstrates significantly higher focality, with a smaller half-maximum radius $r_{0.5}$ = 16.3 mm, compared to the square electrode $r_{0.5}$ = 24.4 mm. A lower $r_{0.5}$

indicates a more spatially confined electric field, emphasizing the enhanced precision of the concentric configuration.

Fig. 5.3 presents the focality index $\mathcal{F}(r)$, which quantifies the spatial confinement of the electric field produced by each electrode configuration. The index describes the cumulative distribution of electric field magnitude as a function of radial distance from the stimulation center. A steeper curve reflects higher spatial confinement. The concentric electrode demonstrated a notably sharper transition, reaching the 50% cumulative electric field energy threshold $\mathbf{r_{0.5}}$ at 16.3 mm. In contrast, the square electrode exhibited a more gradual rise, with $\mathbf{r_{0.5}}$ extending to 24.4 mm. This difference highlights the superior focality of the concentric geometry, indicating that a greater proportion of the electric field is concentrated near the electrode center, while the square electrode disperses its field over a broader area. These findings support the qualitative observations from the previous figures and provide quantitative evidence of the enhanced spatial selectivity achieved with concentric electrode designs.

As illustrated in Figure 5.4 A, MRG simulations revealed distinct recruitment profiles for the two electrode geometries. With concentric stimulation, the median nerve was selectively activated at 4.1 mA, with higher thresholds for the radial (5.2 mA) and ulnar (14.1 mA) nerves. This yielded a high-selectivity range (HSR) of 2.7 mA before co-activation of the next nerve.

In contrast, the square electrode activated the median nerve at a lower threshold (2.5 mA), but with a narrow HSR of only 0.6 mA. Both the radial

and ulnar nerves were recruited at 3.1 mA and 4.2 mA, respectively, indicating reduced selectivity and earlier off-target activation.

Figure 5.4 B depicts the time evolution of membrane potentials across nodes of Ranvier, highlighting the spatial extent of axonal depolarization for each electrode type. In the concentric configuration (left panel), depolarization is well-localized and propagates as a confined wave along the axon, consistent with focused action potential initiation. Conversely, the square electrode (right panel) induces a broader and less spatially restricted membrane response, indicating a wider zone of neuronal recruitment.

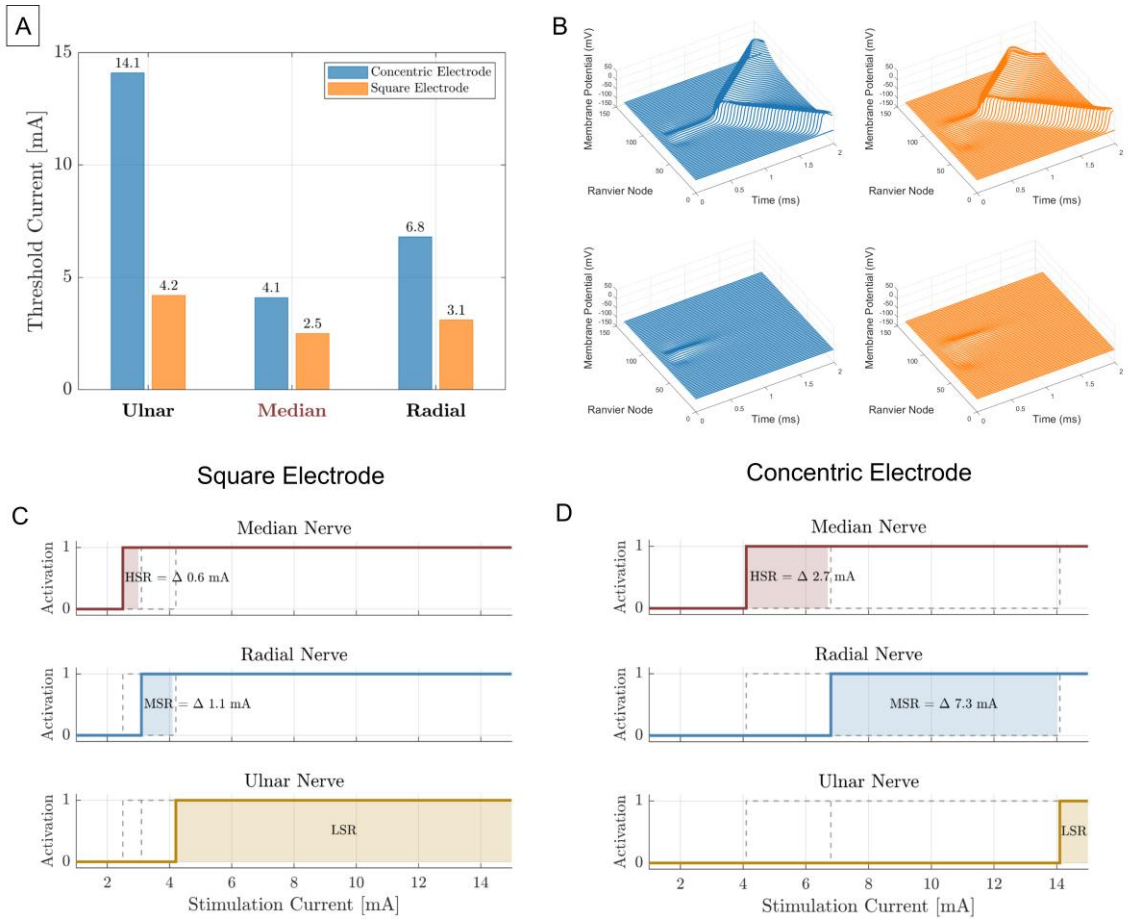

Fig. 5.4. In-silico evaluation of nerve activation with concentric and square electrodes using the MRG axon model. (A) Activation thresholds for ulnar, median, and radial nerves. (B) Action

potential propagation along the median nerve with 7 mA (activation) and 2 mA (No activation). (C–D) Recruitment profiles showing selective activation ranges (HSR, MSR, LSR). Concentric electrodes achieved narrower selective recruitment, whereas square electrodes produced broader, less specific activation

In general, the electric field generated by the square electrodes covers a larger volume compared to the concentric electrode, providing a broader area of stimulation. In contrast, the concentric electrode demonstrates a higher concentration of the field in the upper layers, particularly in the skin and fat. This increased concentration results in a higher current density in these layers, which can cause greater discomfort for patients due to the intensified stimulation at the surface. This phenomenon is primarily attributed to the edge effect of the electrode, where the proximity of the anode and cathode in the concentric design amplifies the electric field at the surface. While the concentric electrode offers more focused stimulation, optimizing its geometry or adjusting operational parameters might be necessary to mitigate discomfort and improve patient tolerance during therapeutic applications. These parameters are evaluated in the next section.

5.1.2 Effect of Design Parameters of Concentric Electrodes

The current density distributions for the three concentric electrode sizes are shown in Fig. 5.5. As illustrated in Panel A, Size 1 produced the highest current density peaks, approaching 160 A/m², primarily concentrated along the electrode edges. This configuration also exhibited the largest non-uniformity coefficient (k), indicating a less homogeneous current distribution. In contrast, Size 2 markedly reduced both the peak current density and the k value, with maximum levels remaining below 100 A/m².

This improvement reflects a more uniform and evenly distributed electric field, attributable to the increased electrode surface area. A comparable trend was observed for Size 3, which further maintained low peak densities and enhanced field homogeneity.

On the other hand, Fig. 5.5.B shows the current density magnitude for Designs I-E1, I-E2, and I-E3, which represent different inter-electrode separations. In all cases, the current density at the inner electrode remains relatively stable. However, as the outer electrode becomes thinner—effectively increasing the inter-electrode distance while maintaining the same overall area—a noticeable rise in current density is observed at the edges of the outer electrode. This effect was inspected by varying parameters such as the area of the external ring, its thickness, and the inter-electrode distance, revealing that the increase in current density is primarily driven by the reduction in ring thickness. Although increasing the external ring thickness can help reduce this edge effect, it compromises the electrode's selectivity, as it is mentioned in the following paragraph.

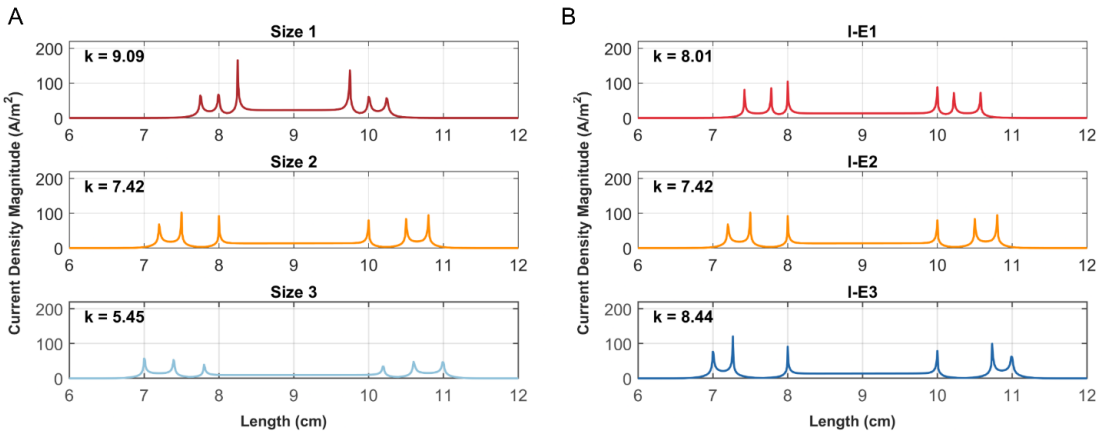

Fig. 5.5. Current density magnitude along a longitudinal line beneath the electrode surface. A) Comparison across electrode sizes (Size 1–3) and B) Comparison across inter-electrode distances

(I-E1 to I-E3). The non-uniformity of each configuration is quantified using the peak-to-average ratio k, with lower values indicating more homogeneous current distribution.

Complementing these results, the neural activation using the MRG model is shown on Fig. 5.6, the input current used was 5 mA for all designs. The smaller sized electrode showed greater selectivity, triggering the action potential only in the target nerve, as the size is increased adjacent nerves were also activated as is shown for Size 2 and Size 3. On the other side, a reduced inter-electrode distance effectively activates only the target nerve, while an increase in the inter-electrode distance reduced the selectivity.

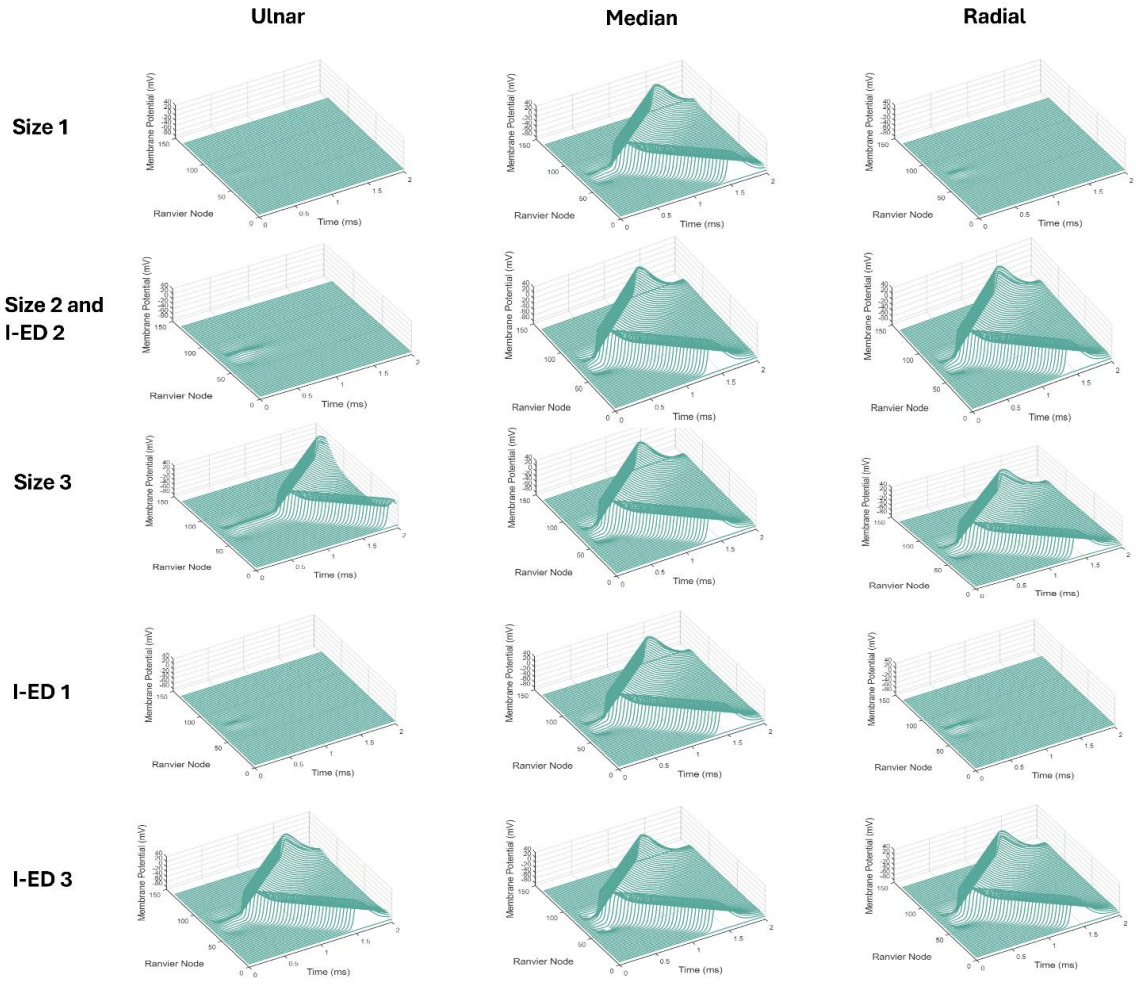

Fig. 5.6. Membrane potential distributions over time and along the Ranvier nodes representing axon activation in the ulnar, median, and radial nerves, corresponding to various concentric ring electrode designs with an input of 5 mA.

With the results extracted from these experiments, electrodes with smaller surface areas exhibited high selectivity by effectively targeting specific nerves, as described in previous works, yet this advantage was coupled with elevated peaks of current density, which could be traduced to an increase of discomfort.

The results demonstrated that optimizing medium-sized concentric electrodes by reducing the inter-electrode distance enhanced neural selectivity while simultaneously lowering peak current density. This configuration therefore shows potential for delivering more precise and efficient stimulation. Nevertheless, decreasing the anode–cathode separation also limits the penetration depth of the electric field, leading to predominantly superficial activation, as illustrated in Fig. 5.7. The implications of this trade-off depend on the specific application and patient characteristics. For instance, superficial stimulation may be advantageous when targeting forearm muscles located close to the skin surface, whereas reduced penetration could compromise effectiveness in deeper muscles or in individuals with larger forearm circumferences. These findings emphasize the importance of minimizing skin impedance to decrease the voltage demand on the stimulator, thereby enabling deeper neural activation when required.

As described in the literature review, this limitation could be addressed by incorporating medium-frequency stimulation to reduce tissue impedance. As shown in Fig. 5.8, the frequency sweep from 1–100 Hz (typical of FES)

to 1–10 kHz (typical of ICS) demonstrates a marked decrease in voltage requirements at higher frequencies, while the applied current remains constant. This reduction in tissue impedance facilitates deeper field penetration, decreases the voltage burden on the stimulator, and improves overall system efficiency.

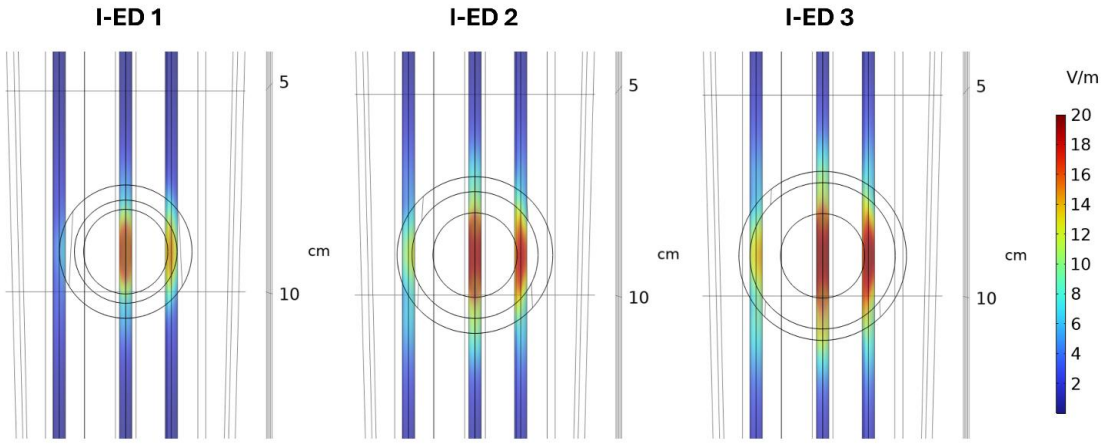

Fig. 5.7. Electric field (V/m) distribution in a cross-sectional plane parallel to the nerve pathways for three concentric electrode designs (I-ED 1, I-ED 2, and I-ED 3), each with varying inter-electrode distances. A constant input current of 5 mA was applied in all cases. The results show that increasing the inter-electrode distance enhances the depth of electric field penetration, as evidenced by the spread of higher voltage regions in I-ED 3 compared to I-ED 1.

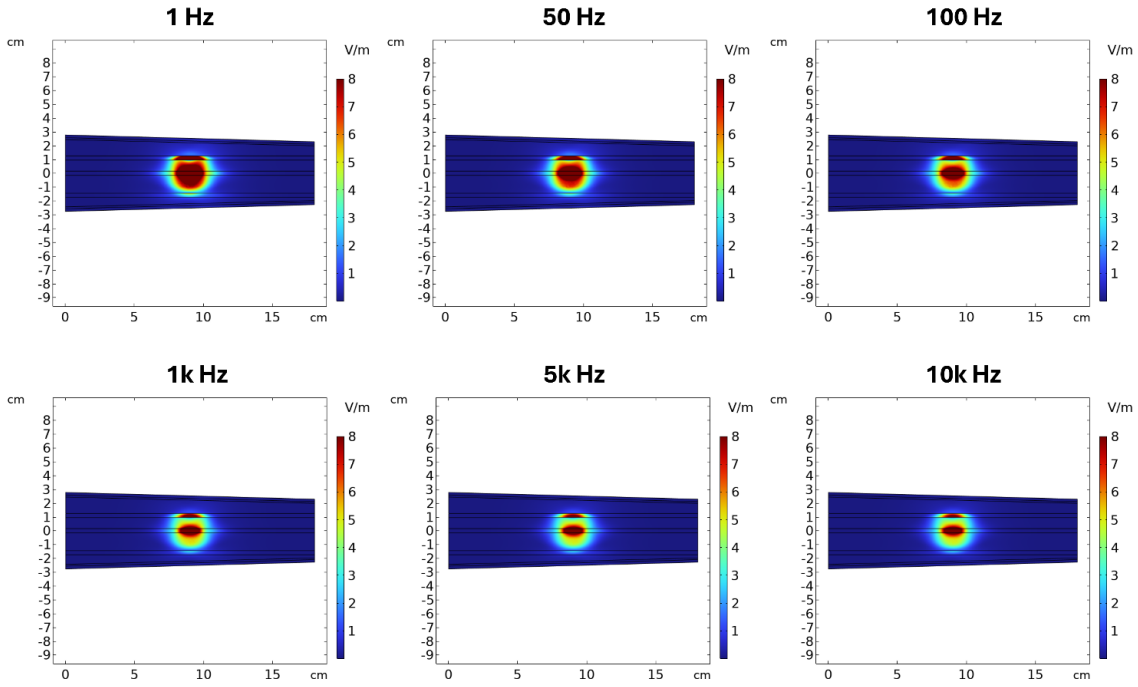

Fig. 5.8. Electric field (V/m) distribution for electrode Size 1 at varying stimulation frequencies: 1 Hz-100 Hz (typical range for FES), and 1k Hz- 10k Hz (typical range for ICS). All simulations were performed with a constant input current of 5 mA. The results demonstrate a decrease in electric field magnitude as frequency increases, due to the reduced impedance of biological tissues at higher frequencies.

5.1.3 Discussion

The results confirm that electrode geometry exerts a decisive influence on current distribution and neural recruitment in surface FES. Concentric electrodes consistently produced more spatially confined electric fields and activating functions compared to square geometries. These observations are consistent with theoretical predictions from quasi-static field models, in which the symmetric anode–cathode topology of concentric designs drives central field convergence and reduces lateral current dispersion. Such focality

enhances the ability to target specific neural structures within the densely innervated forearm.

However, the improved spatial confinement of concentric electrodes was accompanied by reduced penetration into deeper tissues, necessitating higher current amplitudes to activate target nerves. This limitation was evident in the MRG simulations, where the concentric configuration required 4.1 mA to elicit median nerve activation, compared to 2.5 mA for the square electrode. Despite this drawback, the concentric design provided a substantially broader high-selectivity range (HSR), allowing selective recruitment of the intended nerve while avoiding co-activation of adjacent nerves across a wider current window. This trade-off highlights the geometry's potential for applications requiring precise control of superficial motor units, while also underscoring the importance of addressing its depth constraints.

This study employed monophasic pulses for modelling, which differ from the biphasic waveforms commonly used in clinical FES. In monophasic stimulation, the outer ring serves as the anode and the central electrode as the cathode, resulting in a focused region of depolarisation beneath the centre and lower-magnitude hyperpolarisation under the return electrode (Fig. 5.2.B). During the cathodic phase of a biphasic pulse, the polarity reverses: the central electrode becomes the anode, and the surrounding ring acts as the cathode. In this case, hyperpolarisation beneath the central contact exceeds the surrounding depolarisation in magnitude, thereby reducing the net excitatory effect at the target site. As a result, higher stimulation currents are

required to achieve axonal activation. Once this threshold is exceeded, activation occurs in both phases.

Regarding stimulation comfort, previous studies have used the non-uniformity coefficient (k) as an indirect indicator of discomfort, associating higher k values with stronger edge effects or “hotspots.” However, no direct correlation between k and subjective pain perception (VAS) has yet been demonstrated. In this study, k was used as a mathematical proxy to estimate potential discomfort, complemented by analysis of current density distributions to guide the optimization of electrode geometry. The experimental validation of perceived discomfort across electrode configurations will be performed in the in-vivo phase using VAS scores.

The FEM simulations also highlighted the influence of medium-frequency stimulation on impedance and voltage requirements. As impedance decreases with increasing frequency, the stimulator can deliver the same current with a lower output voltage—an especially relevant factor for voltage-controlled stimulators. This reduction in impedance facilitates deeper current penetration into the tissue, enabling more efficient activation of muscular structures while minimizing surface discomfort.

The modelling strategy provides a comprehensive framework for evaluating different stimulation parameters and their physiological implications, enabling meaningful translation to in-vivo experiments. Moreover, developing anatomically specific FEM models for individual subjects could support a personalized approach, allowing stimulation parameters and electrode geometries to be tailored to each patient’s unique anatomy.

Altogether, the findings position electrode geometry as a modifiable and physiological control point in the design of surface FES systems. The concentric configuration presents a promising geometry to enhance selectivity in transcutaneous stimulation, particularly in the forearm and hand.

5.2. Prototyping Process

5.2.1 Fabrication

The fabrication workflow for the custom electrodes consisted of two main stages: 3D printing of the flexible substrate and manual assembly of the conductive and interface layers. The stages of the prototyped electrode and the result of the assembled electrode are shown on Fig. 5.9. 3D printing process of the resin substrate took 7 hours and 7 minutes for a batch of 8 electrodes using the Formlabs Form 3.

Following printing, the electrodes underwent a post-curing process under UV light at 60 °C for 1 hour using the Form Cure system to ensure optimal mechanical and material properties. The subsequent assembly process—including application of the Ag/AgCl conductive paint and hydrogel layer—took approximately 1 hour per batch, yielding an average fabrication time of roughly 1 hour and 15 minutes per electrode. This efficient turnaround allows for rapid prototyping and design iteration, with new electrode geometries ready for testing within 24 hours.

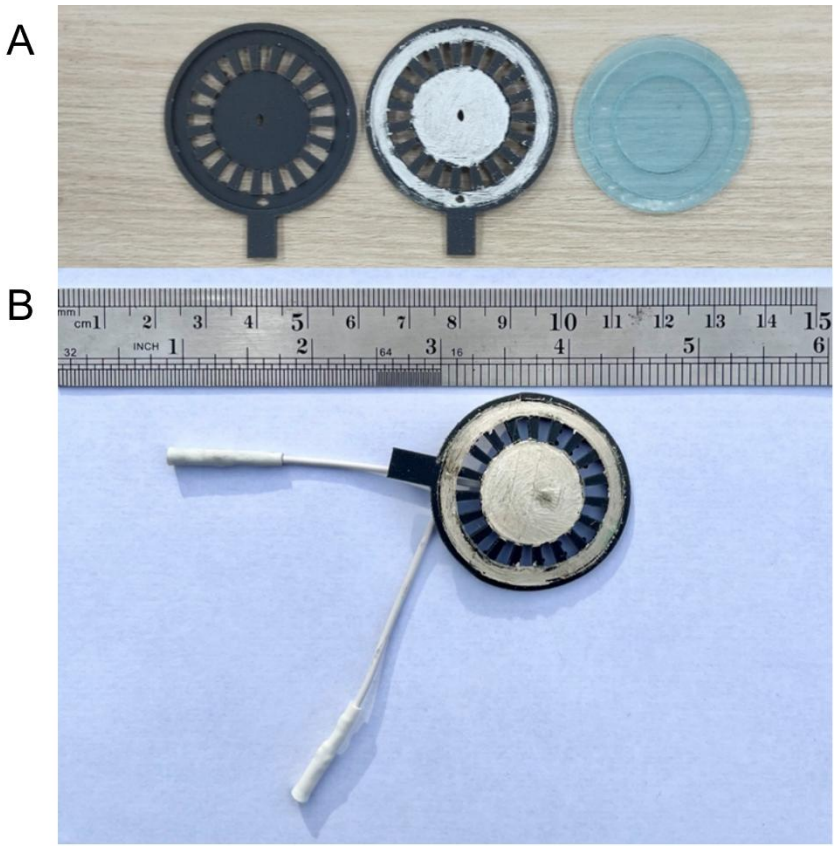

Fig. 5.9. A) Stages of the fabrication process of the electrodes. Flexible resin substrate, substrate filled with conductive Ag/AgCl paint and hydrogel layer. B) Frontal view of the 3D-printed electrode with a measurement reference.

Functionally, the fabricated electrodes were able to deliver current pulses reliably and maintain stable adhesion to the skin for approximately 30 minutes. It is anticipated that the use of higher-grade hydrogel materials could improve long-term adhesion and optimize the electrical interface by reducing impedance and enhancing stimulus transmission. However, it was noted that the electrode connectors were somewhat sensitive to movement and must be handled with care to avoid signal interruption. No skin irritation or damage was reported using the electrodes.

From a cost perspective (described in Table 5.1), the initial investment in equipment includes the Formlabs Form 3+ printer (approx. $2,500 USD) and the Form Cure UV curing unit (approx. $750 USD), totaling $3,250 USD. These devices are commonly available in academic and research environments, which facilitates the implementation of the fabrication process without requiring significant additional investment.

Table 5.1. Estimated material costs for 3D-printed electrodes.

Material	Unit Cost	Quantity per Batch	Cost per Batch (USD)
Flexible resin (FLFLGR02)	$199/L	20 mL	$3.98
117-23 Ag/AgCl	$5/g	1.42 g	$7.10
Hydrogel	$0.02/cm^2	100.5 cm^2	$2.01
Total cost per batch			$13.09
Estimated cost per electrode			$1.64

The materials used for electrode production include Formlabs flexible resin (FLFLGR02), with an approximate cost of $199 USD per liter. Each electrode consumes about 2.5 mL of resin (obtained from Formlabs Software), meaning that 100 electrodes can be produced from 250 mL of material. The Ag/AgCl conductive paint, used to define the active layer, costs $500 USD per 100 grams. Based on estimated usage, 50 grams of paint is sufficient to fabricate approximately 350 electrodes. Additionally, an Axelgaard AG735 hydrogel disc is used as the skin-contact interface, priced

at $0.3 USD per unit. The unit cost per electrode—including resin, conductive paint, and hydrogel—is approximately $1.64 USD.

Beyond the functional validation of the prototyped electrodes, the fabrication strategy itself represents a significant methodological advancement for rapid testing of geometry-specific designs in FES. The simplified pipeline described in this work overcomes critical barriers identified in the literature, such as complex and multi-step workflows, reliance on proprietary materials, and the need for specialized personnel. By minimizing infrastructure and material constraints, this approach enables same-day simulation and next-day prototyping, thereby facilitating a closed-loop workflow between modeling, fabrication, and experimental validation. This capability is especially valuable for academic and clinical research settings where agility and adaptability are essential. In contrast to PCB-based alternatives, which often lack flexibility or biocompatibility, the resin-based custom electrodes offer a practical balance between skin conformity, electrical performance, and design versatility. Furthermore, their integration into hypothesis-driven design-evaluation cycles allows for targeted exploration of anatomical regions, paving the way for patient-specific neurostimulation strategies. However, future efforts should focus on reducing inter-sample variability during the conductive layer deposition and improving connector robustness, as these factors currently constrain mechanical reliability and electrical repeatability during testing.

While the proposed prototyping method reduces fabrication barriers and accelerates design iteration, it also introduces limitations. Among them is the increased variability stemming from manual fabrication steps—

particularly during conductive layer deposition and hydrogel placement. This variability can compromise the mechanical robustness and electrical uniformity of the electrodes, especially under repeated or dynamic use. Rather than achieving cost reduction purely through lower material expenses, this approach prioritizes speed and adaptability, making it especially advantageous for evaluating novel or anatomically complex electrode geometries. Such flexibility enables tight feedback loops between simulation and empirical testing, a critical asset in exploratory FES research. However, these benefits come at the expense of standardization. Variability across batches may introduce confounding factors in comparative studies or clinical scaling. To mitigate this, future work should investigate targeted semi-automation strategies—such as precision stenciling or modular paint cartridges—to reduce inter-sample deviation while preserving the prototyping agility that underpins this framework.

5.2.2 Impedance Measurement

The frequency-dependent impedance characteristics of the skin–electrode interface were evaluated for three electrode configurations: the custom-fabricated concentric electrode, a custom square electrode, and a commercial square electrode (Axelgaard UltraStim X). All measurements were conducted under identical conditions, including standardized skin preparation and consistent placement on the anterior forearm, to ensure comparability.

As illustrated in Fig. 5.10, all electrode types exhibited the expected inverse relationship between impedance and frequency, characteristic of the

capacitive nature of the electrode–tissue interface. In the low-frequency range (10–100 Hz), impedance values were notably higher. The concentric and square prototyped electrodes presented initial impedance values exceeding 450 kΩ, whereas the commercial square electrode demonstrated a lower starting impedance of approximately 300 kΩ.

As the frequency increased across the 10 Hz to 100 kHz range, impedance values for all electrode types decreased exponentially, approaching similar values. Notably, beyond 1 kHz, the differences among electrode configurations diminished significantly, with all curves converging to impedance values below 10 kΩ at higher frequencies. This convergence suggests reduced influence of geometric and material differences at stimulation frequencies commonly associated with interferential currents, and highlights the relevance of impedance evaluation in the low-frequency regime where most transcutaneous stimulation protocols operate.

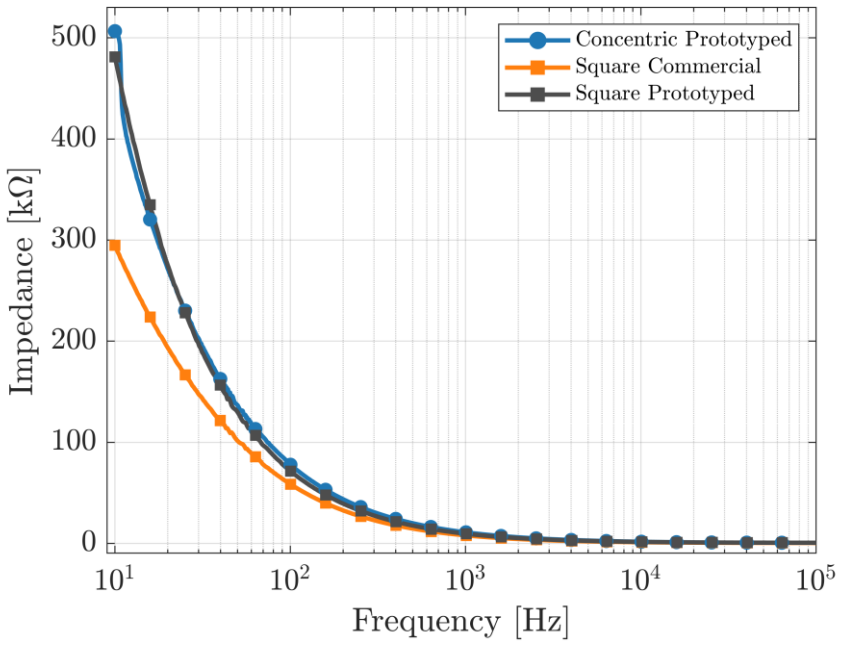

Fig. 5.10. Impedance vs. frequency for concentric, square prototyped, and commercial electrodes. All configurations show decreasing impedance with frequency, with greater differences observed below 1 kHz.

5.2.3 Discussion

The importance of electrode geometry in enhancing stimulation focality and therapeutic efficacy in FES was assessed. However, translating novel designs into practical, testable prototypes remains hindered. Conventional fabrication methods—such as stereolithography, screen printing, and inkjet deposition—often involve complex, multi-step procedures, reliance on proprietary materials, and stringent quality control requirements [96], [97], [98]. These constraints increase dependence on specialized equipment and technical expertise, and limit the feasibility of rapid iteration in typical academic or clinical research settings [98].

Limitations of the current method include manual variability in conductive layer application, hydrogel adhesion, and connector integrity. These issues highlight the need for improved standardization or semi-automated manufacturing in future iterations. Nonetheless, the model provides sufficient physiological fidelity for comparative analysis and iterative design. In this way, the proposed methodology offers a reproducible, and accessible platform for the systematic exploration of surface electrode configurations in FES.

5.3. In-vivo Testing

In-vivo testing was conducted to validate the modeling and prototyping results under physiological conditions. This stage provided the first link between computational predictions and actual motor responses, allowing assessment of how electrode geometry and stimulation strategies translate into functional movements and user comfort.

5.3.1 Biphasic Stimulation with Concentric Electrodes

The biphasic-stimulation results obtained with the concentric and square electrodes are described as follows. For these tests, the medium-sized concentric electrode (I-E2) was used together with a square electrode of equivalent surface area. This geometry was selected because it provided consistent selectivity and showed good adaptability across different anatomical variations.

Fig. 5.11 shows representative metacarpophalangeal (MCP) joint-angle trajectories for both electrode configurations. Both geometries successfully induced visible digit flexion, but distinct differences emerged in

the spatial distribution and selectivity of the evoked responses. With the square electrode, stimulation elicited synchronous flexion of all digits, with comparable amplitudes in the pinky, ring, and middle fingers. In contrast, the concentric electrode produced pronounced flexion of the ring finger, reduced flexion of the little finger, and negligible responses in the middle and index fingers. This qualitative pattern was consistent across subjects, but some inter-subject variability was observed. Selective activation was also achieved with square electrodes in two participants, and co-activation of the middle finger occurred in some instances with concentric stimulation. These results suggest that anatomical variability plays a non-negligible role in modulating stimulation outcomes, even under standardized electrode placement.

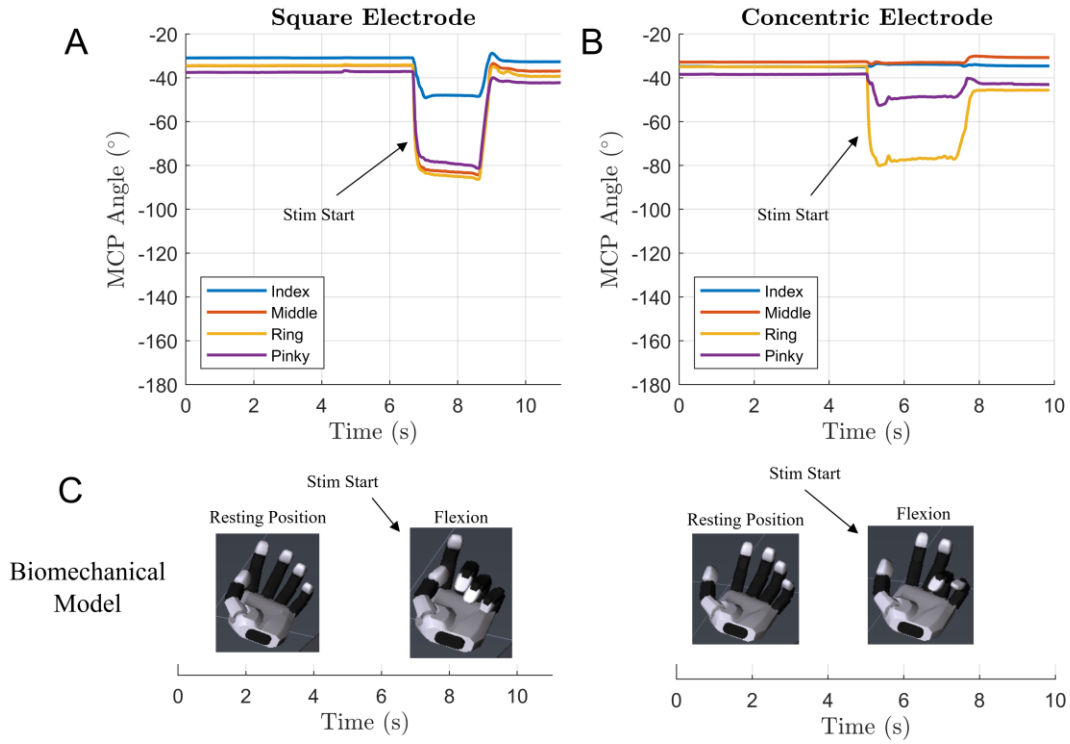

Fig. 5.11. Representative example of metacarpophalangeal (MCP) joint trajectories during digit flexion with square and concentric electrodes. (A) Square electrode stimulation induced simultaneous flexion of all four fingers, with similar amplitudes across them. (B) Concentric electrode

stimulation produced a more selective response, with pronounced flexion of the ring finger, partial activation of the pinky, and minimal movement in the index and middle fingers. (C) Biomechanical hand model illustrating the corresponding flexion response, showing the transition from resting position to flexion after stimulation onset.

To quantify motor selectivity, the ROM was calculated for each finger and averaged across participants. The pattern observed in the previous figure is supported by the mean ROM values shown in Fig. 5.12 for finger flexion and thumb abduction. Details are described in Table 5.2. For finger flexion, concentric electrodes produced a more differentiated ROM profile across digits, with reduced unintended activation of the index and middle fingers and preserved or enhanced flexion of the ring and little fingers. A similar trend was observed during thumb abduction, where concentric electrodes limited co-activation of non-targeted fingers. However, in this case, the ROM generated with concentric electrodes was lower than that achieved with square electrodes. This effect arises because the focalized field of concentric electrodes is less able to maintain activation when the motor point shifts during thumb movement, whereas the broader field of square electrodes can follow this displacement. This limitation, observed by some participants, underscores the need for further development of concentric geometries capable of adapting to motor point displacement, such as multi-concentric electrodes or concentric arrays.

Another effect observed was that, despite consistent electrode placement across participants, square electrodes sometimes activated the middle and ring fingers simultaneously. This unintended co-activation could be mitigated by tailoring the design of concentric electrodes to better match individual anatomical characteristics.

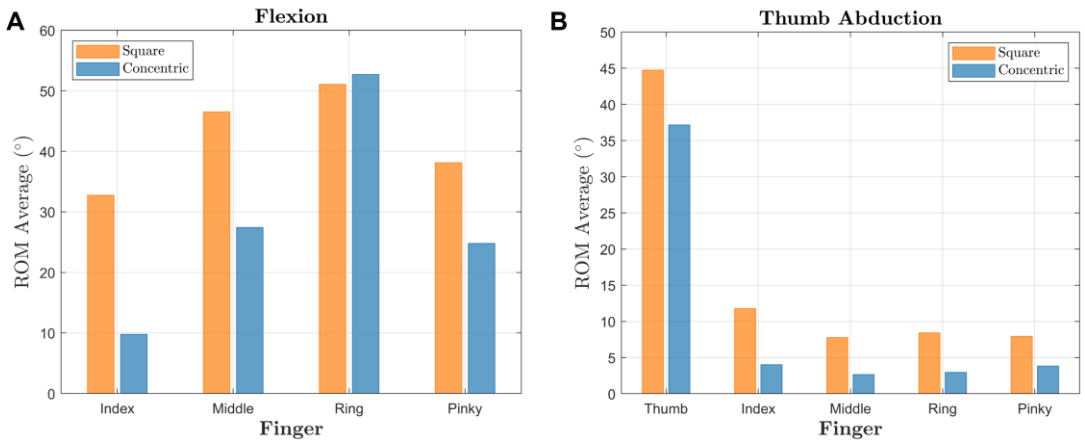

Fig. 5.12. Average range of motion (ROM) during (A) finger flexion and (B) thumb abduction with square and concentric electrodes. Square electrodes induced broader activation across digits, while concentric electrodes showed greater selectivity, reducing unintended movements in non-targeted fingers.

Table 5.2. Average ± SD ROM (°) of fingers with square and concentric electrode for finger flexion and thumb abduction.

Movement	Finger	Square	Concentric
Finger Flexion	Index	32.74 ± 20.49	9.78 ± 8.64
	Middle	46.53 ± 20.43	27.43 ± 23.63
	Ring	51.06 ± 17.73	52.69 ± 13.93
	Pinky	38.12 ± 16.61	24.78 ± 15.93
Thumb Abduction	Index	11.77 ± 11.94	4.02 ± 3.49
	Middle	7.77 ± 8.84	2.66 ± 4.24
	Ring	8.43 ± 8.48	2.96 ± 2.64
	Pinky	7.94 ± 8.13	3.83 ± 2.42
	Thumb	44.74 ± 11.59	37.16 ± 8.55

Measurements from the selectivity index highlighted the significance of the selectivity of movements. For the flexion of fingers, the selectivity index of concentric electrode (0.723 ± 0.175) compared to square electrodes

(0.546 ± 0.098), as detailed in Table 5.3. Given the non-normal distribution of scores in the square condition (Shapiro–Wilk test, $p = 0.001$), a Wilcoxon signed-rank test was used, confirming a statistically significant improvement with the concentric geometry ($p < 0.01$). For the thumb abduction, the concentric electrode had a selectivity index of 0.759 ± 0.120 and the square electrode 0.626 ± 0.19. Given the non-normal distribution of the data a Wilcoxon signed-rank test was applied confirming a $p<0.05$. Particularly this movement was more selective than the flexion of finger because it was directly applied to the muscle abductor pollicis. However, the square electrode produces higher untargeted activations.

Table 5.3. Mean ± SD values of Selectivity index and VAS per geometry.

Movement	Geometry	Selectivity Index	VAS
Finger Flexion	Square	0.546 ± 0.098	2.18 ± 1.54
	Concentric	0.723 ± 0.175	2.91 ± 2.17
Thumb Abduction	Square	0.626 ± 0.19	2.67 ± 1.37
	Concentric	0.759 ± 0.120	2.58 ± 1.56

Participant discomfort was evaluated using a 10-point VAS as shown on Fig. 5.13. Average scores were slightly higher with concentric electrodes (2.91 ± 2.17) compared to square electrodes (2.18 ± 1.54), but the difference was not statistically significant (paired t-test, $p > 0.01$). Average stimulation current was 5.75 mA (flexion with square), 9.36 mA (flexion with concentric), 6.17 mA (thumb abduction with square) and 6.25 mA (thumb abduction with concentric). No relation between discomfort and increase of current was found across patients.

Mild adverse effects were observed in some participants, including transient erythema, occurring in four cases with concentric electrodes and in two cases with square electrodes during the 30-minute stimulation period. Notably, erythema with the concentric electrodes appeared first around the external ring, consistent with the mathematical modeling results that showed elevated current density at the electrode edges.

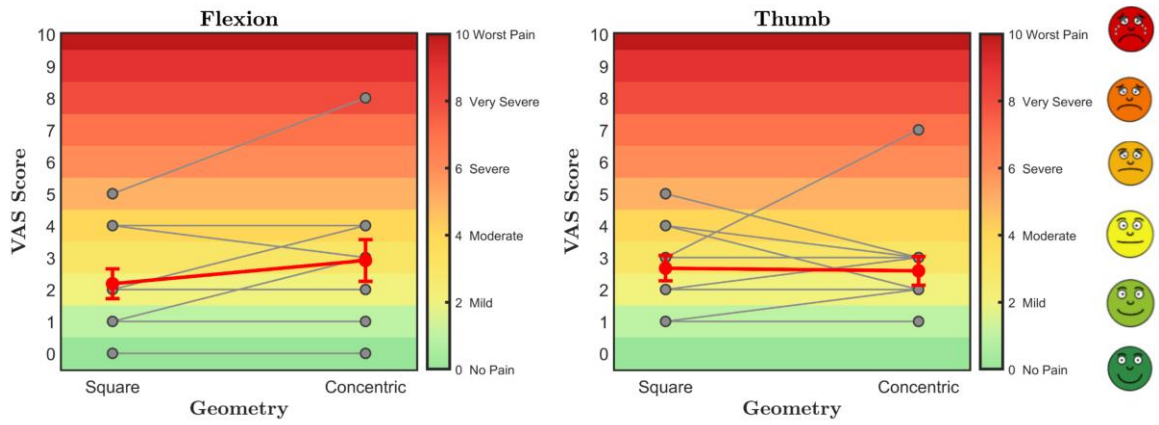

Fig. 5.13. Visual Analog Scale (VAS) scores for perceived discomfort during (left) finger flexion and (right) thumb abduction with square and concentric electrodes. For flexion, concentric electrodes showed slightly higher average VAS scores than square electrodes, though both remained within the mild-to-moderate range. For thumb abduction, mean VAS scores were similar between electrode types, with most participants reporting mild discomfort, no statistical significance was found.

5.3.2 Interferential Current Stimulation with Concentric Electrodes

ICS was evaluated to compare its performance against conventional biphasic stimulation using concentric electrodes. A key finding was that the current required to elicit visible finger movement was consistently lower with ICS than with biphasic stimulation. This reduction is explained by the decreased tissue impedance at medium frequencies, which facilitates current penetration and lowers the activation threshold. Despite these differences in

current demand, the overall selectivity and distribution of range of motion (ROM) across the fingers remained similar between the two stimulation modes, reflecting the effect of electrode geometry. However, because ICS achieved activation at lower current thresholds of the stimulator, participants exhibited greater ROM compared to biphasic stimulation. This effect is illustrated in Fig. 5.14, where panel A shows the threshold current required to elicit movement, and panel C depicts the average range of motion achieved for each finger.

Consistent with these results, a greater number of participants exhibited finger activation with ICS compared to concentric biphasic stimulation. For instance, at the same motor point used in the previous measurement (zone 2), activation was observed in 8 participants with ICS, whereas only 5 participants responded to concentric biphasic stimulation. It should be noted, however, that the total number of participants showing activation was lower than in earlier trials, due to limitations of the stimulator employed in this experiment, which restricted the maximum output voltage that could be delivered. An outlier was observed in zone 4 with concentric biphasic stimulation. While activation in all zones generally required lower current with ICS, only one participant exhibited activation in zone 4 using a concentric electrode at 18 mA. When averaged with the other participant who responded in this zone, the mean threshold appeared lower (24.0 mA). However, this was an isolated case and should not be interpreted as a consistent effect.

Regarding the forearm zone mapping with ICS (Fig. 5.14 A and B), distinct activation patterns were observed. Zone 1 primarily elicited flexion

of the ring finger, zone 2 activated both the ring and middle fingers, and zone 3 predominantly targeted the middle finger. In contrast, zone 4 showed inconsistent responses, with only a small number of participants exhibiting activation (2 and 3 for each stimulation method). These findings suggest that, with the present concentric geometry, stimulation is most effective for recruiting the ring and middle fingers. Further research using alternative electrode geometries will be necessary to identify isolated motor points for the index and pinky fingers.

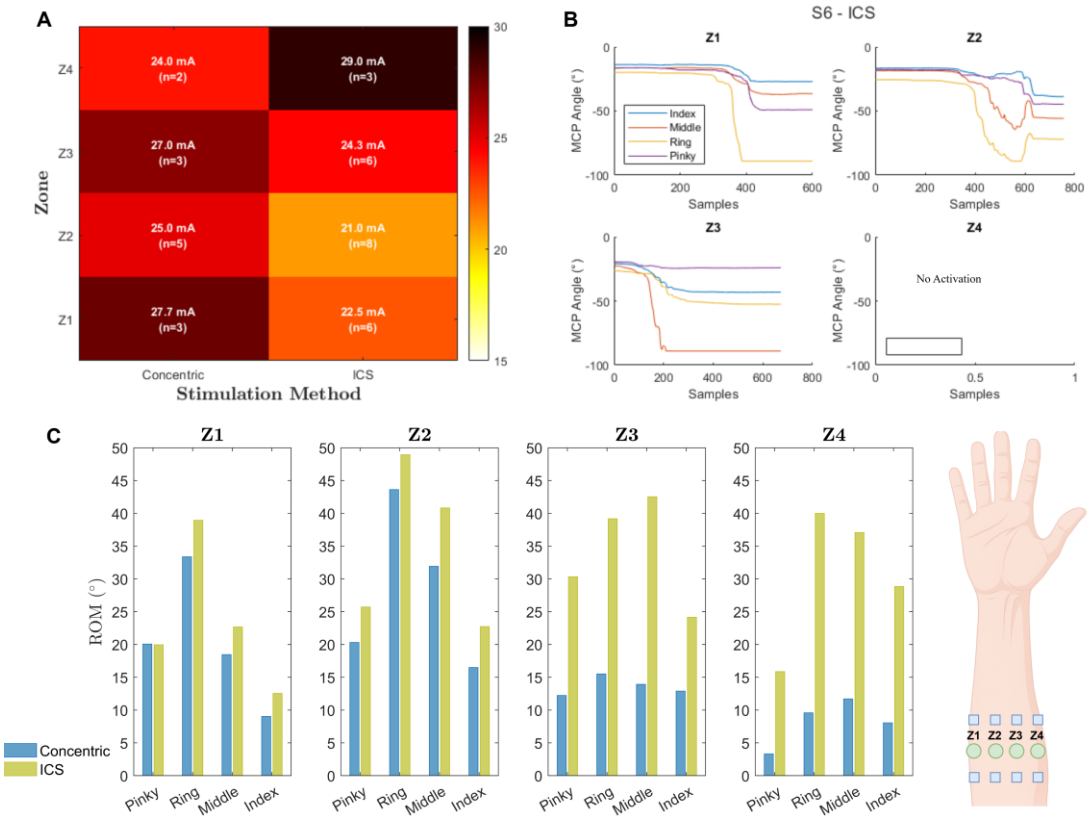

Fig. 5.14. ICS and concentric electrode results across forearm zones. (A) Threshold currents required to elicit activation and the number of participants responding in each zone for both stimulation methods. (B) Example of finger movements generated with ICS across zones Z1–Z4; no activation was observed in Z4 for this participant. (C) Average range of motion (ROM) for each finger

across zones and stimulation methods, showing generally higher ROM with ICS compared to concentric biphasic stimulation.

Table 5.4. Stimulation current threshold (mean ± SD, mA) for each zone and number of participants that elicit an activation for each type of stimulation.

Zone	Concentric	ICS	N_Concentric, N_ICS
Z1	27.67 ± 4.93	22.50 ± 6.66	(3, 6)
Z2	25.00 ± 7.52	21.00 ± 6.76	(5, 8)
Z3	27.00 ± 5.20	24.33 ± 5.57	(3, 6)
Z4	24.00 ± 8.49	29.00 ± 1.73	(2, 3)

Participant discomfort during stimulation was assessed using a 10-point VAS. As shown in Fig. 5.15, ICS resulted in significantly lower pain scores compared to concentric biphasic stimulation ($p < 0.05$, paired t-test). The average VAS score decreased from 3.75 ± 1.98 with concentric biphasic stimulation to 2.12 ± 1.73 with ICS, corresponding to a shift from moderate toward mild discomfort. These findings confirm that ICS not only reduces the activation threshold but also enhances user comfort during stimulation.

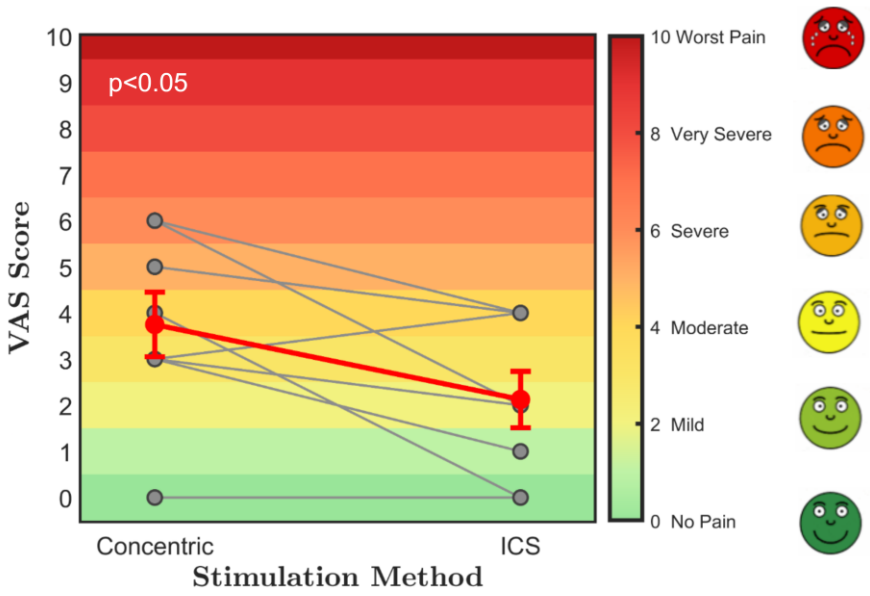

Fig. 5.15. VAS scores comparing discomfort during concentric biphasic stimulation and ICS. Average VAS scores were significantly lower with ICS (2.12 ± 1.73) compared to concentric biphasic stimulation (3.75 ± 1.98), indicating improved comfort with ICS (paired t-test, $p < 0.05$).

Since discomfort was reduced with ICS, future work could focus on refining electrode design to further improve selectivity. The use of smaller concentric electrodes or variations in the thickness of the outer ring may enhance the activation of additional fingers by better matching the stimulation field to specific motor points. Importantly, the in-silico evaluation indicated that these geometries, when used with conventional biphasic stimulation, would likely increase discomfort due to higher current densities. By employing ICS, however, this limitation can be mitigated, as medium-frequency stimulation effectively controls surface discomfort while maintaining selectivity.

Complementing this, a comprehensive mapping of forearm motor points with concentric electrodes would provide valuable insight into the optimal geometries for targeting individual muscles.

5.3.3 Discussion

The in-vivo results highlight the critical role of electrode geometry in modulating motor selectivity during surface FES. In the context of upper-limb rehabilitation, precise activation of individual muscles is essential for achieving functional movements such as grasping, releasing, or performing precision pinches [32], [35], [40]. Concentric electrodes achieved more focal activation of the ring finger with reduced unintended movement of adjacent digits, as reflected by a 32% increase in the Selectivity Index (0.723 ± 0.175 vs. 0.546 ± 0.098). This spatial precision is of direct clinical relevance, offering a non-invasive approach to selectively activate individual muscles.

Participant feedback highlighted a strong dependence of sensory perception on electrode alignment with the motor point. When concentric electrodes were misaligned, participants reported localised discomfort without visible muscle contraction. In contrast, accurate placement consistently produced effective muscle activation with minimal or no discomfort. These observations highlight the critical role of motor point location in realising the full selectivity potential of concentric configurations—particularly in applications requiring fine-grained control, such as independent digit activation in upper-limb neuroprosthetics.

Despite overall improvements in selectivity, considerable inter-subject variability was observed, as indicated by the standard deviation of the

Selectivity Index (SD = 0.175). This variation is likely attributable to individual differences in forearm anatomy and motor point location. In certain cases, square electrodes produced partially selective activation, while in others, concentric stimulation resulted in unintended co-activation of adjacent digits. This observation is consistent with differences among concentric electrode designs. Preliminary tests with the smaller inter-electrode distance (I-ED1) showed high selectivity but failed to elicit activation in some participants, likely due to its limited penetration depth and the larger circumference of the proximal forearm of some subjects. To ensure uniform testing across all subjects, the medium-sized I-ED2 electrode was therefore selected for all measurements.

These findings reinforce the importance of subject-specific optimization of electrode geometry and placement to account for anatomical variability and enhance stimulation precision [99]. This personalization can be achieved through iterative refinement of electrode geometry and placement within the modelling-to-prototyping workflow.

ICS demonstrated a clear reduction in activation current, attributable to the lower tissue impedance at medium frequencies. The resulting selectivity were comparable to those obtained with biphasic stimulation, as electrode geometry remained the primary factor determining selectivity. Importantly, ICS also reduced discomfort levels, likely due to the analgesic effect of medium-frequency stimulation on the skin surface.

The challenge of achieving transcutaneous focality has traditionally been addressed using high-density or matrix-based electrode arrays that enable localized current steering. However, these systems often require

complex hardware and control algorithms, limiting their practicality in clinical or resource-constrained environments. The approach proposed in this thesis offers a simpler and more accessible alternative: by modifying the electrode geometry and integrating ICS, it is possible to obtain comparable improvements in selectivity and hand dexterity without increasing system complexity. Implementation could follow the same principles as traditional surface stimulation setups, requiring only the substitution of standard electrodes with concentric designs. In the simplest form, this adaptation could even be achieved by physically cutting or shaping existing electrodes into a concentric configuration. Future developments are expected to focus on the commercial production of concentric geometries optimized for clinical and rehabilitation applications, enabling broader adoption of this technique.

In the other side, a feasible approach would involve a compact, multi-channel stimulator capable of delivering medium-frequency currents through concentric electrodes placed over key motor points. By coordinating their activation through simple control algorithms, it would be possible to reproduce functional hand movements like grasping, releasing, or finger flexion. Moreover, combining different electrode types could enhance the versatility of such a system: for instance, square electrodes could be used for global grasping movements, while concentric electrodes with ICS could target specific finger flexions or fine motor adjustments, both operating under the same stimulation configuration. Compared to transcutaneous matrix-array systems, this approach represents a simpler and more accessible method to achieve hand dexterity, requiring fewer stimulation channels and less complex control hardware. However, a comprehensive motor-point mapping

of the forearm remains essential to fully exploit the potential of this hybrid stimulation strategy and to enable reliable, patient-specific electrode placement.

Chapter 6. Conclusion

This thesis evaluated the biophysical and neurophysiological effects of surface electrical stimulation of the forearm using custom concentric electrodes and interferential currents to improve finger movement selectivity and stimulation comfort. The research integrated computational modeling, rapid prototyping, and in-vivo testing to systematically assess the proposed approach, successfully meeting the defined objectives.

FEM and axon modeling indicated that concentric electrodes generate a more localized electric field and higher focality index than traditional square electrodes. This configuration achieved more confined and selective neural activation. These findings confirm that electrode geometry critically determines stimulation selectivity and position geometry as a modifiable parameter to advance non-invasive FES systems. However, the elevated surface current density observed at low frequencies suggests potential discomfort, emphasizing the importance of optimizing inter-electrode spacing and stimulation parameters. Such parameters should be individually adjusted for each patient to balance selectivity, comfort, and therapeutic effectiveness.

The prototyping process, implemented through a simplified 3D-printing-based workflow, proved effective for rapidly fabricating biocompatible and flexible electrodes. The fabrication strategy allowed for rapid iteration between modeling and experimental testing, reducing dependency on industrial manufacturing and demonstrating feasibility for research and small-scale clinical applications.

During the in-vivo evaluation, concentric electrodes achieved significantly higher selectivity indices for both finger flexion and thumb abduction compared to square electrodes This confirms the improved control of motor recruitment. Furthermore, the use of ICS reduced the current required to elicit muscle activation and improved comfort compared to biphasic stimulation. These findings show that combining concentric geometry with ICS enhances both selectivity and comfort without increasing system complexity. Further research is required to translate these results into task-oriented FES applications for functional rehabilitation, as well as pilot studies in stroke patients to assess the feasibility of these techniques in clinical FES therapies.

Overall, this thesis demonstrates that optimizing surface electrode geometry and stimulation waveform parameters can bridge the gap between complex neuroprosthetic systems and the accessibility of traditional FES. The combined use of concentric electrodes and interferential currents proved effective in improving selectivity and comfort, validating the initial hypothesis.

Chapter 7. Appendix

7.1. Biphasic Stimulation with Concentric Electrodes

Table 7.1. Subjects ROM (°) per finger and selectivity index during stimulation with square biphasic stimulation for finger flexion.

Subject	Index	Middle	Ring	Pinky	Selectivity Index
s1	43.46	79.89	79.30	75.53	0.5566
s2	57.66	30.30	57.38	34.94	0.5121
s3	36.96	34.67	35.02	35.9	0.4975
s4	34.72	61.83	60.24	33.95	0.4938
s5	12.46	38.09	27.62	18.70	0.4781
s6	49.54	63.90	59.39	49.86	0.4906
s7	7.66	42.91	29.57	26.14	0.5193
s8	60.01	38.02	71.65	55.13	0.5640
s9	13.92	35.62	44.60	30.77	0.6034
s10	3.54	5.71	27.92	18.13	0.8328
s11	52.21	68.02	64.44	49.19	0.4838
s12	19.73	58.43	55.61	29.17	0.5203

Table 7.2. Subjects ROM (°) per finger and selectivity index during stimulation with concentric biphasic stimulation for finger flexion.

Subject	Index	Middle	Ring	Pinky	Selectivity Index
s1	9.40	9.11	54.30	59.87	0.8605
s2	3.49	2.52	40.31	14.17	0.9007
s3	2.32	0.69	40.99	28.88	0.9587
s4	29.21	72.10	65.91	37.16	0.5043
s5	-	-	-	-	-
s6	14.23	44.73	59.43	31.50	0.6066
s7	3.62	16.19	55.01	8.96	0.7636
s8	10.09	34.47	42.13	11.95	0.5483
s9	6.46	36.67	49.96	32.45	0.6564

s10	0.3	1.57	34.54	7.55	0.9574
s11	20.35	30.1	83.87	29.44	0.6919
s12	8.07	53.56	53.22	10.66	0.590

Table 7.3. Subjects ROM (°) per finger and selectivity index during stimulation with square biphasic stimulation for thumb abduction.

Subject	Index	Middle	Ring	Pinky	Thumb	Selectivity Index
s1	8.00	9.87	6.34	5.97	52.47	0.6348
s2	13.48	6.52	20.29	9.81	49.89	0.4989
s3	44.16	27.46	24.52	23.00	50.49	0.2977
s4	2.25	0.94	2.89	2.82	32.14	0.7831
s5	20.81	24.11	20.66	25.96	64.23	0.4132
s6	14.69	4.19	6.96	6.42	20.80	0.3921
s7	2.74	1.95	0.60	3.18	41.83	0.8316
s8	16.64	5.36	7.18	5.72	48.61	0.5820
s9	5.02	6.46	6.62	6.75	50.47	0.6701
s10	3.73	3.63	1.51	1.38	32.23	0.7586
s11	2.48	1.59	0.72	2.05	43.33	0.8636
s12	7.25	1.20	2.91	2.26	50.38	0.7872

Table 7.4. Subjects ROM (°) per finger and selectivity index during stimulation with concentric biphasic stimulation for thumb abduction.

Subject	Index	Middle	Ring	Pinky	Thumb	Selectivity Index
s1	4.20	1.73	4.27	5.26	51.31	0.7686
s2	2.85	0.50	2.32	4.27	27.35	0.7332
s3	6.90	2.73	1.52	3.86	37.60	0.7146
s4	3.10	0.08	1.63	1.57	40.41	0.8637
s5	2.97	1.76	2.50	3.16	33.29	0.7621
s6	1.25	0.73	0.83	2.97	21.54	0.7886
s7	1.03	1.15	1.66	1.46	33.44	0.8623
s8	13.94	14.3	8.73	10.66	39.39	0.4226
s9	3.19	7.85	7.55	3.46	38.06	0.6331
s10	1.86	0.04	0.93	2.02	34.10	0.8756

s11	2.58	0.68	0.61	3.70	37.83	0.8332
s12	4.34	0.36	2.97	3.58	51.58	0.8208

7.2. Interferential Current Stimulation with Concentric Electrodes

Table 7.5. Subjects ROM (°) per finger during biphasic stimulation with concentric electrodes in Z1.

Subject	Index	Middle	Ring	Pinky	Current (mA)
s1	9.86	29.33	57.27	35.41	31
s2	6.64	7.49	8.56	2.62	30
s9	10.60	18.59	34.28	22.14	22

Table 7.6. Subjects ROM (°) per finger during biphasic stimulation with concentric electrodes in Z2.

Subject	Index	Middle	Ring	Pinky	Current (mA)
s2	50.58	90.51	85.95	58.97	29
s3	13.27	18.26	18.57	6.09	29
s6	5.93	12.35	31.30	1.94	30
s9	9.62	33.33	49.35	29.81	12
s12	3.02	5.22	32.92	4.79	25

Table 7.7. Subjects ROM (°) per finger during biphasic stimulation with concentric electrodes in Z3.

Subject	Index	Middle	Ring	Pinky	Current (mA)

s1	14.49	21.43	30.29	28.95	21
s2	3.24	3.33	2.24	1.05	30
s3	20.96	17.00	13.97	6.71	30

Table 7.8. Subjects ROM (°) per finger during biphasic stimulation with concentric electrodes in Z4.

Subject	Index	Middle	Ring	Pinky	Current (mA)
s1	3.68	12.71	8.02	5.05	18
s3	12.45	10.71	11.13	1.58	30

Table 7.9. Subjects ROM (°) per finger during ICS with concentric electrodes in Z1.

Subject	Index	Middle	Ring	Pinky	Current (mA)
s1	12.96	24.05	67.16	27.34	25
s2	33.1	62.43	63.46	45.36	25
s4	2.01	1.57	1.14	3.17	30
s6	13.43	20.99	69.20	33.10	19
s8	5.13	21.14	15.30	4.01	30
s9	14.52	26.40	35.27	22.45	11
s12	6.72	2.16	21.03	4.33	25

Table 7.10. Subjects ROM (°) per finger during ICS with concentric electrodes in Z2.

Subject	Index	Middle	Ring	Pinky	Current (mA)
s1	14.64	34.64	60.36	36.89	19

s2	49.06	88.16	101.01	59.75	19
s3	19.22	17.23	18.12	14.64	23
s4	25.19	65.65	63.19	39.86	30
s6	22.28	46.02	63.50	27.03	13
s8	18.63	47.85	17.93	9.35	30
s9	17.43	21.28	23.43	8.25	12
s12	15.4	5.76	44.00	10.00	22

Table 7.11. Subjects ROM (°) per finger during ICS with concentric electrodes in Z3.

Subject	Index	Middle	Ring	Pinky	Current (mA)
s1	17.6	25.98	62.72	82.85	30
s2	32.95	43.46	48.87	35.11	23
s3	31.34	23.94	22.56	1.06	30
s6	22.62	67.43	26.54	5.36	17
s8	19.63	40.36	16.67	18.92	27
s9	20.82	53.92	57.73	38.60	19

Table 7.12. Subjects ROM (°) per finger during ICS with concentric electrodes in Z4.

Subject	Index	Middle	Ring	Pinky	Current (mA)
s1	14.09	14.55	38.70	21.55	30
s2	58.54	81.09	67.16	24.60	27
s3	13.62	15.63	14.11	1.43	30

Chapter 8. References

[1] V. L. Feigin *et al.*, “World Stroke Organization (WSO): Global Stroke Fact Sheet 2025,” *International Journal of Stroke*, p. 17474930241308142, Dec. 2024, doi: 10.1177/17474930241308142.

[2] DIPRECE, “Problema de salud AUGE N°37 Ataque Cerebrovascular Isquémico en personas de 15 años y más,” DIPRECE. Accessed: Aug. 31, 2024. [Online]. Available: https://diprece.minsal.cl/garantias-explicitas-en-salud-auge-o-ges/guias-de-practica-clinica/ataque-cerebrovascular-isquemico-en-personas-de-15-anos-y-mas/descripcion-y-epidemiologia-2/

[3] K. Cisek and J. D. Kelleher, “Current Topics in Technology-Enabled Stroke Rehabilitation and Reintegration: A Scoping Review and Content Analysis,” *IEEE Transactions on Neural Systems and Rehabilitation Engineering*, vol. 31, pp. 3341–3352, 2023, doi: 10.1109/TNSRE.2023.3304758.

[4] Y. Yang *et al.*, “Prediction Models for Post-Stroke Cognitive Impairment: A Systematic Review and Meta-Analysis,” *Public Health Nursing*, vol. n/a, no. n/a, doi: 10.1111/phn.13509.

[5] D. Dutta, S. Sen, S. Aruchamy, and S. Mandal, “Prevalence of post-stroke upper extremity paresis in developing countries and significance of m-Health for rehabilitation after stroke - A review,” *Smart Health*, vol. 23, p. 100264, Mar. 2022, doi: 10.1016/j.smhl.2022.100264.

[6] X. Li, Y. He, D. Wang, and M. J. Rezaei, “Stroke rehabilitation: from diagnosis to therapy,” *Front. Neurol.*, vol. 15, Aug. 2024, doi: 10.3389/fneur.2024.1402729.

[7] H. L. Choi *et al.*, “Increased Risk of Developing Depression in Disability after Stroke: A Korean Nationwide Study,” *International Journal of Environmental Research and Public Health*, vol. 20, no. 1, Art. no. 1, Jan. 2023, doi: 10.3390/ijerph20010842.

[8] J. E. Sanner Beauchamp *et al.*, “A Retrospective Study to Identify Novel Factors Associated with Post-stroke Anxiety,” *Journal of Stroke and Cerebrovascular Diseases*, vol. 29, no. 2, p. 104582, Feb. 2020, doi: 10.1016/j.jstrokecerebrovasdis.2019.104582.

[9] “What is Electrical Stimulation Treatment? – IFESS.” Accessed: Aug. 17, 2024. [Online]. Available: https://ifess.org/what-is-fes/

[10] M. Gandolla, L. Niero, F. Molteni, E. Guanziroli, N. S. Ward, and A. Pedrocchi, “Brain Plasticity Mechanisms Underlying Motor Control Reorganization: Pilot Longitudinal Study on Post-Stroke Subjects,” *Brain Sci*, vol. 11, no. 3, p. 329, Mar. 2021, doi: 10.3390/brainsci11030329.

[11] M. G. H. Kristensen, H. Busk, and T. Wienecke, “Neuromuscular Electrical Stimulation Improves Activities of Daily Living Post Stroke: A Systematic Review and Meta-analysis,” *Archives of Rehabilitation Research and Clinical Translation*, vol. 4, no. 1, p. 100167, Mar. 2022, doi: 10.1016/j.arrct.2021.100167.

[12] C. Marquez-Chin and M. R. Popovic, “Functional electrical stimulation therapy for restoration of motor function after spinal cord

injury and stroke: a review," *BioMed Eng OnLine*, vol. 19, no. 1, p. 34, Dec. 2020, doi: 10.1186/s12938-020-00773-4.

[13] A. S. P. Sousa *et al.*, "Usability of Functional Electrical Stimulation in Upper Limb Rehabilitation in Post-Stroke Patients: A Narrative Review," *Sensors*, vol. 22, no. 4, Art. no. 4, Jan. 2022, doi: 10.3390/s22041409.

[14] D. B. Popović, "Advances in functional electrical stimulation (FES)," *Journal of Electromyography and Kinesiology*, vol. 24, no. 6, pp. 795–802, Dec. 2014, doi: 10.1016/j.jelekin.2014.09.008.

[15] E. Losanno, M. Mender, C. Chestek, S. Shokur, and S. Micera, "Neurotechnologies to restore hand functions," *Nat Rev Bioeng*, vol. 1, no. 6, pp. 390–407, Jun. 2023, doi: 10.1038/s44222-023-00054-4.

[16] Axelgaard, "Axelgaard - Educational Resources." Accessed: Sep. 02, 2024. [Online]. Available: https://www.axelgaard.com/Education

[17] A. Gupta, N. Vardalakis, and F. B. Wagner, "Neuroprosthetics: from sensorimotor to cognitive disorders," *Commun Biol*, vol. 6, no. 1, pp. 1–17, Jan. 2023, doi: 10.1038/s42003-022-04390-w.

[18] A. R. Trent, P. Chopra, and A. Jain, "Peripheral Nerve Stimulator," in *StatPearls*, Treasure Island (FL): StatPearls Publishing, 2024. Accessed: Aug. 23, 2024. [Online]. Available: http://www.ncbi.nlm.nih.gov/books/NBK539703/

[19] H. Usman, Y. Zhou, B. Metcalfe, and D. Zhang, "A Functional Electrical Stimulation System of High-Density Electrodes With Auto-Calibration for Optimal Selectivity," *IEEE Sensors J.*, vol. 20, no. 15, pp. 8833–8843, Aug. 2020, doi: 10.1109/JSEN.2020.2983004.

[20] K. Bazaka and M. V. Jacob, “Implantable Devices: Issues and Challenges,” *Electronics*, vol. 2, no. 1, Art. no. 1, Mar. 2013, doi: 10.3390/electronics2010001.

[21] Y.-H. Joung, “Development of Implantable Medical Devices: From an Engineering Perspective,” *International Neurourology Journal*, vol. 17, no. 3, p. 98, Sep. 2013, doi: 10.5213/inj.2013.17.3.98.

[22] R. Velik, N. Malešević, L. Maneski, U. Hoffmann, and T. Keller, *INTFES: A Multi-pad Electrode System for Selective Transcutaneous Electrical Muscle Stimulation*. 2011.

[23] M. Kutlu, C. T. Freeman, E. Hallewell, A.-M. Hughes, and D. S. Laila, “Upper-limb stroke rehabilitation using electrode-array based functional electrical stimulation with sensing and control innovations,” *Medical Engineering & Physics*, vol. 38, no. 4, pp. 366–379, Apr. 2016, doi: 10.1016/j.medengphy.2016.01.004.

[24] N. M. Malešević *et al.*, “A multi-pad electrode based functional electrical stimulation system for restoration of grasp,” *Journal of NeuroEngineering and Rehabilitation*, vol. 9, no. 1, p. 66, Sep. 2012, doi: 10.1186/1743-0003-9-66.

[25] U. Hoffmann, M. Deinhofer, and T. Keller, “Automatic determination of parameters for multipad functional electrical stimulation: Application to hand opening and closing,” in *2012 Annual International Conference of the IEEE Engineering in Medicine and Biology Society*, Aug. 2012, pp. 1859–1863. doi: 10.1109/EMBC.2012.6346314.

[26] M. A. Garenfeld *et al.*, “A compact system for simultaneous stimulation and recording for closed-loop myoelectric control,” *Journal*

of NeuroEngineering and Rehabilitation, vol. 18, no. 1, p. 87, May 2021, doi: 10.1186/s12984-021-00877-5.

[27] S. Ferrante *et al.*, "A Personalized Multi-Channel FES Controller Based on Muscle Synergies to Support Gait Rehabilitation after Stroke," *Front. Neurosci.*, vol. 10, Sep. 2016, doi: 10.3389/fnins.2016.00425.

[28] J. S. Jara, S. Agger, and E. R. Hollis, "Functional Electrical Stimulation and the Modulation of the Axon Regeneration Program," *Front. Cell Dev. Biol.*, vol. 8, Aug. 2020, doi: 10.3389/fcell.2020.00736.

[29] Y. Hara, "Rehabilitation with Functional Electrical Stimulation in Stroke Patients," *Int J Phys Med Rehabil*, vol. 01, no. 06, 2013, doi: 10.4172/2329-9096.1000147.

[30] N. Nakanishi *et al.*, "Effect of Electrical Muscle Stimulation on Upper and Lower Limb Muscles in Critically Ill Patients: A Two-Center Randomized Controlled Trial," *Critical Care Medicine*, vol. 48, no. 11, p. e997, Nov. 2020, doi: 10.1097/CCM.0000000000004522.

[31] A. D. Koutsou, J. C. Moreno, A. J. del Ama, E. Rocon, and J. L. Pons, "Advances in selective activation of muscles for non-invasive motor neuroprostheses," *Journal of NeuroEngineering and Rehabilitation*, vol. 13, no. 1, p. 56, Jun. 2016, doi: 10.1186/s12984-016-0165-2.

[32] L. Popović-Maneski *et al.*, "Multi-Pad Electrode for Effective Grasping: Design," *IEEE Transactions on Neural Systems and Rehabilitation Engineering*, vol. 21, no. 4, pp. 648–654, Jul. 2013, doi: 10.1109/TNSRE.2013.2239662.

[33] L. Popović-Maneski, "Non-invasive Functional Electrical Stimulation in Rehabilitation Engineering," in *Advances in Biomedical and*

Veterinary Engineering, P. Bonačić Bartolin, R. Magjarević, M. Allen, and M. Sutcliffe, Eds., Cham: Springer Nature Switzerland, 2024, pp. 46–52. doi: 10.1007/978-3-031-42243-0_4.

[34] M. A. Trout, A. T. Harrison, M. R. Brinton, and J. A. George, "A portable, programmable, multichannel stimulator with high compliance voltage for noninvasive neural stimulation of motor and sensory nerves in humans," *Sci Rep*, vol. 13, no. 1, p. 3469, Mar. 2023, doi: 10.1038/s41598-023-30545-8.

[35] A. Martín-Odriozola *et al.*, "Analysis of the movements generated by a multi-field functional electrical stimulation device for upper extremity rehabilitation," *Artificial Organs*, vol. 46, no. 10, pp. 2027–2033, 2022, doi: 10.1111/aor.14346.

[36] M. G. Garcia-Garcia, L. I. Jovanovic, and M. R. Popovic, "Comparing preference related to comfort in torque-matched muscle contractions between two different types of functional electrical stimulation pulses in able-bodied participants," *The Journal of Spinal Cord Medicine*, vol. 44, no. sup1, pp. S215–S224, Sep. 2021, doi: 10.1080/10790268.2021.1970882.

[37] R. M. de Freitas, M. Capogrosso, T. Nomura, and M. Milosevic, "Preferential activation of proprioceptive and cutaneous sensory fibers compared to motor fibers during cervical transcutaneous spinal cord stimulation: a computational study," *J. Neural Eng.*, vol. 19, no. 3, p. 036012, May 2022, doi: 10.1088/1741-2552/ac6a7c.

[38] R. G. Braun and G. F. Wittenberg, "Motor Recovery: How Rehabilitation Techniques and Technologies Can Enhance Recovery and

Neuroplasticity," *Semin Neurol*, vol. 41, no. 02, pp. 167–176, Apr. 2021, doi: 10.1055/s-0041-1725138.

[39] N. Bryson *et al.*, "Enhanced selectivity of transcutaneous spinal cord stimulation by multielectrode configuration," *J. Neural Eng.*, vol. 20, no. 4, p. 046015, Jul. 2023, doi: 10.1088/1741-2552/ace552.

[40] A. Crema, N. Malesevic, I. Furfaro, F. Raschella, A. Pedrocchi, and S. Micera, "A Wearable Multi-Site System for NMES-Based Hand Function Restoration," *IEEE Trans. Neural Syst. Rehabil. Eng.*, vol. 26, no. 2, pp. 428–440, Feb. 2018, doi: 10.1109/TNSRE.2017.2703151.

[41] M. Krenn, U. S. Hofstoetter, S. M. Danner, K. Minassian, and W. Mayr, "Multi-Electrode Array for Transcutaneous Lumbar Posterior Root Stimulation," *Artificial Organs*, vol. 39, no. 10, pp. 834–840, Oct. 2015, doi: 10.1111/aor.12616.

[42] H. Shin and X. Hu, "Multichannel Nerve Stimulation for Diverse Activation of Finger Flexors," *IEEE Trans. Neural Syst. Rehabil. Eng.*, vol. 27, no. 12, pp. 2361–2368, Dec. 2019, doi: 10.1109/TNSRE.2019.2947785.

[43] S. C. O. Martins and S. S. Matuja, "Acute stroke care in low and middle-income countries," *Current Opinion in Neurology*, p. 10.1097/WCO.0000000000001332, Nov. 2024, doi: 10.1097/WCO.0000000000001332.

[44] C. Pantoja-Ruiz *et al.*, "Socioeconomic Status and Stroke: A Review of the Latest Evidence on Inequalities and Their Drivers," *Stroke*, vol. 0, no. 0, Dec. 2024, doi: 10.1161/STROKEAHA.124.049474.

[45] C. van Zyl, M. Badenhorst, S. Hanekom, and M. Heine, “Unravelling ‘low-resource settings’: a systematic scoping review with qualitative content analysis,” *BMJ Glob Health*, vol. 6, no. 6, Jun. 2021, doi: 10.1136/bmjgh-2021-005190.

[46] R. G. Barelli, V. F. Avelino, and M. C. F. Castro, “STIMGRASP: A Home-Based Functional Electrical Stimulator for Grasp Restoration in Daily Activities,” *Sensors*, vol. 23, no. 1, Art. no. 1, Jan. 2023, doi: 10.3390/s23010010.

[47] “MyndMove™ Therapy - MyndTec Inc.” Accessed: Oct. 11, 2024. [Online]. Available: https://myndtec.com/clinicians/myndmove-therapy/

[48] N. RaviChandran, M. Y. Teo, A. McDaid, and K. Aw, “Conformable Electrode Arrays for Wearable Neuroprostheses,” *Sensors*, vol. 23, no. 6, p. 2982, Mar. 2023, doi: 10.3390/s23062982.

[49] W. Besio, R. Aakula, K. Koka, and W. Dai, “Development of a Tri-polar Concentric Ring Electrode for Acquiring Accurate Laplacian Body Surface Potentials,” *Ann Biomed Eng*, vol. 34, no. 3, pp. 426–435, Mar. 2006, doi: 10.1007/s10439-005-9054-8.

[50] W. Besio and A. Prasad, “Analysis of Skin-Electrode Impedance Using Concentric Ring Electrode,” in *2006 International Conference of the IEEE Engineering in Medicine and Biology Society*, Aug. 2006, pp. 6414–6417. doi: 10.1109/IEMBS.2006.260048.

[51] A. Datta, M. Elwassif, F. Battaglia, and M. Bikson, “Transcranial current stimulation focality using disc and ring electrode configurations: FEM analysis,” *J. Neural Eng.*, vol. 5, no. 2, p. 163, Apr. 2008, doi: 10.1088/1741-2560/5/2/007.

[52] W. G. Besio, R. Hadidi, O. Makeyev, H. Luna-Munguía, and L. Rocha, "Electric fields in hippocampus due to transcranial focal electrical stimulation via concentric ring electrodes," in *2011 Annual International Conference of the IEEE Engineering in Medicine and Biology Society*, Aug. 2011, pp. 5488–5491. doi: 10.1109/IEMBS.2011.6091400.

[53] M. Bortoletto, C. Rodella, R. Salvador, P. C. Miranda, and C. Miniussi, "Reduced Current Spread by Concentric Electrodes in Transcranial Electrical Stimulation (tES)," *Brain Stimulation: Basic, Translational, and Clinical Research in Neuromodulation*, vol. 9, no. 4, pp. 525–528, Jul. 2016, doi: 10.1016/j.brs.2016.03.001.

[54] N. RaviChandran, M. Y. Teo, K. Aw, and A. McDaid, "Design of Transcutaneous Stimulation Electrodes for Wearable Neuroprostheses," *IEEE Trans. Neural Syst. Rehabil. Eng.*, vol. 28, no. 7, pp. 1651–1660, Jul. 2020, doi: 10.1109/TNSRE.2020.2994900.

[55] C. Keogh *et al.*, "Non-invasive phrenic nerve stimulation to avoid ventilator-induced diaphragm dysfunction in critical care," *Artificial Organs*, vol. 46, no. 10, pp. 1988–1997, Oct. 2022, doi: 10.1111/aor.14244.

[56] M. G. Cassar, C. Sebu, M. Pidcock, S. Chandak, and B. Andrews, "Optimal design of electrodes for functional electrical stimulation applications to single layer isotropic tissues," *COMPEL*, vol. 42, no. 3, pp. 695–707, May 2023, doi: 10.1108/COMPEL-08-2022-0293.

[57] H. Wu *et al.*, "Materials, Devices, and Systems of On-Skin Electrodes for Electrophysiological Monitoring and Human–Machine Interfaces,"

Advanced Science, vol. 8, no. 2, p. 2001938, Jan. 2021, doi: 10.1002/advs.202001938.

[58] L. Golestanirad, C. Pollo, and S. J. Graham, "Analysis of fractal electrodes for efficient neural stimulation," in *2013 35th Annual International Conference of the IEEE Engineering in Medicine and Biology Society (EMBC)*, Osaka: IEEE, Jul. 2013, pp. 791–794. doi: 10.1109/EMBC.2013.6609619.

[59] H. Gnanasambanthan, D. Ghosh, K. Hemavathy, A. Tyagi, S. Addy, and D. Maji, "Study of electrical conductivity, biocompatibility and degradation effect of copper electrodes with hydrogel coatings for use in flexible electronics," *Appl. Phys. A*, vol. 130, no. 5, p. 273, May 2024, doi: 10.1007/s00339-024-07444-4.

[60] S. Chamani, L. Mobasheri, Z. Rostami, I. Zare, A. Naghizadeh, and E. Mostafavi, "Heavy metals in contact dermatitis: A review," *J Trace Elem Med Biol*, vol. 79, p. 127240, Sep. 2023, doi: 10.1016/j.jtemb.2023.127240.

[61] P. D. Pigatto, S. M. Ferrucci, L. Brambilla, and G. Guzzi, "Alopecia Areata and Toxic Metals," *Skin Appendage Disord*, vol. 6, no. 3, pp. 177–179, 2020, doi: 10.1159/000507296.

[62] E. Skrzetuska, D. Michalak, and I. Krucińska, "Design and Analysis of Electrodes for Electrostimulation (TENS) Using the Technique of Film Printing and Embroidery in Textiles," *Sensors*, vol. 21, no. 14, p. 4789, Jul. 2021, doi: 10.3390/s21144789.

[63] K. Lim *et al.*, “Material and structural considerations for high-performance electrodes for wearable skin devices,” *Commun Mater*, vol. 5, no. 1, pp. 1–17, Apr. 2024, doi: 10.1038/s43246-024-00490-8.

[64] Q. Li *et al.*, “Review of Printed Electrodes for Flexible Devices,” *Front. Mater.*, vol. 5, p. 77, Jan. 2019, doi: 10.3389/fmats.2018.00077.

[65] B. Stephens-Fripp, V. Sencadas, R. Mutlu, and G. Alici, “Reusable Flexible Concentric Electrodes Coated With a Conductive Graphene Ink for Electrotactile Stimulation,” *Front. Bioeng. Biotechnol.*, vol. 6, p. 179, Dec. 2018, doi: 10.3389/fbioe.2018.00179.

[66] A. A. Chlaihawi, B. B. Narakathu, S. Emamian, B. J. Bazuin, and M. Z. Atashbar, “Development of printed and flexible dry ECG electrodes,” *Sensing and Bio-Sensing Research*, vol. 20, pp. 9–15, Sep. 2018, doi: 10.1016/j.sbsr.2018.05.001.

[67] E. Mirzakhalili, B. Barra, M. Capogrosso, and S. F. Lempka, “Biophysics of Temporal Interference Stimulation,” *Cell Systems*, vol. 11, no. 6, pp. 557-572.e5, Dec. 2020, doi: 10.1016/j.cels.2020.10.004.

[68] É. P. Rampazo and R. E. Liebano, “Analgesic Effects of Interferential Current Therapy: A Narrative Review,” *Medicina*, vol. 58, no. 1, Art. no. 1, Jan. 2022, doi: 10.3390/medicina58010141.

[69] G. C. Goats, “Interferential current therapy.,” *Br J Sports Med*, vol. 24, no. 2, pp. 87–92, Jun. 1990.

[70] K. Kozasa, R. Fujihara, H. Hirai, and H. I. Krebs, “Interferential Electrical Stimulation Applied to the Soleus Muscle in Humans: Preliminary Study on the Relationship Among Stimulation Parameters, Force Output, and Pain Sensation,” in *2018 7th IEEE International*

Conference on Biomedical Robotics and Biomechatronics (Biorob), Enschede: IEEE, Aug. 2018, pp. 1038–1043. doi: 10.1109/BIOROB.2018.8488076.

[71] S. Bounyong, S. Adachi, T. Yoshimoto, T. Ota, and J. Ozawa, "Controlling interfered area in interferential current stimulation by electrode-area patterning," in *2016 38th Annual International Conference of the IEEE Engineering in Medicine and Biology Society (EMBC)*, Aug. 2016, pp. 1721–1724. doi: 10.1109/EMBC.2016.7591048.

[72] X. Liu, S. Qi, L. Hou, Y. Liu, and X. Wang, "Noninvasive Deep Brain Stimulation via Temporal Interference Electric Fields Enhanced Motor Performance of Mice and Its Neuroplasticity Mechanisms," *Mol Neurobiol*, vol. 61, no. 6, pp. 3314–3329, Jun. 2024, doi: 10.1007/s12035-023-03721-0.

[73] M. Tugay and A. Kul, "Efficacy of Interferential Current Therapy in Patients Diagnosed with Subacromial Impingement Syndrome," *Eurasian J Med*, vol. 55, no. 3, pp. 192–198, Oct. 2023, doi: 10.5152/eurasianjmed.2023.22282.

[74] H.-L. Chen, F.-A. Yang, T.-H. Lee, T.-H. Liou, R. Escorpizo, and H.-C. Chen, "Effectiveness of interferential current therapy in patients with knee osteoarthritis: a systematic review and meta-analysis of randomized controlled trials," *Sci Rep*, vol. 12, no. 1, p. 9694, Jun. 2022, doi: 10.1038/s41598-022-13478-6.

[75] Z. Korkut, E. T. Demir, and S. T. Celenay, "Effects of interferential current stimulation in women with pelvic organ prolapse: a prospective

randomized sham-controlled study," *Int Urogynecol J*, vol. 34, no. 1, pp. 279–289, Jan. 2023, doi: 10.1007/s00192-022-05402-3.

[76] L. Jabban *et al.*, "The comfort of temporal interference stimulation on the forearm: computational and psychophysical evaluation," *J. Neural Eng.*, vol. 22, no. 2, p. 026044, Apr. 2025, doi: 10.1088/1741-2552/adc33b.

[77] M. Stefano, F. Cordella, A. Loppini, S. Filippi, and L. Zollo, "A Multiscale Approach to Axon and Nerve Stimulation Modeling: A Review," *IEEE Transactions on Neural Systems and Rehabilitation Engineering*, vol. 29, pp. 397–407, 2021, doi: 10.1109/TNSRE.2021.3054551.

[78] N. RaviChandran, J. Hope, K. Aw, and A. McDaid, "Modeling the excitation of nerve axons under transcutaneous stimulation," *Computers in Biology and Medicine*, vol. 165, p. 107463, Oct. 2023, doi: 10.1016/j.compbiomed.2023.107463.

[79] J. Gómez-Tames, J. González, and W. Yu, "Influence of Different Geometric Representations of the Volume Conductor on Nerve Activation during Electrical Stimulation," *Computational and Mathematical Methods in Medicine*, vol. 2014, pp. 1–10, 2014, doi: 10.1155/2014/489240.

[80] A. Kuhn, T. Keller, M. Lawrence, and M. Morari, "The Influence of Electrode Size on Selectivity and Comfort in Transcutaneous Electrical Stimulation of the Forearm," *IEEE Transactions on Neural Systems and Rehabilitation Engineering*, vol. 18, no. 3, pp. 255–262, Jun. 2010, doi: 10.1109/TNSRE.2009.2039807.

[81] R. Osorio L., S. M. Hall, F. Saavedra R., P. Aqueveque N., J. J. FitzGerald, and B. Andrews, “Finite Element Modelling for Biophysical Models of Nervous System Stimulation: Best Practices for Multiscale Adaptive Meshing,” *IEEE Transactions on Neural Systems and Rehabilitation Engineering*, vol. 33, pp. 298–309, 2025, doi: 10.1109/TNSRE.2024.3525343.

[82] A. Kuhn, T. Keller, M. Lawrence, and M. Morari, “A model for transcutaneous current stimulation: simulations and experiments,” *Med Biol Eng Comput*, vol. 47, no. 3, pp. 279–289, Mar. 2009, doi: 10.1007/s11517-008-0422-z.

[83] IT’IS Foundation, “Dielectric Properties.” [Online]. Available: https://itis.swiss

[84] 3D4Medical, “Complete Anatomy.” [Online]. Available: https://3d4medical.com/

[85] J. P. Dmochowski, A. Datta, M. Bikson, Y. Su, and L. C. Parra, “Optimized multi-electrode stimulation increases focality and intensity at target,” *J. Neural Eng.*, vol. 8, no. 4, p. 046011, Aug. 2011, doi: 10.1088/1741-2560/8/4/046011.

[86] F. Rattay, *Electrical Nerve Stimulation*. Vienna: Springer Vienna, 1990. doi: 10.1007/978-3-7091-3271-5.

[87] F. Rattay, “The basic mechanism for the electrical stimulation of the nervous system,” *Neuroscience*, vol. 89, no. 2, pp. 335–346, Mar. 1999, doi: 10.1016/S0306-4522(98)00330-3.

[88] C. C. McIntyre, A. G. Richardson, and W. M. Grill, “Modeling the Excitability of Mammalian Nerve Fibers: Influence of Afterpotentials on

the Recovery Cycle," *Journal of Neurophysiology*, vol. 87, no. 2, pp. 995–1006, Feb. 2002, doi: 10.1152/jn.00353.2001.

[89] S. Danner, C. Wenger, and F. Rattay, *Electrical stimulation of myelinated axons: An interactive tutorial supported by computer simulation*. 2011.

[90] Formlabs, "Flexible Resin for Ergonomic Features." [Online]. Available: https://formlabs-media.formlabs.com/datasheets/Flexible_Technical.pdf

[91] Creative Materials, "Electrically Conductive Medical Electrode Ink." [Online]. Available: https://server.creativematerials.com/datasheets/DS_117_23.pdf

[92] H. Lee, D. Kim, and Y.-L. Park, "Explainable Deep Learning Model for EMG-Based Finger Angle Estimation Using Attention," *IEEE Transactions on Neural Systems and Rehabilitation Engineering*, vol. 30, pp. 1877–1886, 2022, doi: 10.1109/TNSRE.2022.3188275.

[93] J. H. Challis, "Quaternions as a solution to determining the angular kinematics of human movement," *BMC Biomedical Engineering*, vol. 2, no. 1, p. 5, Mar. 2020, doi: 10.1186/s42490-020-00039-z.

[94] P. Shenoy, A. Gupta, and V. S.K.M., "Design and Validation of an IMU Based Full Hand Kinematic Measurement System," *IEEE Access*, vol. 10, pp. 93812–93830, 2022, doi: 10.1109/ACCESS.2022.3203186.

[95] F. V. Bennekom, "Visual Analog Survey Scale -- A Pain-ful Misnamed Scale," Great Brook Consulting. Accessed: Dec. 05, 2024. [Online]. Available: https://greatbrook.com/visual-analog-survey-scale/

[96] A. Tong, P. Perera, Z. Sarsenbayeva, A. McEwan, A. C. De Silva, and A. Withana, “Fully 3D-Printed Dry EEG Electrodes,” *Sensors*, vol. 23, no. 11, Art. no. 11, Jan. 2023, doi: 10.3390/s23115175.

[97] R. Dey *et al.*, “Graphene-based electrodes for ECG signal monitoring: Fabrication methodologies, challenges and future directions,” *Cogent Engineering*, vol. 10, no. 1, p. 2246750, Dec. 2023, doi: 10.1080/23311916.2023.2246750.

[98] H. Yuk *et al.*, “3D printing of conducting polymers,” *Nat Commun*, vol. 11, no. 1, p. 1604, Mar. 2020, doi: 10.1038/s41467-020-15316-7.

[99] J. Baier, S. Selkmann, and B. Bender, “Simulation of FES on the forearm with muscle-specific activation resolution,” *Front. Bioeng. Biotechnol.*, vol. 12, Jun. 2024, doi: 10.3389/fbioe.2024.1384617.